Applications of x-ray computed tomography polymer gel dosimetry

by

Evan David Maynard
B.Sc., University of Victoria, 2010
M.Sc., University of Victoria, 2014

A Dissertation Submitted in Partial Fulfillment of the
Requirements for the Degree of

DOCTOR OF PHILOSOPHY

in the Department of Physics and Astronomy

Applications of x-ray computed tomography polymer gel dosimetry

by

Evan David Maynard
B.Sc., University of Victoria, 2010
M.Sc., University of Victoria, 2014

Supervisory Committee

Dr. Andrew Jirasek, Co-Supervisor
(Department of Physics and Astronomy)

Dr. Michelle Hilts, Co-Supervisor
(Department of Physics and Astronomy)

Dr. Derek Wells, Departmental Member
(Department of Physics and Astronomy)

Dr. Jody Klymak, Outside Member
(School of Earth and Ocean Sciences)

Supervisory Committee

Dr. Andrew Jirasek, Co-Supervisor
(Department of Physics and Astronomy)

Dr. Michelle Hilts, Co-Supervisor
(Department of Physics and Astronomy)

Dr. Derek Wells, Departmental Member
(Department of Physics and Astronomy)

Dr. Jody Klymak, Outside Member
(School of Earth and Ocean Sciences)

ABSTRACT

Radiation therapy, one of the most common forms of cancer treatment, is continually evolving with the introduction of new technology, more complex treatments and more advanced radiation dose calculations. To ensure the effectiveness and safety of modern radiation therapy, dose measurement tools must improve to accommodate these advances. X-ray computed tomography (CT) polymer gel dosimetry is a unique type of dosimeter that has many advantages and the potential to address some of the challenges in the verification of dose delivery and calculation in radiation therapy. This dissertation investigates the advancement of an x-ray CT polymer gel dosimetry system for use in clinical applications and in particular for deformable dose verification.

The first part of this work consists of a reproducibility study of an established x-ray CT polymer gel dosimetry system in an effort to determine the accuracy and precision of dose measurements made with this system and the feasibility of interbatch and generic calibration. Gel measurements were found to have excellent agreement

with Monte Carlo dose calculation when using a generic calibration curve. The excellent dosimetric and spatial accuracy established in this study suggest that this dosimetry system is ideally suited for the measurement of high-dose fractionation treatments such as stereotactic radiosurgery (SRS) or stereotactic body radiation therapy (SBRT). The second stage was the development and characterization of the first deformable x-ray CT polymer gel dosimetry system. This study established the setup reproducibility, deformation characteristics and dose response of the new deformable system. The dose response was found to be similar to that of the non-deformable system with similar dosimetric and spatial accuracy when compared to Monte Carlo dose calculation. The system was also found to have sub-millimetre setup reproducibility and the deformable dosimeter was found to reproducibly deform and relax for external compression of up to 30 mm and over 100 consecutive compressions. This work established several important characteristics of the new deformable dosimetry system and it shows excellent potential for use in the evaluation of deformable dose accumulation algorithms.

The final component of this dissertation was the use of the newly developed deformable dosimetry system in the evaluation of a novel deformable dose accumulation algorithm, defDOSXYZ. Gel measurements and defDOSXYZ showed excellent agreement in the case of a static control case and this set a benchmark for deformable dose measurements. Measurements of deformed dose by the gel dosimeter showed significant disagreement with dose deformed by defDOSXYZ and the dosimetric differences were well outside the uncertainties established in the first two studies of this dissertation. The results from this study provided some insight into potential avenues of improvement for both the deformable dose calculation and deformable dose measurements. These results were also the first example of deforming dose measured by an x-ray CT read out gel dosimetry system.

Overall, the results in this dissertation represent a significant advancement in x-ray CT polymer gel dosimetry and establish its suitability for several clinical applications.

Contents

List of Tables

List of Figures

List of Abbreviations

ART Adaptive Radiation Therapy

BIS N,N-methylenebisacrylamide

CT Computed Tomography

DIR Deformable Image Registration

DNA Deoxyribonucleic Acid

DTA Distance-To-Agreement

EPID Electronic Portal Imaging Device

HU Hounsfield Unit

IMRT Intensity Modulated Radiation Therapy

IGRT Image Guided Radiation Therapy

MRI Magnetic Resonance Imaging

MOSFET Metal Oxide Silicon Field Transistor

MU Monitor Unit

MLC Multi-leaf Collimator

NMR Nuclear Magnetic Resonance

NIPAM N-isopropylacrylamide

OSLD Optically Stimulated Luminescent Detector

PAG Polyacrylamide Gel

PGD Polymer Gel Dosimetry

RAR Remnant Artifact Removal

QA Quality Assurance

SBRT Stereotactic Body Radiation Therapy

SRS Stereotactic Radiosurgery

THPC Tetrakis (Hydroxylmethyl) Phosphonium Chloride

TLD Thermoluminescent Detector

TPS Treatment Planning System

VIMC Vancouver Island Monte Carlo

VMAT Volumetric Modulated Arc Therapy

ACKNOWLEDGEMENTS

First and foremost I would like to thank my supervisors Dr. Andrew Jirasek and Dr. Michelle Hilts for their guidance and support throughout the entierty of this project. This work would not have been possible without their incredible dedication and commitment. I would also like to thank Dr. Emily Heath for her collaboration on this project, her contribuions and insight was invaluable and she offered a significant amount of her time and knowledge to help make this work happen.

Working at the Vancouver Island Centre has been an fantastic experience and I need to thank the team of medical physiscts who always have their doors open and are always willing to help lost and confused grad students. I also need to thank Stephen Gray for all his help in the construction of various phantoms and devices, and for always keeping me on my toes and I could not have made it through my time in this program without the support of all my fellow medical physics graduate students, past and present.

Finally I would like to thank my parents for their support and encouragement throughout my entire academic career and my wife Loreena for tolerating, and loving, a grumpy Ph.D. student trying to finish a seemingly endless dissertation.

Chapter 1

Introduction

Cancer diagnosis and treatment is one of the most significant challenges of the Canadian healthcare system. Nearly half of all Canadians are expected to develop cancer at some point in their lifetime with one in four Canadians expected to die of the disease [2]. In 2017 there were an estimated 206,200 newly diagnosed cases of cancer in Canada and over 80,000 deaths, making it the number one cause of premature death [2]. This amounts to roughly 550 new diagnosed cancer cases and 200 deaths a day across the country, and with an aging population the rate of incidence of cancer diagnosis in Canada is expected to grow for the foreseeable future. Cancer is, however, often treatable with 60% of diagnosed cancer patients in Canada living at least 5 years beyond their date of initial diagnosis. Improvements in cancer prevention and treatment have led to decreasing age-standardized mortality rates in Canada for the past 30 years. Although much of this decrease can be attributed to cancer prevention and early detection efforts, improvement of treatments, including radiation therapy, have also had a significant impact [2]. Additionally, improvement of cancer treatment is not just about decreasing overall mortality, as treatment can not only lead to an increase in life expectancy but also to an improvement in quality of life for cancer patients.

Radiation therapy, one of the most common forms of cancer treatment, has made significant advances in recent years with new technology allowing for novel radiation delivery techniques. With the increasing complexity of treatments and radiation dose calculations it is imperative that dose measurement tools advance as well to accommodate the changing radiation therapy environment and ensure the safety and accuracy of radiation delivery. Polymer gel dosimetry (PGD) is a unique type of radiation measurement that has the potential to address a number of current challenges in the

verification of radiation delivery. Polymer gels use radiosensitive chemicals to measure the amount of radiation dose absorbed within the dosimeter. With the chemicals distributed evenly throughout the dosimeter the entire gel acts as the dose measurement tool, and therefore has the ability to measure dose distributions in three dimensions. Three dimensional (3D) dosimeters have advantages over more traditional one dimensional and two dimensional dosimeters, and 3D dosimeters are becoming increasingly important in more advanced radiation delivery techniques. The goal of this work is to advance an x-ray computed tomography (CT) polymer gel dosimetry system and establish clinical applications of this system.

1.1 Radiation Therapy

Radiation therapy along with surgery and chemotherapy, is one of the three main techniques for treating cancer. Chemotherapy can preferentially kill cells with characteristics that are generally associated with cancer, such as high proliferation, but often does significant damage to the rest of the patient. Surgery is the most common method of treatment and involves physically removing cancer cells; solid tumours are often targeted and the gross tumour volume is removed. Radiation kills cells in a non-discriminatory manner and cancer cells need to be targeted by localizing high radiation doses specifically to disease sites. The goal of radiation therapy is then to deliver a prescribed radiation dose to a defined treatment volume while sparing the surrounding healthy tissue as much as possible so negative side-effects from healthy tissue toxicities may be avoided. Radiation therapy can be used alone or in conjunction with chemotherapy and/or surgery and approximately half of all cancer patients are expected to receive radiation therapy over the course of their treatment [3].

1.1.1 Ionizing Radiation and Interactions with Matter

In a typical radiation therapy treatment, a beam of x-ray photons or electrons are delivered to a patient with primary photon or electron energies in the MeV range. In this energy range photons interact with matter through three main processes: photoelectric effect, Compton scattering and pair production. At the lower end of photon energies (<26 keV in water) the photoelectric effect is the dominant interaction in which a bound electron is ejected from the atom when a photon is absorbed [4]. The electron is ejected with a kinetic energy equal to the energy of the incoming

photon minus the energy required to remove the electron from its bound state. The probability of this interaction is approximately proportional to $\frac{Z^n}{E^3}$, where Z is the effective atomic number of the interaction medium, E is the energy of the incident photon and n is a number that varies between 3 and 5 [5]. This energy dependence leads to the photoelectric effect becoming insignificant at higher incident photon energies (>150 keV) and in the energy range most typical of radiation therapy (150 kev - 24 MeV), Compton scattering is the dominant interaction [4]. In a Compton scattering interaction an outer atomic shell electron is ejected and the photon is deflected with only a portion of its energy transferred to the ejected electron. The probability of a Compton scattering interaction is approximately proportional to $\frac{1}{E}$, so like the photoelectric effect it becomes less important as energy increases but unlike the photoelectric effect it is largely independent of the atomic number of the interaction medium. The final major interaction relevant in radiation therapy energy ranges is pair production, where the incident photon interacts at the nucleus and is absorbed in the production of an electron-positron pair. Given the rest mass of both an electron and positron is 511 keV the incident photon must have an energy of at least 1.022 MeV for pair production to occur and any energy in excess of this from the incident photon is imparted as kinetic energy split between the positron and electron.

Once the primary photons have interacted and transferred their energy to secondary electrons, the ejected electrons generated in these interactions will then travel through the matter and deposit energy along their track. A cascading effect occurs as ejected electrons interact with molecules creating more ionized molecules and more ejected electrons; other interactions will cause electrons to lose their energy through excitations or bremsstrahlung. Bremsstrahlung occurs when high speed electrons are slowed by Coulomb interaction with the nuclei of atoms and as the electrons are slowed they convert some fraction of their energy to one or more photons [5]. Energy is considered to be absorbed by the material when it is deposited by secondary electrons within the material, but not all energy transferred from the primary photons is absorbed and some escapes via scattered photons and bremsstrahlung radiation. The energy that is absorbed within the medium is described by a quantity called absorbed dose, which is defined as the amount of energy deposited in a given mass and has units of gray (Gy), equal to one joule per kilogram (J/kg).

Ionized molecules are highly reactive and in human cells can lead to significant damage though the breaking of chemical bounds. The energy is deposited randomly within human tissue but most of this does little permanent damage as most cellular

components have many copies and undergo quick replication and replacement. One critical component to cell survival, DNA, has only two copies within a cell and undergoes relatively infrequent turnover. Radiation induced DNA damage, specifically DNA double-strand breaks which are often unrepairable, is then what leads to cell death and tumor eradication in radiation therapy. The amount of absorbed dose delivered to human tissue can be related to the fraction of cells that will be killed through DNA damage and therefore the probability that any tumor cells will survive. For example, 1 Gy of absorbed dose will cause approximately 20-40 double-strand DNA breaks and will kill roughly 30% of cells in a typical human cell line [6]. To predict the biological effect radiation therapy will have, it is important to know what doses of radiation are delivered to tissues within the body. Treatments are planned with the goal of finding a balance between delivering enough dose to control the tumour growth and sparing enough of the surrounding normal tissue to avoid unacceptable side effects caused by normal tissue damage. For this reason, advancements in radiation therapy have focused on delivery techniques which limit dose delivered to normal tissue and allow for more precise radiation delivery to tumour volumes.

1.1.2 Modern Radiation Therapy Delivery

Modern radiation therapy consists of two main types of treatments: external beam radiation therapy and brachytherapy. Brachytherapy literally translates to "short-" therapy, as permenant or transient radiation sources are directly inserted into a patient to deliver radiation over as short a distance as possible. This work is concerned solely with mesurements of external beam radiation therapy which the remainder of this chapter will focus on. In the earliest days of external beam radiation therapy, high energy photon beams were achieved by use of cobalt-60 in a treatment machine known as a cobalt therapy unit. The decay of cobalt-60 produces photons with energy of 1.17 MeV and 1.33 MeV creating a photon beam with an average energy of 1.25 MeV [4]. In cobalt therapy, the amount of dose delivered was controlled by the length of treatment, the distance from the cobalt source to the patient and the collimation of the beam. Modern radiation therapy treatments are delivered by a specialized piece of equipment known as a medical linear accelerator which can produce a range of beam energies and also gives more control over the rate at which dose is delivered. Figure 1.1 shows an image of a linear accelerator and a simple diagram of the major components within the accelerator treatment head when delivering photon therapy.

When delivering a photon beam, electrons are produced via thermonic emission and accelerated by radio frequency pulses in a wave guide to generate a mono-energetic beam of electrons. The electrons are directed towards a tungsten target, which induces bremsstrahlung interactions within the target and creates a beam with a spectrum of photon energies. The maximum energy of the photon beam is the same as the energy of the electrons that hit the target and the photon beam is then designated by the voltage required to accelerate the electrons to the energy that produced the beam. The beam is then shaped by the various filters and collimators within the treatment head before reaching the delivery target. The entire treatment head sits on a gantry which allows the x-ray source to rotate about the patient and deliver radiation from any angle in the plane of rotation. The gantry rotates around a single point, called the isocentre, which is typically located 100 cm from the x-ray source. The fluence delivered by the linear accelerator is measured by the monitor ion chamber, and can be described by a unit known as the monitor unit (MU). The MU of a linear accelerator is often calibrated for a photon beam so that 1 MU is equal to 1 cGy at isocentre and at the depth of maximum dose in water for a 10×10 cm^2 field. The fluence rate, or machine dose rate, of radiation delivery is measured in units of MU per minute.

Modern radiation therapy often relies on highly modulated beams to deliver dose to the patient. The fixed primary collimator reduces the size of the beam prior to filtering and the two secondary collimators, known as the X and Y jaws and seen in figure 1.2a, allow for adjustable rectangular field shaping in two dimensions. Tertiary collimation of the radiation beam is done by the multi-leaf collimator (MLC), which sits within the linear accelerator head and is made up of high density leaves which allow for sub-millimetre dynamic shaping of the radiation beam. A typical MLC on a Varian TrueBeam (Varian Medical Systems, Palo Alto, CA, USA) linear accelerator can been seen in figure 1.2b and has either 40 or 60 pairs of leaves with the 20 outer pairs projecting a 10 mm width at isocentre and the 40 inner pairs projecting a 5 mm width at isocentre. The MLC is the basis of modern conformal radiation therapy techniques [7]. In 3D conformal radiation therapy (3DCRT) radiation beams are delivered from multiple angles with the MLC used to shape the beam to conform to the shape of the tumour that is being treated. By delivering radiation from different angles and shielding surrounding tissues from radiation using the MLC, a conformal 3D dose can be delivered to the tumour and normal tissues are significantly spared from dose. Intensity modulated radiation therapy (IMRT) is similar to 3DCRT in that several beams at different static gantry angles are delivered to the patient, how-

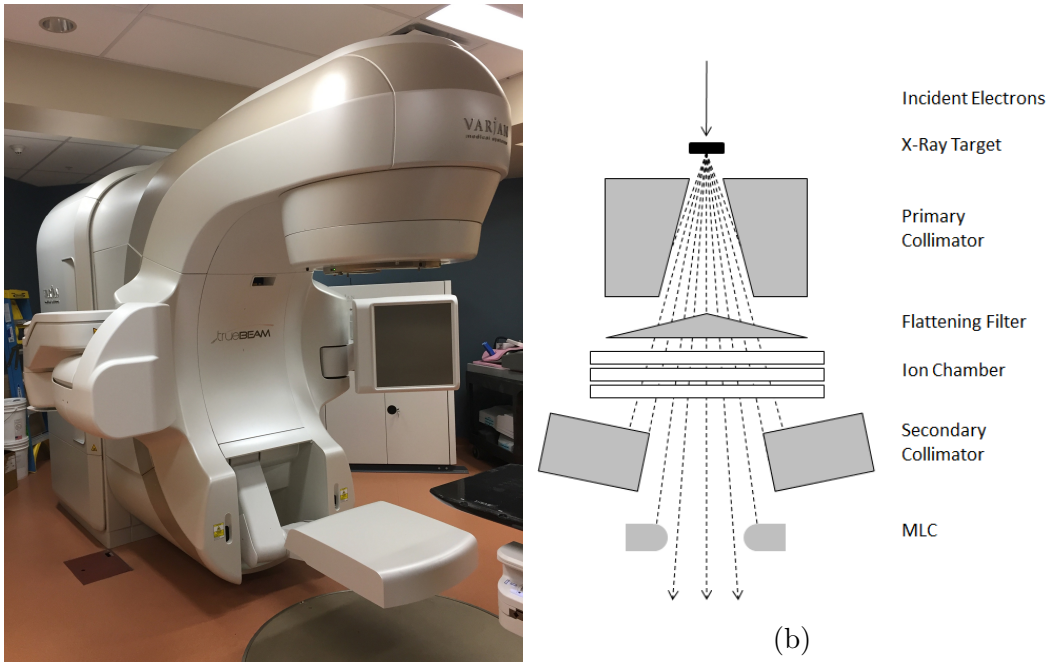

(a) (b)

Figure 1.1: (a) Image of a medical linear accelerator at the Vancouver Island Centre used in radiation therapy and (b) a schematic of the major components within the linear accelerator treatment head.

ever in IMRT the beams are dynamically modulated by the MLC during delivery. This dynamic modulation of the beam intensity makes it possible to shield normal tissue more effectively, particularly in cases where the target of high doses are near or overlapping with critical normal tissues, such as the bowel in prostate treatment. Inverse-planning and treatment plan optimization also play an important role in delivering dose in such a precise manner and will be discussed in the following section. The precise nature of the MLC collimation in IMRT allows for dose escalation to the tumour and these highly modulated treatment beams have been shown to improve patient outcomes and decrease normal tissue complications, making IMRT the standard radiation therapy treatment for many disease sites [8]. Volumetric modulated arc therapy (VMAT) is a natural extension of the IMRT treatment technique that delivers dose in a continuous 360° arc around the patient instead of in static beams [9]. In a VMAT treatment the MLC is continuously modulating the beam intensity, the gantry is continuously rotating around the patient at varying speed and the dose rate is dynamically modulated. The continuous delivery of radiation in VMAT treatments provides a decrease in overall treatment time and therefore improved patient comfort and a decrease in the chance of significant patient motion during delivery. VMAT deliveries also result in a lower overall "beam-on" time during treatment (in other words a lower number of overall MU delivered) which could potentially reduce the chance of a patient developing secondary malignancies [10–13].

Another advancing area of radiation therapy is the concept of ablative delivery techniques such as stereotactic radiosurgery (SRS) and stereotactic body radiation therapy (SBRT). In these treatment techniques, rather than delivering the prescribed dose in a large number of smaller fractions (typically 2 Gy per fraction over 20-30 fractions), patients are treated in a small number of fractions with a much higher dose per fraction (6-30 Gy per fraction over 1-5 fractions) [14, 15]. The idea is that with less time for tumour cells to repair and repopulate, delivering high doses over a relatively short treatment time will result in a more potent biological effect. The dose escalation used in these treatments can increase the risk of normal tissue damage and therefore the delivery of dose and selection of patients must be done carefully. Typically, SBRT and SRS treatments are used on smaller (<5 cm in diameter) tumours that are well-defined and have a smaller margin surrounding the tumour. These treatments often use a MLC with narrower leaves to provide more precise shaping of the radiation beam. To ensure dose delivery that is as accurate as possible patient positioning is maintained through specialized patient immobilization techniques, image guidance,

(a) (b)

Figure 1.2: Images of the treatment head with (a) the MLC leaves retracted and the X and Y secondary collimators visible and (b) the MLC extended and forming an aperture typically seen in advanced radiation therapy.

and the management of patient respiratory motion [15].

1.1.3 Treatment Planning and Dose Calculation

In complex radiation therapy deliveries there are many factors that can affect the way dose is deposited within a patient and the combination of all these factors determine the overall dose distribution. In a treatment as complex as VMAT one must consider the beam energy, dose rate, gantry position, gantry speed and position of each MLC leaf to determine the state of the radiation beam at each point within the treatment. To then determine how dose will be deposited in a patient, the beam delivered by the linear accelerator at each point of the treatment must be simulated as it passes through the patient anatomy. Given the complexity of this task it is not trivial to find the optimal delivery plan for each patient, and to achieve this goal a process known as inverse-planning is used. Inverse-planning works backwards from a list of weighted dose constraints and a treatment planning system (TPS) optimizes the relevant variables (leaf positions, gantry position, dose rate, etc.) to determine a delivery plan to best meet these constraints [7]. In general, the dose constraints consist of doses prescribed by radiation oncologists to kill the tumour cells and dose limits for surrounding normal tissues so that normal tissue toxicities are minimized. Although the TPS may not be able to meet all the constraints it is given due to physical limitations of the patient anatomy or linear accelerator, it will attempt to meet them as best as possible [7]. Once the plan of delivery has been optimized a dose calculation algorithm within the TPS calculates the dose distribution using the density of tissues from CT images of the patient, a characterization of the radiation beam specific to the linear accelerator that will be used for treatment, and modelling of the various collimators. In order to maintain a feasible calculation time, rather than calculating each particle of the radiation beam and its individual interactions, the TPS dose calculation splits the primary beam into smaller beamlets and models how these beamlets will deposit dose based on the patient's CT data, physical parameters, and measured beam data.

1.1.4 Quality Assurance

Given the complexities of treatment planning, dose calculation and dose delivery there are several potential sources of error between what is actually delivered by the linear accelerator and what is calculated in the TPS. These include physical discrepancies

of the accelerator itself such as errors in the gantry or MLC position and speed or dose rate errors [16]. Dosimetric calculation factors used in the TPS are also a source of potential error, these include the modelling of the MLC leaf ends and edges, calculation of transmission of radiation through the leaves, calculation of scattered dose and modelling of the radiation source [16]. There can also be errors within the treatment plan created during the transfer of data from the TPS to the linear accelerator due to the corruption of data. Though many of these errors may seem subtle, given the tight margins and high dose gradients present in modern radiation therapy deliveries they can potentially have significant impacts on the overall dose distribution. To ensure these types of errors are minimized, periodic quality assurance (QA) tests are performed on linear accelerators, CT scanners and the TPS. For many of these tests the process starts with the commisioning of equipment and software with QA ensuring consistency over time. These QA tests can involve measurements using dosimeters and imaging devices that have set tolerances indicating when action is required to address an issue [17]. Along with the individual QA of equipment and software used in the radiation therapy treatment chain, induvidual patient plans also undergo QA tests. To ensure the accuracy of the TPS dose calculation every treatment plan undergoes a secondary dose calculation check and some treatment plans undergo patient specific pretreatment verification which is a comprehensive verification of an individual's plan prior to treatment [18]. Pretreatment verification is often used for newer treatment techniques before there is an extended history of reliable dose calculation and delivery and in cases of high dose fractionation and small margins like SRS or SBRT. It aims to test all the accelerator and TPS factors as well as unexpected errors that could occur throughout the entire chain from planning to delivery; it is designed to be a final check that the planned and approved optimal treatment matches what is delivered. This type of measurement will often involve delivering a single fraction of the plan to one or more dosimeters that may or may not be embedded in a phantom. The dose measured by the dosimeter is compared to what the TPS predicts and if it falls within an acceptable tolerance the plan can then be safely delivered to the patient.

1.1.5 Patient Motion in Radiation Therapy

Another major source of uncertainty in the delivery and planning of radiation dose is patient motion. There can be intra-fraction motion, motion that occurs during

the delivery of each fraction such as organ motion due to patient breathing or shifts and rotations of the patient on the treatment couch. There can also be inter-fraction motion, motion that occurs in between the delivery of fractions that can be caused by day-to-day differences in patient setup on the couch and internal anatomy changes due to weight loss or related to the state of the digestive system [19]. Inter-fraction motion caused by human error during patient setup has the potential to be missed by regular machine QA, and limiting these types of errors must be considered when implementing radiation therapy. Patient motion can also occur during simulation stage of treatment, with orgrans or tumours moving while acquiring planning CT images. Ultimately these changes to the patient position or anatomy can lead to a difference in the position and state of the tumor and surrounding normal tissues compared to what was used to plan the radiation delivery. These differences could then potentially lead to underdosing of portions of the tumour or overdosing of normal tissue. Ideally, any motion would be accounted for in a safety margin surrounding the tumour that is applied during the planning process, however in the case of unexpected motion, exceptional changes to the anatomy, or overlapping anatomical structures this may not always be the case. Many steps are taken during treatment to minimize patient motion, including increasingly precise patient positioning devices to limit day-to-day changes in patient setup, immobilization devices to restrict patient movement on the treatment couch and many forms of image guidance during and prior to treatment. Image guided radiation therapy (IGRT) involves the use of medical imaging devices, attached to the linear accelerator or installed in the treatment room, to aid in the accurate delivery of radiation therapy. IGRT can consist of 2D x-ray images [20], cone beam CT [21] or MR images [22] used to position the patient as close as possible to the planning setup prior to treatment. Real time images and tracking can also be used to monitor intra-fraction patient motion and can even be used to gate the treatment based on breathing motion, only delivering radiation when the patient is in certain phases of the breathing cycle [23]. In high dose treatments such as SRS and SBRT more extensive patient immobilization and IGRT techniques are used because of the high doses, high dose gradients and small error margins associated with these treatments [15].

In many cases intra- and inter-fraction patient motion is not limited to simple shifts and rotations as internal changes can occur causing anatomical structures to not only move, but also deform. With improvements in on-board imaging equipment and the advent of 4D imaging techniques, adaptive radiation therapy (ART) is emerging as

a solution to internal patient deformations. ART is the reoptimization or replanning of a treatment when the original planned images no longer match the current patient anatomy [24]. In its simplest form ART is done off-line, in between fractions but with advancements in computing and dose calculation efficiency the potential for online, real-time ART exists [25, 26]. In order to evaluate the doses in ART that are delivered and planned on different anatomical states, either due to intra-fraction motion or over several different fractions, it is necessary to adapt or deform calculated dose across multiple sets of patient images to a single reference image. To do this dose deformation, a deformable image registration (DIR) algorithm is used to determine how each image set deforms to the reference image set. To date a number of different DIR algorithms and dose warping methods have been developed [27–30]. This type of deformable dose calculation, however, is difficult to validate and the use of a fully 3D, deformable dosimeter for this validation would be ideal.

1.2 Radiation Dosimetry

As radiation therapy has advanced, tumours that had previously been untreatable using radiation can now be treated [31, 32]. The ability to deliver more conformal dose has led to higher doses delivered to smaller volumes with smaller margins surrounding the treatment area, and treatments can now be delivered closer to critical structures within the body. These advances have led to improved outcomes for patients [31–33] and played a critical role in the advancement of cancer treatment but have also led to radiation treatments that are more complex, both in delivery and calculation. With more complex treatments and smaller margins for error, the need for advancements in radiation dosimetry is equally important to ensure that the dose indented to be delivered is the dose that is actually delivered.

Radiation dosimetry is the measurement of absorbed dose delivered by ionizing radiation. As mentioned in section 1.1.4, safe and accurate delivery of radiation therapy treatments relies on verification of these treatments through radiation dosimetry. Traditionally this has been, and still is, performed using one dimensional (1D) dosimeters, such as silicon diodes or ion chambers and two dimensional (2D) dosimeters, such as radiosensitive film and electronic portal imaging devices (EPID). Individual point dosimeters can also be combined to form 2D or 3D arrays of point measurements and more recently true 3D dosimeters have started to have an impact in the clinical setting in the evaluation of complex radiation therapy treatments [34, 35]. This section

will give a brief overview of radiation dosimeters that are currently used in the clinic and their various roles.

1.2.1 Current Dosimetry Tools

Point Dosimeters

Point dosimeters measure radiation in a single point and can be moved to acquire multiple measurements in a line to measure dose in 1D. There are several point dosimeters currently used in the cancer clinic including ionization chambers, thermoluminescent and optically stimulated luminescent detectors (OSLDs and TLDs), and solid-state detectors. Ionization chambers (or ion chambers) are essentially air filled cavities with a polarizing voltage to collect ion pairs produced in air by ionizing radiation. An example of a clinically used ion chamber can be seen in figure 1.3. The amount of charge collected is proportional to the dose delivered to the chamber and by applying corrections for temperature, pressure, and photon energy, one can determine the dose that would have been delivered to water at the position of the chamber. Ionization chamber are one of the most precise dose measuring devices and are considered the 'gold-standard' for point dose measurements. For this reason, ion chambers are often used in the QA and commissioning of linear accelerators when precise measurements of the dosimetric output are necessary [36]. Ionization chambers however have relatively large cavities, (they generally range from 2 to 6 mm in diameter) [37] and therefore even when used in an array have low spatial resolution and are susceptible to volume averaging artifacts in regions of high dose gradients.

Figure 1.3: A PTW (PTW, Freiburg, Germany) Farmer type ionization chamber.

A TLD is a detector made of a crystalline material, typically LiF or CaF_2, and when exposed to ionizing radiation electrons can be excited to long-lived energy levels or 'traps' of the material [38]. When heated the electrons are released from these traps and produce visible light as the electrons return to a lower energy state and measurement of this visible light output can be related to the dose absorbed by

the TLD. OSLDs are similar detectors, but rather than using thermal energy to release trapped electrons, visible light is used [39]. TLDs and OSLDs are typically used for personal radiation protection measurements, in-vivo surface dosimetry and comparison of inter-institute radiation deliveries.

Other solid state detectors used for point measurements include silicon diodes, metal oxide silicon field transistors (MOSFET) and diamond detectors. These types of detectors are semiconductors and when exposed to ionizing radiation a charge is created in the material. The charge can be collected from the active detector region of the semiconductor through the diffusion of ionized electrons-hole pairs to opposite sides of the semiconductor junction creating a current that is proportional to number of ion pairs produced. Solid state detectors have the advantage of higher sensitivity compared to ionization chambers and can therefore be made to have a smaller active region making them more suited for measurements in small fields or other applications where high spatial resolution is needed [5]. Solid state detectors, however, often require a significant number of correction factors to account for effects such as temperature dependence, dose rate dependence, field size dependence and detector orientation [40–43].

2D Dosimeters and Detector Arrays

There are several 2D dosimeters that are used clinically and these provide a more extensive picture of the deposition of dose than 1D measurements. Radiochromic film has commonly been used in the clinic for both linear accelerator QA and in some cases, pretreatment verification. Radiochromic film undergoes a solid state polymerization reaction leading to a change in colour and optical density of the film when exposed to ionizing radiation; an example of this can be seen in figure 1.4. Film measurements offer excellent spatial resolution in two dimensions, are near tissue equivalent and can be easily embedded within a larger phantom for measurement purposes, but film measurements require an extensive dose response calibration to convert optical density measurements to dose and the read out method can be somewhat laborious and time consuming [44]. Film is often used for mechanical checks where spatial accuracy is important such as in the measurement of couch, gantry and collimator rotation walkout. In complex radiation therapy such as IMRT or VMAT, film measurements are often limted to measuring each beam angle individually or collapsing all MLC motion to one beam delivery angle for the purpose of delivery verification [40]. Al-

though it is possible to embed radiographic film within a phantom to validate these deliveries from multiple beam angles with one film measurement, this can induce some uncertainty due the direction dependent response of film dosimeters.

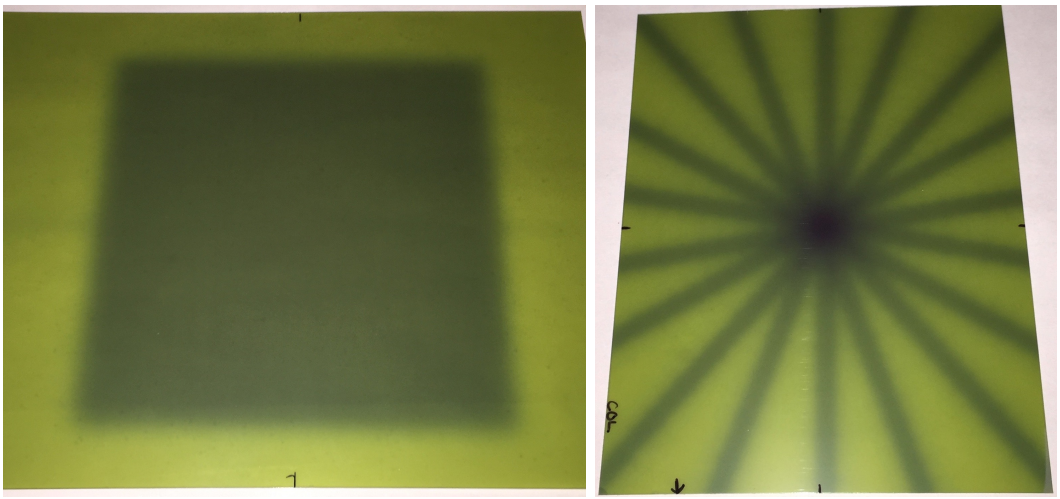

(a) (b)

Figure 1.4: Images of radiochromic film after being exposed to ionizing radiation delivered by a linear accelerator with (a) an open field delivery and (b) a star shot pattern that was used to measure collimator rotation walkout.

A more convenient 2D dose measurement device is the EPID, which is a flat panel detector that primarily functions to image and verify patient positioning using the radiation beam of the linear accelerator. These devices are typically made of an array of amorphous silicon photodiodes with good spatial resolution and are attached to most modern linear accelerators which therefore requires little setup and acquisition time for the purposes of dosimetry [45]. The EPID is often used for mechanical QA checks such as determing the location of the linear accelerator isocentre and measurements of MLC leaf positions and movement. A significant amount of research has been done to use these imaging devices for 2D dosimetry but they do suffer from some energy dependence due to the lack of water equivalence of the detectors and require correction for ghosting and image lag in dosimetry measurements [46]. Like film, EPID dose measurements are not able to measure integrated dose over different gantry angles as they are fixed in position in the radiation beam's eye view, as seen in figure 1.1a. They are therefore limited to measuring 2D dose maps at individual gantry angles and not capable of performing a true 3D dose measurement, although it is possible to use a set of 2D EPID measurements to make 3D and 4D

dose reconstructions [47, 48]. Given the position of the EPID beyond the treatment couch they are uniquely able to acquire dosimetric information during treatment with a patient on the couch and without any interference to the beam delivery. For this reason, in-vivo EPID measurements to verify delivery during patient treatment have recently been introduced into clinical practice [49, 50].

Another option for 2D dose measurement is with an array of point detectors such as silicon diodes or ion chambers. Commercial examples of this include the MapCHECK (Sun Nuclear Corp., Melbourne, FL) dosimeter, which is a 2D array of silicon diodes [41], or the MatriXX (IBA Dosimetry, Schwarzenbruck, Germany) dosimeter, a 2D array of ion chambers [51]. These types of detectors are easy to setup and acquire data with and, given that they are commercial products, come with user friendly software to acquire and analyze dosimetric measurements. Given the size and cost of the detectors used they have limited spatial resolution and require corrections to the individual point measurements. Two-dimensional detector arrays such as these are often used during machine QA to quickly measure the flatness and symmetry of the beam profile and ensure that it falls within a pre-determined tolerance.

3D Detector Arrays

In treatments with dynamic gantry motion such as VMAT, 1D and 2D dosimeters fall short in capturing the integrated dose distribution; the measurement of a static fields at each gantry angle is simply not possible when the gantry is continuously rotating. It has also been suggested that 3D dose measurements may even be necessary for IMRT delivery verification as 2D planar dosimetry may not be able to predict clinically relevant dose errors [52–54]. For this reason, a number of non-planar detector arrays have recently emerged to address this potential dosimetry need. These include the commercially available diode arrays, ArcCHECK (Sun Nuclear Corp., Melbourne, FL) [55] and Delta^4 (ScandiDos AB, Uppsala, Sweden) [56], and Octavius 4D (PTW, Freiburg, Germany) [57], a planar array of ion chambers that rotates synchronously with the gantry during a VMAT or IMRT delivery. The ArcCHECK dosimeter consists of silicon diodes that are arranged in a helical array embedded in an acrylic phantom with a 15.5 cm diameter cavity at the centre as can be seen in figure 1.5. The cavity in the ArcCHECK phantom can be filled with an acrylic plug to avoid the large air gap, but in either case there are no detectors within the central region of the dosimeter. Delta^4 is also an acrylic phantom, but with two intersecting perpendicular

planar arrays of diodes. With these arrays the diode measured dose is corrected in real time for factors including temperature, beam direction, field size, and depth; to facilitate some of these corrections the linear accelerator gantry angle is determined by beam entry and exit diode measurements on the ArcCHECK and with a physical inclinometer attached to the gantry in the case of Delta^4. There have been many studies validating both ArcCHECK and Delta^4 as pretreatment verification devices for both IMRT and VMAT deliveries [58–63]. Although these detector arrays provide more information than strictly 2D dosimeters and are a better option for more complex deliveries like VMAT, they cannot be considered true 3D dosimeters. Given the cost of individual detectors and limitations in embedding them within a phantom the spatial resolution of these dose measurements is relatively low and provides only a sample of the agreement between planned and delivered treatments. Additionally, the phantom and detectors are not tissue equivalent and although correction factors are able to account for the effects of this, in an ideal scenario a dosimeter's composition would be near tissue equivalent.

3D Dose Reconstruction

One way to achieve 3D dosimetry is the combination of both measurement and calculation to reconstruct a 3D dose distribution based on an array of point measurements. The ArcCHECK's rotationally symmetric design makes it possible to be used in conjunction with a software called 3DVH (Sun Nuclear Corp., Melbourne, FL), which calculates 3D dose for VMAT treatment verification [64, 65]. The 3DVH software reconstructs a 3D dose distribution by taking dose calculated by the TPS and perturbing it using measurements from the ArcCHECK's helical diode array; Delta^4 has a similar program called Delta^{4DVH} [66]. In both cases the software also has the option to reconstruct dose directly into patient anatomy by taking TPS calculations and diode measurements of the delivery. Another dose reconstruction method exists using an EPID which uses the measurements from individual IMRT fields to reconstruct the dose into a virtual cylindrical water phantom [67]; a similar dosimetry system has been developed for VMAT deliveries [68]. While these types of dose calculations and reconstructions are certainly of clinical value, they are not true 3D measurements but predictions of dose based on a limited set of data. The verification of a complex treatment plan would ideally involve a true 3D dosimeter.

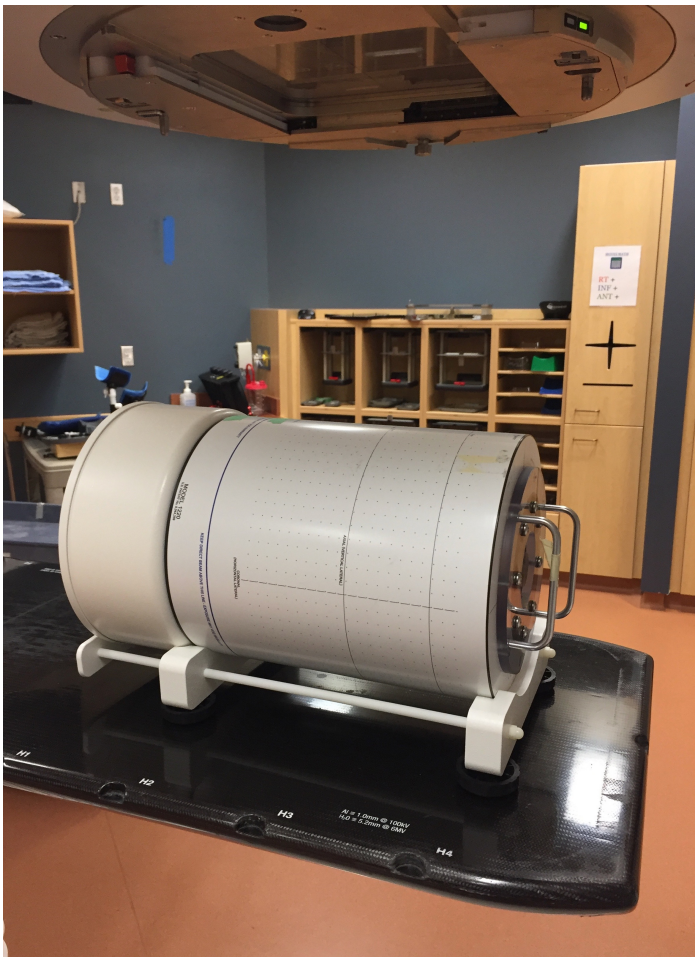

Figure 1.5: Image of the ArcCHECK detector setup on the linear accelerator couch.

3D Dosimeters

True 3D dosimetry in modern radiation therapy involves either radiochromic dosimeters or polymer gel dosimeters. Radiochromic 3D dosimeters include micelle gels [69, 70], silicone based dosimeters [71, 72] and a dye-based polyurethane dosimeter called PRESAGE® [73]. In micelle gels a radiochromic leucodye is dissolved in micelles dispersed throughout an aqueous gel, in silicone based gels the leucodye is dissolved in chloroform with a silicone elastomer serving as the 3D matrix and in PRESAGE® gels the polyurethane of the dosimeter is doped with a leucodye. In these radiochromic dosimeters, the leucodyes change colour when exposed to radiation and this change can then be read out by an optical CT scanner.

Polymer gel dosimeters are 3D, tissue equivalent, dosimeters that have excellent spatial and dosimetric resolution. These characteristics make them unique in the world of radiation dosimetry and provide advantages over many other dosimeters. The flexible nature of the gelatin matrix also make polymer gels an interesting candidate for the validation of deformable or four dimensional (4D) dose calculation. After irradiation polymer gels are generally imaged using x-ray CT, optical CT, magnetic resonance imaging (MRI) or ultrasound imaging to extract the relevant dosimetric information [34]. The fabrication, irradiation and readout of gel dosimeters is often labour and cost intensive, limiting their use as an everyday QA tool. However, the positive attributes of polymer gels make them a potentially powerful tool for commissioning new delivery techniques or dose calculation methods and end-to-end dosimetry tests. A detailed overview of polymer gels and x-ray CT readout will be discussed in Chpater 2.

1.3 Dissertation Scope and Motivation

Given the recent advancements in radiation therapy it is clear that the tools of radiation dosimetry must evolve to meet the ever changing needs for safe and effective delivery of radiation treatments. To this point radiation dosimetry has managed to meet the demands imposed by these technological advancements, but one could argue with the adaptive radiation therapy and dose warping calculations that delivery and calculation techniques have moved beyond the ability to verify their reliability. It is also conceivable that radiation delivery techniques will continue to advance and grow more complex and for patients to see the benefit from these future developments there

must be more sophisticated dosimetric tools in place.

The work presented in this dissertation investigates the use of a polymer gel dosimetry system for clinical applications and in particular for deformable dose verification. This dosimetry system was previously investigated by University of Victoria student Dr. Holly Johnston. This type of gel is designed to be read out by x-ray CT imaging and has improved dose sensitivity over previous x-ray CT gels [74]. The previous work on this gel system focused on initial characterization of the gel response, the use of multi-slice CT scanning techniques for gel read out and other issues associated with the gel response. This work will move towards determining the clinical applications of this system and what role it may have in radiation dosimetry.

Chapter 2 provides background information on polymer gel dosimetry and other 3D dosimeters, x-ray CT imaging, deformable dose calculation and reviews the current state of clinical applications using 3D dosimetry. Chapter 3 describes the materials and methods used in this work that are common to the subsequent results chapters. Chapter 4 presents the results of a study to assess the reproducibility and accuracy of the static gel dosimetry system. In this work the ability for inter-batch and generic dose calibration of the system is explored and what effects these calibration methods have on the overall accuracy of dose measurement. These results provide context for the gel measurements in subsequent chapters and gives some insight into what type of clinical role this system may have. Chapter 5 details the development of the first 3D deformable dosimetry system based on x-ray CT polymer gel dosimetry and establishes the setup reproducibility, deformation characteristics and dose response of the system. This work establishes several important characteristics of the new system and sets up its use for future clinical applications, including the validation of deformable dose accumulation algorithms. Chapter 6 presents the results of the first attempt to utilize the deformable dosimeter to measure deformed dose and a comparison of this measured dose to that calculated using a deformable dose accumulation algorithm. With these results, areas of disagreement between calculation and measurement are investigated to determine what steps can be taken to improve them. Finally, Chapter 7 summarizes the conclusions of the work presented in this dissertation and considers what future steps may be taken with this dosimetry system.

Chapter 2

Background

This chapter gives a general overview of the major components of the dosimetry system investigated in this work and describes how similar dosimetry systems are implemented in clinical applications and research. Section 2.1 describes the history and development of polymer gel dosimetry and other 3D dosimeters, including a general overview of the different procedures and readout methods that can be used. Section 2.2 is an overview of x-ray computed tomography (CT) imaging and how it applies to radiation therapy and polymer gel dosimetry. Section 2.3 describes Monte Carlo dose calculation methods and its clinical impact including the more recent development of deformable dose calculation algorithms. Section 2.4 is a literature review of the most recent clinical applications and research in polymer gel dosimetry and 3D dosimeters.

2.1 Polymer Gel Dosimetry

In general, gel dosimetry can be described as the measurement of chemical changes that occur within a material when it is exposed to ionizing radiation, where the chemicals that undergo these changes are often infused in a gelatin or agarose matrix to provide 3D information. The information stored within the dosimeter can be read out and related to absorbed dose by use of a calibration curve which can be obtained by exposing one or more gel phantoms to predefined amounts of radiation. Although the radiosensitive chemicals that are used or method to read out this information can vary from dosimeter to dosimeter the general principle remains the same.

2.1.1 History

The first use of radiosensitive chemicals to form a gel dosimeter was in 1950 by Day et al., who showed that dyes such as methylene blue would change colour when exposed to ionizing radiation [75]. In 1957, Andrews et al. measured electron and photon depth dose profiles using gels containing chloral hydrate that were read out using spectrophotometry and pH measurements [76]. Gel dosimetry using polymers was introduced in 1954 by Alexander et al. who showed that polymethylmethacrylate would cross-link when exposed to ionizing radiation and had potential for radiation dosimetry [77]. In 1958, Hoecker et al. investigated the use of polymer dosimetry in liquids [78] and Boni developed a polyacrylamide based dosimeter for gamma dosimetry in 1961 [79]. So the underlying principles of polymer gel dosimetry had been established around the middle of the 20th century but, without the ability to easily measure 3D dose distributions with these tools, their potential was limited.

Modern gel dosimetry began in 1984 when Gore et al. showed that the previously discovered Fricke dosimeter [80], where ferrous ions in a ferrous sulphate solution were converted to ferric ions when irradiated, could be imaged using magnetic resonance imaging (MRI) to measure radiation exposure [81]. To maintain the spatial information of the irradiated dosimeter, the ferrous sulfate solution was infused into a gelatin matrix. Further study of the Fricke-gel dosimeter showed that the diffusion of the converted ferric ions in the gelatin matrix was too high which compromised the spatial integrity of the dosimeter [82] and attempts to remedy this issue were unsuccessful. Although ultimately unsuccessful at the time, the concept of reading out 3D information from these Fricke-gel dosimeters using MRI was an important step for 3D dosimetry.

Polymer gels were first introduced in 1992 by Maryanski et al. with a recipe consisting of acrylamide (AAm), N,N'-methylenebisacrylamide (BIS) and agarose [83]. The acrylamide served as a linear monomer, the BIS as a cross-linking monomer, and the two formed a polymerized network within the agarose matrix when exposed to radiation. Like Fricke gels, the dose information was read out using MRI. The polymer gel dosimeter demonstrated superior spatial integrity as the highly crosslinked polymer aggregates were entangled within the gel matrix. The presence of oxygen in these gels was found to terminate polymer chains and limit the amount of polymerization that could occur and this meant the gels needed to be fabricated and stored in an oxygen-free environment [84, 85]. In future work, gelatin replaced agarose as

the matrix for the monomers and this was the beginning of polyacrylamide gel (PAG) dosimetry [86]. Following the establishment of PAG gel dosimeters in combination with quantitative MRI read out, a number of studies were undertaken to investigate the accuracy of this type of dosimetry system and the different clinical applications it could be used for [34].

Although MRI was the method of choice for a long time to read out gel dosimeters, other imaging modalities emerged, in part due to the limited availability and cost of MRI. In 1996, Gore et al. and Maryanski et al. investigated the use of optical CT imaging as a readout method which measures the change in opacity that comes with gel polymerization [87, 88]. In 2000, Hilts et al. introduced the use of x-ray CT imaging as read out method to measure changes in electron density caused by gel polymerization [89]. Although other read out methods such as Raman spectroscopy [90] and ultrasound imaging [91] have been used to image gel dosimeters, MRI, optical CT, and x-ray CT are the three main modalities used in modern gel dosimetry and each will be investigated in more detail later in this chapter.

An important step in the development of gel dosimeters came with the development of a new type of gel by Fong et al. in 2001 that could be fabricated in a normal oxygen, or 'normoxic', environment [92]. This gel formulation used ascorbic acid to bind free oxygen and prevent the terminatination of polymerization reactions. Another compound, tetrakis (hydroxylmethyl) phosphonium chloride (THPC), has also been shown to work as an effective oxygen scavenger in PAG dosimetry [93, 94]. Gels that use oxygen scavengers and are fabricated in normoxic environments are known as normoxic gel dosimeters. The use of normoxic gels removes a layer of complexity from the already labour intensive gel manufacture process and allows for gels to be made on a bench-top in the laboratory. This is an attractive feature in regards to the implementation of a gel dosimetry system within a cancer clinic.

More recently, research in 3D gel dosimetry has focused on the radiation chemistry and investigations of new gel formulations and types of 3D dosimeters [34, 95]. There have been efforts to reduce the toxicity of PAG gel dosimeters by substituting the carcinogenic monomer acrylamide by N-isopropylacrylamide (NIPAM). This monomer, NIPAM, will be further employed in this work. [96, 97]. There has also been an evolution from polymer gels to new types of 3D dosimeters that use dyes immersed in a gel or solid plastic matrix to acquire 3D dose distributions with optical CT readout. The first dye based 3D dosimeters were Fricke gel dosimeters that included a metal ion indicator called xylenol orange which caused a visible colour change in the gel

when irradiated [98]. The addition of the xylenol orange allowed for these gels to be read out using optical CT imaging and created the first radiochromic gel dosimeter. This was followed by the development of a radiochromic plastic dosimeter containing leuco-dyes that turns green when exposed to radiation and would eventually become known as the PRESAGE® dosimeter [73]. Although not technically a gel dosimeter, PRESAGE® is a 3D dosimeter that uses the same principles as gel dosimetry and is read out using optical CT imaging. Other optically read out radiochromic dosimeters such as micelle gels [69, 70] and a silicone based dosimeter [71, 72, 99, 100] have been introduced with the emergence of the optical CT read out method.

2.1.2 Polymer Gel Chemistry

When a polymer gel dosimeter is irradiated the water within the gel undergoes radiolysis generating highly reactive radicals given by the following equation:

$$H_2O \longrightarrow 2R^{\bullet} \tag{2.1}$$

where the dissociation of water molecules is proportional to the absorbed dose and creates reactive intermediates $R^{\bullet}$ [34]. The radicals can then initiate the polymerization of monomers in the following step:

$$R^{\bullet} + M \longrightarrow M^{\bullet}, \tag{2.2}$$

generating a monomer radical, $M^{\bullet}$, which can subsequently react with another monomer creating a polymeric radical. These polymeric radicals can react further, adding more monomers in chain propagation. A general equation for this can be seen in the following equation:

$$M_m^{\bullet} + M_n \longrightarrow M_{m+n}^{\bullet}, \tag{2.3}$$

where $M_m^{\bullet}$ is a polymeric radical with m units, M_n is a polymer chain with n units and $M_{m+n}^{\bullet}$ is the newly generated polymeric radical with $m+n$ units. For the cases of $m = 1$ or $n = 1$ these are monomer radicals and a single monomer, respectively. These polymer chains continue to grow until they are terminated by interactions with other radicals:

$$M_m^{\bullet} + M_n^{\bullet} \longrightarrow M_{m+n} \tag{2.4}$$

$$M_m^\bullet + M_n^\bullet \longrightarrow M_m + M_n \tag{2.5}$$

$$M_m^\bullet + R^\bullet \longrightarrow M_m \tag{2.6}$$

Note that a dead polymer chain can be activated by a radical:

$$M_m + R^\bullet \longrightarrow M_m^\bullet, \tag{2.7}$$

or through chain transfer:

$$M_m + M_n^\bullet \longrightarrow M_m^\bullet + M_n. \tag{2.8}$$

With the inclusion of a cross-linking monomer, copolymerization occurs and the kinetic models in the above equations become more complicated [101, 102]. Gels with a linear, non-crosslinking monomer only form linear polymer chains, and when a cross-linking polymer is added the structure of these chains becomes a crosslinked network and leads to an increase in the rate of consumption of unreacted monomers [103]. Crosslinked polymer chains are insoluble in water, and they precipitate to form microgels that influence the MR, optical and x-ray properties of the gel [103, 104].

When oxygen is present, peroxide-radicals are generated:

$$R^\bullet + O_2 \longrightarrow ROO^\bullet \tag{2.9}$$

$$M_m^\bullet + O_2 \longrightarrow M_nOO^\bullet, \tag{2.10}$$

which quickly react with other radicals leading to the termination of polymer chains [34]. This quick termination limits the amount of polymerization that occurs which can have a significant impact on the dose sensitivity of the gel. This oxygen effect is why polymer gels need to be manufactured in an oxygen-free environment or contain some form of oxygen scavenger.

2.1.3 Gel Dosimetry Procedure

Despite the variations in gel formulation and read-out methods over the history of gel dosimetry, the general workflow of this type of dosimetry has remained relatively unchanged. A general outline of the steps of this workflow are shown in figure 2.1.

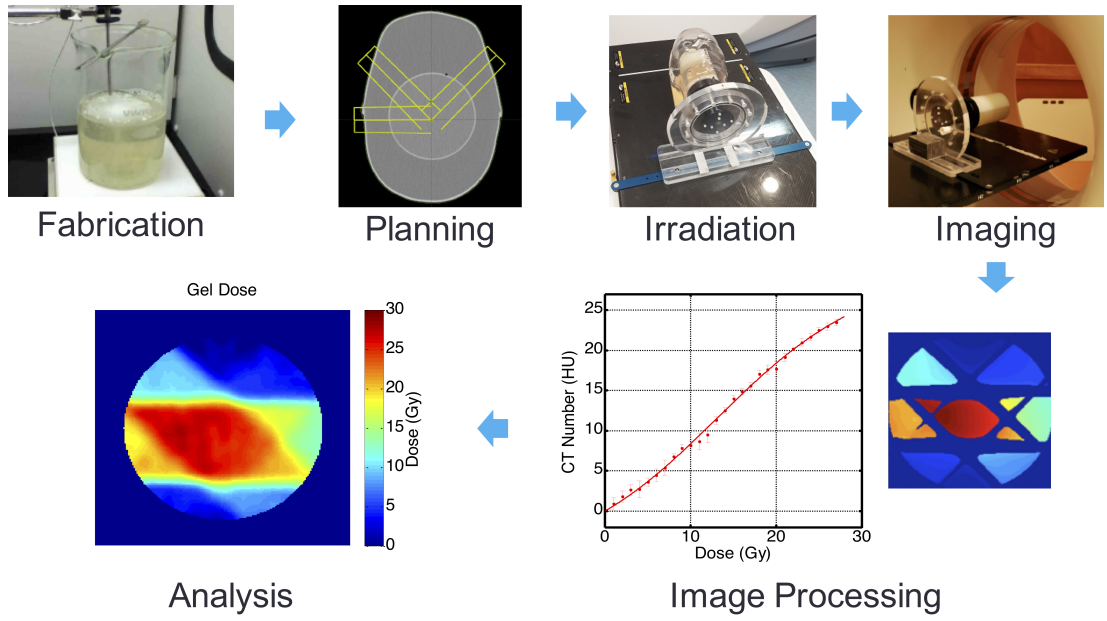

Figure 2.1: A general workflow for gel dosimeters. First a gel is fabricated and poured into a container and a plan for radiation delivery is calculated. The gel is then setup and irradiated with the desired plan and after some time, allowing for chemical changes to occur, it is read out using the appropriate imaging modality. These images are then processed and the readout information is calibrated to absorbed dose, generating a gel measured 3D dose distribution.

The first step of the procedure is to manufacture the gel, by mixing the ingredients of the gel recipe to form the dosimeter. For polymer gels the recipe generally consists of a linear monomer, a cross-linking monomer, and for normoxic gels, an oxygen scavenger. Once the gel is fabricated it is poured into a container and then stored for a period of time to allow the chemicals and structure to set prior to irradiation. The type of storage container and conditions for storage will vary and depend on the dosimetry application and the type of gel being used.

At this time, or possibly prior to fabrication, the irradiation pattern that is to be delivered to the gel must be planned and the dose for this plan calculated. This planning and dose calculation is done using CT images of the gel dosimeter that is to be irradiated, or images of a dosimeter with identical shape and composition. This plan, determined by the treatment planning system (TPS), not only gives the linear accelerator directions for radiation delivery, but is also the basis for producing a dose calculation which is often to what the gel measured dose will be compared.

The gel is then irradiated with the determined plan and then allowed to sit while reactions within the dosimeter caused by the radiation occur, producing changes to the dosimeter's structure. For polymer gels this is the process of building polymer chains from the monomers within the gel and these reactions generally stabilize after a period of 15 to 24 hours [34]. Once these changes have stabilized the dosimeter can then be read out by the appropriate imaging modality, this is primarily MRI, optical CT, or x-ray CT.

The set of readout images is then processed and some form of calibration is applied to convert the imaging information to absorbed dose within the dosimeter. A calibration is often achieved by delivering a simple plan to a gel for which the dose can be reliably and accurately calculated and by comparing the calculated dose to the read out information of the gel irradiated with this simple plan. With this calibration established the dosimeter can then be used in subsequent measurements to evaluate more complicated dose deliveries.

After read out, image processing and calibration a 3D dosimetric map of absorbed dose to the gel is obtained. This 3D dose map can then be compared to dose calculated by either the TPS or Monte Carlo or to dose measured by another dosimetry tool.

2.1.4 Imaging Methods

The three main imaging modalities for gel dosimetry read out are MRI, optical CT and x-ray CT. This section will give a brief overview of MRI and optical CT while x-ray CT, the imaging modality used in this work, is described in more detail in section 2.2.

MRI

Magnetic resonance imaging takes advantage of the phenomenon of nuclear magnetic resonance (NMR) within the nucleus of the atom. The protons and neutrons in the atomic nucleus possess a magnetic dipole moment and this magnetic moment describes the magnetic field properties of the nucleus and depends on the number of protons and neutrons. The simplest example of this is hydrogen which, in its most common isotope, consists of a single proton with an orbiting electron. Hydrogen is abundant within the human body and produces a large magnetic moment, so therefore the proton is the principal element used in MRI. Normally, the magnetic moments of hydrogen atoms in tissue are oriented in a random manner and no net magnetic signal can be detected. When a strong external magnetic field, B_0, is applied these magnetic moments become aligned parallel, or anti-parallel to B_0. The parallel orientation is the lower energy state and a majority of proton magnetic moments are in this state, the ratio of which depends on the temperature of the material and the strength B_0. The stronger the external magnetic field the more protons are aligned in the parallel state. Although the magnetic moment of a single proton is not detectable but the combination of many proton moments when added, can be observed [105].

The external magnetic field also applies a torque to the protons which produces a precession in the direction of the magnetic moment, causing it to rotate about the axis of the external magnetic field. The precession frequency, ω_0 is proportional to the external magnetic field, B_0:

$$\omega_0 = \gamma B_0, \tag{2.11}$$

where γ is the gyromagnetic ratio and is a physical property of each element. In a given element the protons will precess with the same frequency but out of phase, as the phase of the precession is distributed randomly. This random distribution of precessions is the equilibrium state of the material and the net magnetization from the combined proton magnetic moments will be in the same direction as B_0 because the

random distribution of transverse magnetization will add to zero. A radiofrequency (RF) pulse with a frequency that matches that of ω_0 can be applied to transfer energy to protons causing their precessions to synchronize and produces a net magnetic field perpendicular to B_0, known as a transverse magnetization. The return from this perturbed state to equilibrium is what produces the NMR signal. The localization of these NMR signals is possible because ω_0 is directly proportional to the applied magnetic field. By applying a magnetic field gradient in 3D, each location within the imaged volume will have a different ω_0 and the frequency of the RF pulse required to generate a signal will determine the location of the signal. The localization of these NMR signals in a 3D volume is the basis for the production of MR images [105].

In PGD, the amount of polymerization within a gel dosimeter is measured using the T_2 relaxation time, which is a measure of the time it takes for magnetic moments to lose phase coherence with one another. Specifically, T_2 is the elapsed time between the peak transverse magnetization signal and 37% (or $1/e$) of the peak signal. The relaxation time is often quoted as a relaxation rate, R_2 which is equal to the inverse of the relaxation time ($R_2 = \frac{1}{T_2}$) [34, 106]. This relaxation occurs due to magnetic inhomogeneities within the material causing the precession of individual magnetic moments to speed up and slow down and therefore lose coherence; this occurs more quickly when molecular motion is limited and the magnetic field variations manifest more easily. When polymerization of an irradiated gel occurs and monomers grow into cross-linked polymer chains, molecules within the gel become less mobile which causes the relaxation time, T_2, to decrease and R_2 to increase. This increase in R_2 can be then be related to amount of polymerization that has occurred and therefore to the dose absorbed within the gel.

MRI was the original read out method for gel dosimeters and initially the most widely used and there is therefore a large amount of research into the use of MRI read out gels [34]. However there are some significant challenges in MRI gel read out that can make its use unappealing. It has been shown that gel temperature during MRI read out can have a drastic effect on dose response with a temperature variation of 1° C leading to errors of up to 15% [107]. For that reason it is critical that the temperature of the gel dosimeters is stable and uniform throughout the dosimeter during during the sometimes lengthy MR imaging sequence [108]. It therefore has been suggested then that these gels should be stored in the MRI scanning room for a day or more prior to read out and in some cases actively heated or cooled during the scanning process [34, 107]. It also requires careful control of temperature between

calibration and test gel batches to avoid dosimetric errors and in most cases it is recommended to scan calibration gels with test gels at the same time [34]. It should be noted that there are also compensation strategies on the MRI pulse sequence which can help in making the gel dosimeters less susceptible to any temperature drift [109]. Practically speaking, MRI is primarily used a diagnostic tool and not for quantitative measurements, so modifications in setup and imaging methodology are required for gel dosimetry and additional QA of the quantitative measurements may be necessary. These considerations along with the limited availability of MR imaging make the implementation of gel dosimetry within a working radiation therapy department a challenge and has led to the investigation of other read out modalities.

Optical CT

Optical CT imaging is an emerging read out imaging modality for PGD and 3D dosimeters in general. In optical laser CT scanning the amount of light transmitted through an object is measured by scanning a laser across the volume of the object. The optical attenuation, μ, of a material can then be determined using the equation:

$$I_t = I_0 e^{-\mu x}, \tag{2.12}$$

where I_0 and I_t are the initial and transmitted intensity of light, respectively and x is the path length through the material. For an inhomogeneous material, a ray of light can pass through several regions of differing optical attenuation before exiting the object. If the path the light takes is broken into equal size path lengths, Δx, the equation becomes:

$$I_t = I_0 e^{-(\mu_1 \Delta x + \mu_2 \Delta x + \mu_3 \Delta x + \ldots + \mu_n \Delta x)}, \tag{2.13}$$

and the total attenuation for the ray, μ, is equal to:

$$\mu = \mu_1 + \mu_2 + \mu_3 + \ldots + \mu_n, \tag{2.14}$$

where μ_i is the optical attenuation of layer i with thickness Δx.

The goal of optical CT is to take measurements of I_t and I_0 and derive a map of attenuation coefficients, μ, throughout the object being scanned [34, 110]. This is done by taking multiple transmission measurements through one slice of an object to develop a 1D projection of optical attenuation values and then by taking multiple projections through this slice from different angles around the object, a 2D map of

attenuation values can be obtained through a process called backprojection. Measurements at multiple slices of the object will generate layers of 2D attenuation maps from which a 3D distribution of optical attenuation values can be built. This process is discussed in greater detail in section 2.2.2 on the subject of x-ray CT imaging which has an analogous image reconstruction process.

When a polymer gel is irradiated the polymerization causes an increase in optical attenuation as the gel becomes more opaque in irradiated regions. This optical attenuation can be related to the amount of polymerization (or colour change for radiochromic dosimeters) that has occurred within the dosimeter and therefore related to the absorbed dose. So, by taking an optical CT scan of an irradiated gel and using an appropriate calibration, one can generate a 3D map of the absorbed dose within the gel. The majority of attenuation that occurs within a polymer gel is due to the scattering of light caused by polymerized gel [34, 110]. This can cause artifacts in image reconstruction when scattered photons can return to the beam's path via multiple scattering interactions. Refraction of light is also an issue in optical CT measurements as refractive index changes at the edge of the dosimeter container need to be corrected for and radiation induced refractive index changes within the dosimeter itself can also lead to refraction of light and imaging artifacts [34, 111]. These issue have led to an increase in the use of dye-based dosimeters with optical CT read out where the primary cause of light attenuation is via absorption rather than scatter [69, 70, 73, 98].

One practical issue of the optical CT read out method is that it is a relatively new imaging technique and one that is only used for the read out of 3D dosimeters. Therefore, optical CT read out gel dosimeters require either the purchase or construction of a dedicated scanner and the development of an in-house code to reconstruct and process the images. This differs from x-ray CT read out gels where the majority of the equipment is already in place at a working cancer clinic. In addition to this, since an optical CT scanner is outside the clinical treatment chain a layer of uncertainty is added to the read out measurements in terms of setup and handling, whereas for MRI and x-ray CT imaging, these systems are already integrated into the clinical workflow.

2.2 X-ray Computed Tomography

X-ray computed tomography (CT) is an extensively used medical imaging technique which has many clinical applications including use in the diagnosis of cancer. It was the first imaging modality that allowed for deep, non-invasive views into human body, providing a slice-by-slice set of 2D images of a patient [105]. X-ray CT scanners use the attenuation of x-rays to generate images and like the visible light used in optical CT, the transmission of x-rays through a patient or phantom is measured by an array of detectors at different angles around the object of interest. Each set of x-rays that are detected from a given angle is called a projection and the data from thousands of projections around the object is used to reconstruct a 2D image of the linear attenuation coefficient for each point within the plane parallel to x-ray beams used in the scan. This section will give an overview of the development of x-ray CT imaging, describe the process of how CT images are formed, provide some context as to how this imaging modality is applied in radiation therapy and how it is used in polymer gel dosimetry.

2.2.1 History

The theoretical idea of tomography was first developed by mathematician Johann Radon in 1917 who proposed that an image could be formed if one had an infinite number of projections of an object. It wasn't until 1956 that Allan Cormack began to apply the principles of tomographic reconstruction to projections produced by x-rays, which led to the construction of a CT prototype in 1963. Independently of Cormack's work, Godfrey Hounsfield in 1967 began research in tomography, using gamma radiation, and developed the first clinical CT scanner, which imaged its first patient in 1971. In 1979 Hounsfield and Cormack were jointly awarded the Nobel Prize in Medicine "for the development of computer assisted tomography". From the first clinical scan in 1971 the CT scanner began to develop rapidly as new and improved scanner designs and scanning geometries were developed reducing image acquisition time and improving image quality as a result [105, 112].

Hounsfield's original scanner employed a rotate/translate pencil beam system, where the x-ray tube and a single detector translate across the field of view producing a series of parallel rays and then rotate and translate back across the patient to generate a second projection. This process is repeated over 180 projections at 1° intervals. This geometry can be seen in figure 2.2a and is now known as a first-

generation CT scanner. With 160 rays per projection, 28,800 rays were measured per slice by the single detector [105]. The NaI detector used had an "afterglow" effect, meaning that two measurements could not be taken over too short a time interval without carryover from the previous measurement [105]. The first image taken on this scanner had an acquisition time of 4.5 minutes and it took 20 seconds to reconstruct the 80 x 80 pixel image with a pixel size of 3 $\times$ 3 mm [112].

The next advance in CT scanners was to a rotate/translate fan beam geometry which is called the second generation and can be seen in figure 2.2b. This system used the same geometry as the first generation but the pencil beam was replaced by a narrow fan beam with an angle of 10 degrees that could cover a larger portion of the FOV at one time and the single detector was replaced by an array of 30 detectors to take transmission measurements from the entire fan beam [112]. This allowed for more rays and projections to be taken in a shorter period of time, allowing for faster scanning time and improved image quality. With 600 rays measured per projection and 540 projections used to acquire each slice, the number of rays measured per slice with the second generation scanner increased to 324,000 and the scanning time could be reduced to as low as 18 seconds per slice [105]. The decrease in scan time not only reduced motion artifacts in images but allowed for the potential of breath-hold imaging protocols as it would be possible for some patients to hold their breath over the duration of a scan. One downside to the introduction of fan beam imaging is an increase in scattered radiation contaminating direct ray measurements with the large detector area and beam size compared to first generation scanners.

By 1976 the most significant contribution to scan time, translational motion, was eliminated in third generation CT scanners which introduced a rotate/rotate geometry as can be seen in figure 2.2c. In this design both the x-ray tube and array of detectors rotate continuously around the patient and the fan beam angle was widened so that it could cover the entire field of view at one time. The new design required a much larger array of detectors and the number of detector elements increased more than ten-fold, up to 1000 in some cases [112]. The increasing number of detectors led to costlier CT scanners but allowed for an increase in image quality and decrease in scan time as more data could be acquired in less time. Initially these systems could scan patients in less than 5 seconds and modern third generation scanners can do so in less than one second [105]. With a larger detector array this geometry is even more susceptible to scattered photons entering the primary beam than previous generations and due to the nature of the fixed source-detector setup is also susceptible to ring

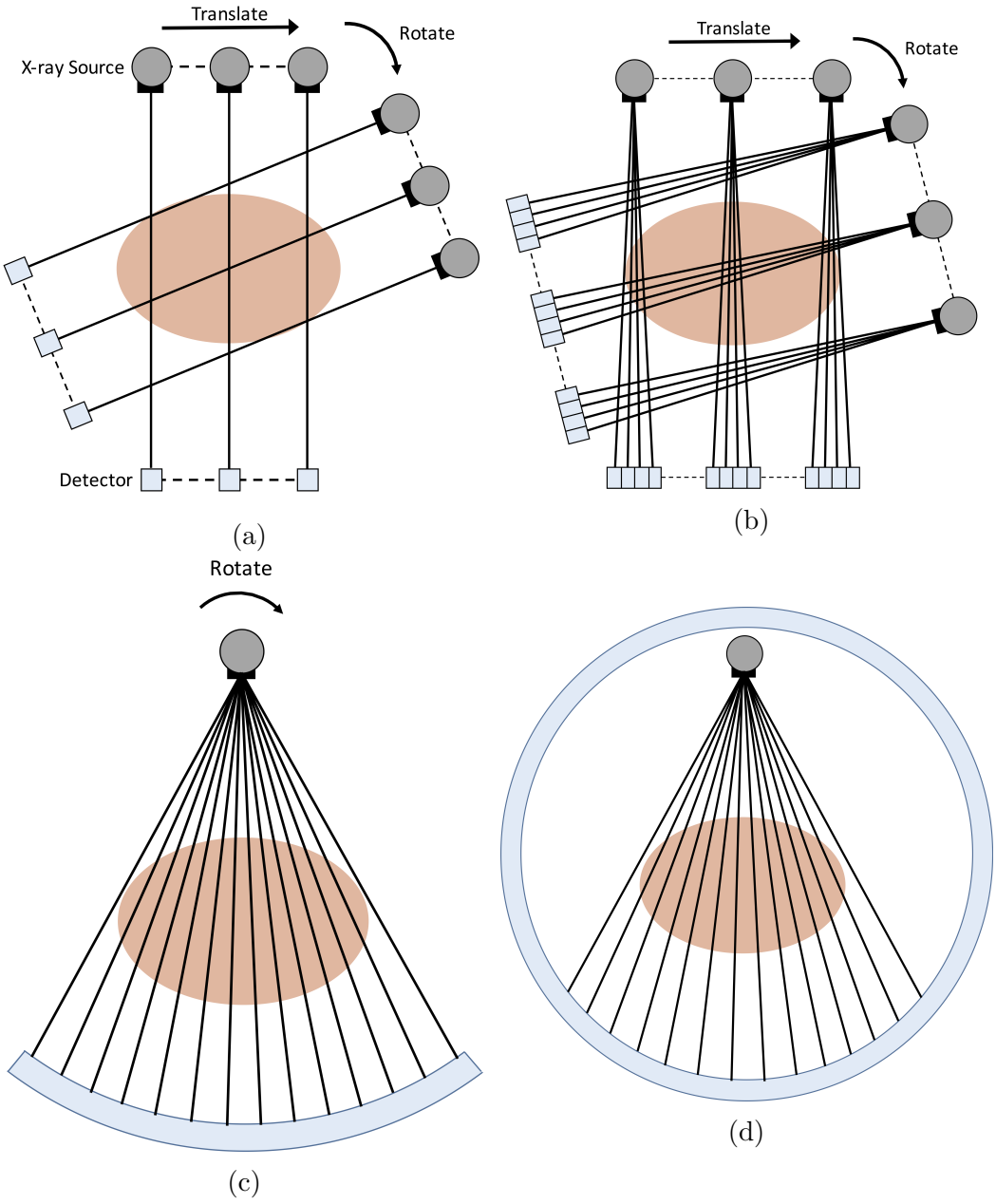

Figure 2.2: Examples of (a) a first generation CT scanner translate/rotate geometry with a single detector and pencil beam, (b) a second generation CT scanner translate/rotate geometry with a detector array and narrow fan beam, (c) a third generation CT scanner rotate/rotate geometry with a large detector array and wide fan beam, and (d) a fourth generation CT scanner rotate/stationary geometry with a stationary ring of detectors that surround the entire patient and a rotating fan beam source.

artifacts. Ring artifacts are generated when there is a difference in gain for a detector element in the array so all rays measured by this detector are miscalibrated, creating a ring in the image during backprojection.

In an effort to eliminate ring artifacts in CT images, the fourth generation of CT scanners were designed with a rotate/stationary design where the rotating array of detectors was replaced by a stationary ring of detectors that completely surround the field of view as can be seen in figure 2.2d. With this geometry each stationary detector element measures the incoming x-rays from different angles so that the reference intensity, I_0, and transmission intensities, I_t, for a given projection are measured by the same detector element. This eliminates the issue of gain differences between detectors elements, effectively eliminating ring artifacts. However, this new design drastically increased the number of detectors, up to 5000 detector elements for some scanners, and therefore drastically increased the cost of the scanner [112]. As detector technology and calibration methods improved, ring artifacts in third generation scanners could largely be eliminated and fourth generation scanners became largely unnecessary [105].

The rotate/rotate geometry of third generation CT scanners are primarily used in diagnostic and radiation therapy simulation scanners today although there have been other advances in CT scanner technology. For example, many modern CT scanners have the capability to perform helical image acquisitions where the couch and patient move through the bore of the scanner while data is being acquired. A helical scan can acquire multiple image slices in a fraction of the time it would take to image single slices with couch shifts between each slice acquisition. This reduces overall imaging time and can therefore reduce the amount of contrast agent needed in some patients or allow for an entire exam to be performed with the patient's breath held reducing variation in patient anatomy between image slices [105].

Another common feature in today's CT scanners is the ability to measure multiple slices at one time with the use of multiple detector arrays. Traditionally single slice CT scanners control the thickness of image slices solely through collimation of the primary x-ray beam. For example, to achieve a 2.5 mm slice thickness the beam is collimated such that it is 2.5 mm wide at the detector surface which is just a single array of detectors. A multiple detector array has more control and flexibility in regards to determining the slice thickness of CT images. Consider a multiple detector array with 16 detector arrays, each 1.25 mm thick; the collimation of the beam can be set to 20 mm wide and the detectors in the array can be combined in many ways

to set the slice thickness. Each detector array can measure its own slice producing 16 slices each 1.25 mm thick per gantry rotation, or the detector arrays can be combined to image 8 x 2.5 mm slices, 4 x 5 mm slices, 2 x 10 mm slices or 1 x 20 mm slice. A simplified visualization of this type of detector can be seen in figure 2.3. The beam can still be collimated to smaller sizes providing even more options for slice thickness and number of slices imaged per gantry rotation. Multiple detector arrays not only allow for faster scanning times by scanning multiple slices at one time, but also use the x-ray beam more effectively as opposed to collimating a significant portion of beam and imaging slices one at a time. Effective use of the x-ray beam is an attractive feature as x-ray tube overheating and cooling is an important factor for modern CT scanners [105].

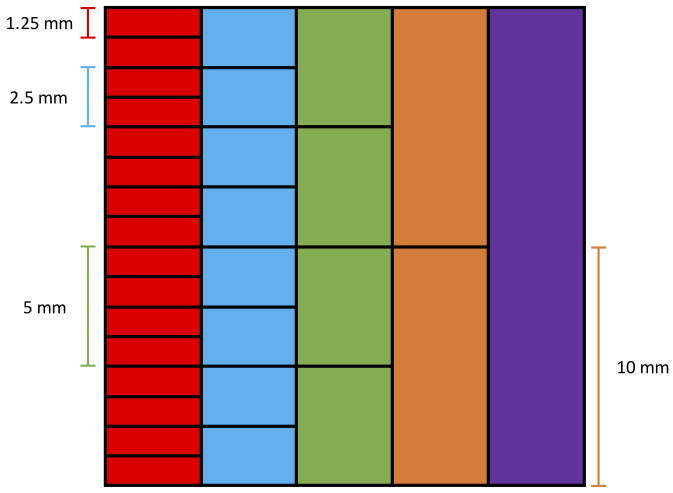

Figure 2.3: A visualization for how a multislice detector determines slice thickness. The entire width of the detector is 20 mm and is made up of 16 individual detector elements, each 1.25 mm in width. The red alignment is each detector element measuring its own 1.25 mm slice, the blue alignment combines detector elements in groups of 2 to measure 2.5 mm slices, the green alignment combines detector elements in group of 4 to measure 5 mm slices, the orange alignment combines detector elements in groups of 8 to measure 10 mm slices, and the purple alignment combines all 16 detector elements to measure one slice 20 mm in width.

2.2.2 Imaging Technique

In a modern third generation CT scanner, once a patient has been set up for image acquisition and a scanning protocol has been initiated, the gantry that houses the x-ray source and detector array begins to rotate around the patient. This rotation

allows the scanner to acquire thousands of projections around the patient within approximately one second of the start of x-ray generation. When gantry has reached the appropriate rotational speed an x-ray tube begins to generate the x-rays that will be used to image the object inside the scanner. After all the projections have been acquired the x-ray beam will turn off and the couch will translate in the axial, or z-, direction so that the next section, or slice, of the patient can be imaged. This process is repeated until the desired volume of the patient has been scanned. The acquired data is then reconstructed using a filtered backprojection into a set of contiguous 2D images, one for each slice of the patient that was imaged.

X-ray Generation

X-rays are generated by accelerating electrons towards a metal target and converting the kinetic energy of the electrons into high energy photons in a process called Bremsstrahlung radiation. This is the same process used to generate photons in a linear accelerator, however x-rays generated for imaging are much lower energy than those used for radiation therapy. The x-ray beam for a CT scanner is generated by an x-ray tube, which consists of an anode and cathode housed in an evacuated metal envelope. The cathode is made up of a tungsten filament which is heated to generate electrons via thermionic emission. A large voltage is applied across the anode and cathode causing the electrons to accelerate towards an angled anode which has a metal target, generally made of tungsten or other high atomic number material [5, 105]. When the accelerated electrons hit the target a beam of Bremsstrahlung photons is generated and directed perpendicular to the travel of the electrons towards an output port in the x-ray tube. The output port contains a filter that will harden the x-ray beam by removing low energy photons to reduce dose to the patient. The energy spectrum of the photon beam depends on the kinetic energy of the electrons and is designated by the voltage used to accelerate the electrons. On a typical CT scanner this value will vary between 80 and 140 kV and a 140 kV tube voltage, for example, will generate a photon beam maximum energy of 140 keV and, depending on filtration, a mean energy between one-third and one-half of the maximum energy [5, 105]. The electrons that hit the target generate a significant amount of heat that if left unchecked, could melt parts of the target which is why tungsten, a material with a high melting point, is often used. The anode is also rotated when in use to spread the heat over a larger area of the target and the x-ray tube housing is surrounded by oil

to aid in the overall cooling of the system. As the housing and target are heated, the oil within the x-ray tube housing expands and when this expansion passes a certain threshold an interlock is activated that prevents further x-ray production until the system has cooled sufficiently.

Image Reconstruction

As discussed in section 2.1.4 with optical CT, image reconstruction in CT is based on measurements of transmission of electro-magnetic radiation through an object. In optical CT imaging, the transmission of visible light was measured producing a map of optical attenuation whereas in x-ray CT, x-ray transmission is measured producing a map of the linear attenuation coefficient. The equations for these transmission measurements are identical to equations 2.11, 2.12 and 2.13 with μ representing the linear attenuation coefficient instead of optical attenuation. The linear attenuation coefficient is defined as the fraction of photons removed from a photon beam per unit thickness, and for photons in the energy range used in x-ray CT imaging these photons will primarily be removed via the photoelectric effect and Compton scattering [5, 105].

The raw transmission measurements are preprocessed in a number of ways including performing a gain calibration of each detector element using data from air scans, interpolation over dead or malfunctioning detector elements and scatter corrections. The processed projections can then be used to reconstruct a 2D image slice in a process called backprojection which is essentially an attempt to follow the data acquisition process but in reverse. Each ray of a projection is associated with its linear attenuation measurement μ from its transmission measurement as in equation 2.11. However since the composition of the potentially heterogeneous object is not known it is impossible to know how this overall attenuation is distributed over the path of the ray. Using the known position and angle of the detector for a given ray in a projection the measured value of μ_n is backprojected along this ray with every pixel along the path assigned the measured attenuation coefficient μ_n. Every ray in every projection is backprojected in this way smearing the measured attenuation coefficients over the entire 2D slice. A simplified visualization of this process can be seen in figure 2.4. This simple backprojection method is surprisingly effective in reproducing an accurate 2D map of the slice being imaged, however it produces a $\frac{1}{r}$ blurring effect as a result of the smearing of μ along the entire ray [105]. For example,

a single point of contrast in an otherwise empty image will produce signal around the object that diminishes as a function of the distance from the object, r, making the point appear blurred.

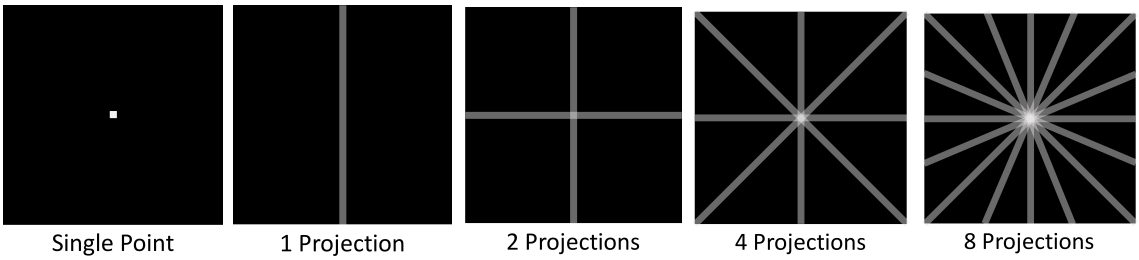

(a) (b) (c) (d) (e)

Figure 2.4: (a) a single point of contrast and reconstructions of this point using a simple backprojection with (b) 1, (c) 2, (d) 4, and (e) 8 projections. The signal from the point grows as more projections are added and the $\frac{1}{r}$ blurring effect can be seen developing from the smearing of the point along each projection.

To address the blurring effect produced in a simple backprojection a filtering step is added prior to backprojection. A filtered backprojection is then one where the original projection data $p(x)$ is convolved with the kernel $k(x)$:

$$p'(x) = p(x) \otimes k(x), \tag{2.15}$$

where $p'(x)$ is the filtered projection data that will be backprojected to produce the slice image [105, 113]. To speed up calculation times the filtering process is often performed in the frequency domain using Fourier transforms so that the original projection data and kernel in the frequency domain, $K(f)$, can be simply multiplied rather than convolved:

$$p'(x) = \mathrm{FT}^{-1}[\mathrm{FT}[p(x)] \times K(f)], \tag{2.16}$$

where $K(f)$ is the the fourier transform of $k(x)$. Some examples of filters in the frequency domain include the ramp filter, which is the ideal reconstruction filter in the abscence of noise, the Shepp-Logan filter, which has a roll-off at higher frequencies to reduce the amplification of high-frequnecy noise, and the Hamming filter, which has a more agrresive high-frequency roll off than the Shepp-Logan filter [113]. The filtered backprojection process is all performed online by the CT scanner manufacturers' software and reconstructed images of multiple slices are available within

seconds of data acquisition. Clinical CT scanners often have more than one option for convolution kernels to achieve different imaging goals. For example, a soft tissue kernel will have more high-frequency roll-off and sacrifice some spatial resolution for an improvement in signal-to-noise ratio (SNR) so that small differences in soft tissues show more contrast. A bone kernel has less high frequency roll-off and will produce sharper edges and better spatial resolution at the expense of increased noise [105]. The reconstruction algorithms and convolution kernels are proprietary information of CT scanner manufactures and detailed information about these processes are not generally released by the manufacturer.

After reconstruction is complete each imaged slice will be represented by a 2D map of linear attenuation coefficients. As a final step these values are converted to a quantity known as CT number for ease of digital display. The CT number of any pixel, $CT(x, y)$ is given by the following equation:

$$CT(x, y) = 1000\frac{\mu(x, y) - \mu_{water}}{\mu_{water}}, \tag{2.17}$$

where $\mu(x, y)$ is the reconstructed linear attenuation coefficient of the pixel and μ_{water} is the linear attenuation coefficient of water. CT numbers are measured in Hounsfield Units (HU) and the equation is defined such that the CT numbers of water and empty space are 0 and -1000 HU, respectively. The CT Numbers of clinical relevant materials can range from approximately -300 HU for lung, up to 100 HU for liver and muscle, and as high as 3000 HU for dense bone [105, 114].

2.2.3 Applications in Radiation Therapy

X-ray CT scanners play a critical role in radiation therapy. X-ray CT imaging is often involved in the diagnosis and staging of tumours and after a patient is diagnosed and radiation therapy is chosen as a course of treatment, the patient will undergo simulation on a CT scanner. The idea of simulation is to simulate the patient setup that will be used during the delivery of radiation. This is achieved through the use of lasers that are synchronized between the CT scanner room and treatment delivery room. With the patient setup in the same position and orientation as they will be for radiation delivery, a set of CT images are acquired. On this image set, an oncologist can delineate the tumor, which needs to be irradiated to a prescribed dose, and healthy tissues, for which radiation dose must be limited. This set of images, along with the contoured structures, are used to determine the plan that will be used to

deliver radiation to the patient. CT images are key to dose calculation and planning as the map of attenuation coefficients make it possible to calculate how radiation beams will be absorbed and attenuated by the various structures within the body and to therefore optimize the delivery of the radiation to achieve the desired clinical goals. It is then imperative that CT images present an accurate representation of the patient's anatomy for radiation delivery. Virtually every patient who is treated with radiation therapy undergoes a CT scan and this imaging process is directly implemented within the treatment workflow.

2.2.4 Applications in Polymer Gel Dosimetry

When polymerization occurs within a gel dosimeter after irradiation, there is a density change as described by Hilts et al [115]. This change in density is small, on the order of 1 $\frac{mg}{cm^3}$ per Gy of absorbed dose, but with the appropriate imaging and image filtering techniques it can be measured using x-ray CT [34]. The change in density will lead to an increase in physical density and therefore an increase in the linear attenuation coefficient and CT number. Images of an irradiated gel dosimeter can then be used to establish a relationship between the change in CT number, ΔN_{CT}, and the dose that was absorbed by the dosimeter and therefore generate dose calibration for x-ray CT PGD. Since the change in density is small, x-ray CT scanning protocols and post-processing of gel images are designed to maximize the low level of contrast between irradiated and unirradiated gel. Image averaging and background subtraction of an unirradiated gel are employed to reduce stochastic image noise. After scanning, image filtering and artifact removal techniques are used to further increase the signal to noise ratio [116, 117]. Newer gel formulations have also been studied and shown to have increased dose sensitivity by introducing isopropanol as a co-solvent to increase the amount of BIS that could be added to the gel mixture [118]. Another more sensitive gel formulation, using NIPAM as the linear monomer, was developed by Chain et al. and is the focus of this work [74]. In this formulation, NIPAM is the linear monomer, but also acts a co-solvent of BIS. By increasing the amount of NIPAM and BIS to their limits of solubility in water the dose sensitivity of the gel is increased.

This particular gel formulation has been characterized in terms of post radiation temporal and spatial stability, intra and inter batch reproducibility, new calibration methods, and dose rate dependence [119]. Temperature dependencies have not been investigated for this specific formulation, but experiments have carefully controlled

for it and previous studies have shown radiation induced temperature increases in NIPAM gels do not affect their dose response [120]. The polymerization reaction was found to stabilize 15 hours after irradiation and the spatial stability began to degrade slightly if imaging was performed more than 36 hours after irradiation. For this reason, gel imaging is recommended between 15 and 36 hours post-irradiation. Batch reproducibility was shown to be excellent, and a significant dose rate dependence (up to 20% discrepancy between 100 MU/min and 600 MU/min) was discovered. However, this dose rate dependence was not found to significantly influence gel response for an intensity modulated radiation therapy (IMRT) delivery when the dose rate between test and calibration irradiations was consistent [119]. Other work with this gel formulation has looked at the removal of CT imaging artifacts and inherent structured noise within the gel when imaging [117], commissioning of a multi-slice CT scanner for gel imaging [121] and the optimization of dose calibration techniques [122].

In polymer gel dosimetry the parameters used in the CT imaging are specifically designed to account for the low contrast in these dosimeters. Factors that affect noise in x-ray CT imaging include phantom diameter, x-ray tube current, x-ray tube voltage, slice scan time, number of image averages, pixel dimension and slice thickness [105]. A larger phantom will attenuate more photons reducing the number that reach the detector and therefore also increase noise in the image. X-ray tube current controls the number of photons produced used to produce the CT image, therefore increasing the signal to noise ratio and low contrast resolution. The X-ray tube voltage controls the photon energy; more energetic photons will be less attenuated and have a higher chance of passing through the imaged object. There is a trade-off though, as increased photon energy will affect photon interaction probabilities and reduce the contrast between different materials. Longer scan time will use more photons to create each image increasing the signal to noise ratio. Larger pixels within the 2D image will have more photons passing through each pixel and will therefore decrease the amount of noise in the image. Finally, increasing the slice thickness will increase the number of photons that reach the detector as the active detector area increases; this increases the signal-to-noise ratio. The effect that each of these parameters has on the noise in polymer gel imaging can be found in Hilts et al [123].

CT scanning protocols for gel dosimetry must account for not only imaging noise, but imaging time, spatial resolution and CT dose delivered to the gel as well. A balance must be struck between decreasing noise, maintaining a reasonable spatial

resolution and keeping scan times low to reduce load on the x-ray tube. Increased load on the x-ray tube can cause overheating and delays in the CT scan. Radiation exposure of the gel can affect gel dosimetry as the deposition of dose during the readout scan will induce polymerization within the gel. The optimization of scanning protocols has been previously studied and is selected to produce low image noise while avoiding excessive tube load and CT dose that can result from using a high number of image averages [123, 124]. In more modern multi-slice CT scanners, where multiple slices can be imaged at one time, tube load is less of an issue in gel doismeter readout [121].

The main advantage of using x-ray CT to read out dose information is that x-ray CT scanners are widely available in practically every cancer clinic. Using an accessible imaging modality that is directly integrated into the clinical treatment could make a dosimeter's clinical implementation and utility more appealing. Uncertainties associated with setup and positioning for x-ray CT gel dosimetry would be comparable to those seen for a patient as the dosimetry system would use the exact same equipment and conventions used for patient imaging and irradiation. If x-ray CT polymer gel dosimetry were to become a standard for radiation dosimetry the implementation of the imaging side would be simpler than for MRI or optical CT. However, since the dose response of polymer gels produces such small changes to the CT data there are some limitations when using x-ray CT as a read out method. X-ray CT cannot be used to measure low doses or evaluate the accuracy of a single 2 Gy fraction. The noise at these low dose levels is just too great to resolve doses in this range. X-ray CT read out gels are then more suited to measuring the delivery of multiple fractions or high dose fractionation schemes such as SBRT.

2.3 Monte Carlo Dose Calculation

Monte Carlo simulation is a method of dose calculation that models individual particles by simulating the transportation and interactions of these particles as they travel though a patient or phantom. This is different from convolution superposition based TPS, described in section 1.1.3, where dose is modelled on a larger scale using small dose beamlets and individual particles are not tracked. In Monte Carlo, particle interactions are sampled from probability distributions based on the fundamental laws of physics to simulate particle interactions such as Compton scattering, pair production, photoelectric absorption, and bremsstrahlung [125]. In theory, Monte Carlo

dose calculations should be able to calculate the dose contributed by each induvidual particle that interacts in the medium and the only limiting factor in the accuracy of simulations is the uncertainty in simulating a finite number of particles using random numbers to sample the probability distributions of the interactions. However, a number of trade-offs must be made in these calculations as simulating every interaction by every particle with an acceptable level of uncertainty would take an unreasonable amount of computing power and time. For example, due to the large number of interactions an electron experiences as it slows down most Monte Carlo simulations combine multiple interactions into larger steps with a process known as the *condensed history technique* [125]. Many other methods have been developed to improve the efficiency of Monte Carlo simulations well maintaining an acceptable level of accuracy, known as *variance reduction techniques*, including particle splitting/recycling, Russian roulette, and forced interactions [126]. In general, these techniques attempt to increase the relative occurrence of certain events to reduce uncertainty and decrease computation time.

Monte Carlo dose calculations generally have two major components: simulation of the linear accelerator head and simulation of radiation transport in the patient or phantom. The model of the linear accelerator head usually models from the point right before the electron beam hits the target and through the various collimators and other internal components of the linear accelerator. Some of this calculation is invariant for a specific beam energy, such the simulation of particles before secondary collimation by the linac jaws, and some is plan-dependent, such as the collimation performed by the jaws and multi-leaf collimator. The output will be a characterization of the beam before it enters the patient or phantom. The most commonly used Monte Carlo code for linac head modelling is BEAMnrc [127]. Modelling of the dose deposition in the patient or phantom is done based off density information from CT scans, just like TPS dose calculations. The beam output from the linac head calculation is used as the starting point for the patient dose calculation. Dose from each particle is deposited in the patient as it travels and this is done over millions of particles to accumulate the total calculate dose of the delivery. There are several Monte Carlo codes used for dose calculation in a patient the most common being DOSXYZnrc [128] and VMC++ [129].

2.3.1 Deformable Dose Calculations

Deformable dose calculations are a form of dose calculation that attempt to deal with the issue of changing patient anatomy during or between treatment fractions. To accurately accumulate dose that was planned in a reference anatomy state to the dose that may have been delivered on one or more deformed states one must somehow transform the dose from these deformed anatomies back to the reference anatomy. This is usually done by using a displacement vector field derived from a deformable image registration (DIR) algorithm. The vector field determines locations in the deformed anatomy which correspond to points in the fixed reference image so that dose from the deformed image can be warped back to points on the reference image. There are several different types of DIR algorithms that can be used achieve this goal. These include commercially available algorithms such as VelocityAI (Varian Medical Systems, Palo Alto, CA), which is an intensity based DIR and uses a B-splines algorithm; MIM Software (Cleveland, OH), which has both intensity based DIR and a hybrid intensity and structure based DIR; and RayStation (RaySearch Laboratories, Stockholm, Sweden), which has a hybrid intensity and structure based DIR and a biomechanically based DIR [130]. Another DIR algorithm, MORFEUS, is biomechanically based and utilizes finite element modeling techniques [131]. For details on additional studies that report on the many available DIR algorithms the reader is referred to a recent review article on DIR [132] and the AAPM TG-132 report on the *Use of image registration and fusion algorithms and techniques in radiotherapy* [133]. VelocityAI was the DIR algorithm used in this work to deform gel images and facilitate deformable dose calculations.

The simplest way to warp this dose is by translating the dose under the assumption that the voxels do change size or shape and simply translate from one location in deformed anatomy to another in the reference anatomy. [28, 134]. However, this correspondence between reference and deformed voxels may not exist due to changes in volume or density of structures in the image set. A number of groups have developed methods to interpolate dose from surrounding voxels in the deformed anatomy when mapping back to the reference anatomy to account for these structure changes [29, 135, 136]. This generally involves splitting the voxels into smaller sub-volumes so that dose from surrounding voxels can be split and interpolated before mapping back to the reference anatomy. It has been shown, however, that dose interpolation methods will lead to errors, especially in regions of high dose gradient [137], and

these methods also ignore changes in density which must occur if there are changes to structure volumes.

Another method of warping dose developed by Heath et al., defDOSXYZ, is a modification of the DOSXYZnrc Monte Carlo code and rather than assume that voxels do not change in size or shape, or interpolate dose from surrounding voxels to account for volume change, this method warps the voxels themselves based on the displacement vector field [30]. This voxel warping method produces irregular dodecahedral voxels in the deformed anatomy for which the density can be adjusted based on the change in volume of the voxel. In this method energy deposition is exactly warped from the deformed state to the reference state and no interpolation is necessary as there is a one-to-one correspondence between the static reference voxels and the warped irregular voxels.

2.4 Current 3D Dosimeter Research and Clinical Applications

As polymer gel and 3D dosimeter research has advanced dosimeters and read out techniques have become more refined, fabrication has become less cumbersome and the use of these dosimeters in clinical applications has become more prevalent. It has been suggested that 3D gel dosimeters could serve an important role as and end-to-end dosimetry device which would serve as a quality assurance test of the entire radiation therapy treatment chain as opposed to the testing of the individual components [35]. At present this type of test is generally only performed by an outside agency and gel dosimeters could provide an in-house option for this type of quality assurance. Another area of clinical application for gel dosimeters is in the initial validation of new treatment techniques, an area where high resolution, tissue equivalent, 3D dose measurements can provide useful insight before clinical implementation [35]. For example, gel dosimeters have been used in the evaluation of complex modern radiation therapy treatments such as 3D conformal RT, IMRT, and VMAT and more recently for high dose, low fractionation treatments such as stereotactic radiosurgery (SRS), and GammaKnife [34]. Gels and other 3D chemical dosimeters have also been used in clinical areas such as brachytherapy [138, 139], in-vivo dosimetry [140], proton dosimetry [141–143] and diagnostic imaging dosimetry [144, 145]. Other more recent work has seen chemical and plastic 3D dosimeters have performed more advanced

and novel dosimetry measurements such as dosimetry in the presence of magnetic fields for MR-linacs [146–148], remote dosimetry [149], verification of stereotactic spinal radiation therapy [150], and dosimetry of synchrotron radiation therapy and microbeam radiation therapy [151–153].

The use of x-ray CT polymer gel dosimetry in clinical applications has been limited to this point with an early example of the measurement of an SRS delivery [154], some preliminary measurements of IMRT dose deliveries [119] and the characterization of small field photon beams [155].

2.4.1 Deformable Dosimeters

Another area where polymer gel and 3D dosimeters have found use in clinical application is in deformable dosimetry. To be confident in the ability of deformable dose accumulation algorithms to accurately predict how dose will be deposited in deforming tissue there is a need for independent dosimetric measurements that are 3D, tissue equivalent, integrating, and deformable. To this end several deformable dosimeter systems have been developed, using MRI [156] and optical-CT [72, 157, 158] readout, with initial studies focusing on the characterization of the dosimetric and mechanical properties of these dosimeters [71, 99, 100, 159]. More clinically applicable research has also been undertaken with the initial evaluations of DIR algorithms and deformable dose accumulation algorithms measured against deformable dosimeters [156, 158, 160, 161]. At this point there are no deformable dosimetry systems that use x-ray CT as an imaging modality, which would have the advantage of a more accessible readout method, available in all modern clinical radiation therapy departments.

Chapter 3

Materials and Methods

This chapter describes general materials and methods relating to the subsequent results chapters. Section 3.1 describes the manufacture procedure and containers of the gel dosimeters used in this work. Section 3.2 describes the phantoms and setup apparatus used to irradiate and image the gel dosimeters. Section 3.3 describes the equipment and procedures used to irradiate the gels. Section 3.4 describes the planning and calculation of dose distributions used for comparison and calibration of gel dosimeters. Section 3.5 describes the equipment and procedures used to image gel dosimeters on the CT scanner. Section 3.6 describes the image processing and calibration techniques used to produce gel measured dose. Finally, section 3.7 describes the techniques and criteria used to evaluate the dose measured by gel dosimeters. Details specific to individual studies are described in their respective results chapter.

3.1 Gel Fabrication

3.1.1 Non-deformable Gels

Non-deformable gel dosimeters consisted of, by weight, 75.5% deionized water, 5% gelatin (Sigma-Aldrich, Oakville, ON, Canada), 15% N-isopropylacrylamide (NIPAM, TCI America, Portland, OR, USA), 4.5% N,N-methylenebisacrylamide (BIS, Sigma-Aldrich) and 5 mM tetrakis hydroxymethyl phosphonium chloride (THPC, Sigma-Aldrich). These gels were fabricated using a procedure initially described by Chain et al [74]. First, the gelatin and water were mixed, while the temperature increased to 40.0 $\pm$ 0.5°C. After approximately 20 minutes, the gelatin dissolved and the temperature of the gelatin-water mixture was reduced to 34.0 $\pm$ 0.5°C. NIPAM was then

added and allowed to dissolve completely over 10-15 minutes which was followed by the addition of BIS which was mixed for 25 minutes until it dissolved. The mixture was then cooled to a temperature of 30.0 ± 0.5°C and THPC was added and stirred into the mixture for 1 min and 15 s. The gel mixture was poured into a 1 L, 10 cm diameter plastic jar (Modus Medical Devices, London, ON, Canada) that can be seen in figure 3.1 and a layer of polytetrafluoroethylene(PTFE) tape was wrapped around the lip of the jar before closing it in an attempt to provide a better seal and to limit oxygen contamination of the gel. The jar was then flipped four times at 30-second intervals in an attempt to create an even distribution of chemicals and mitigate any effects of gravity induced settling of active chemicals at the bottom of the container. A large water bath was used in the setting process to reduce temperature gradients and slow the cooling of the gel as recommended by Johnston et al [121]. The temperature of the water bath was set at 30.0 ± 0.1°C to match the temperature of the prepared gel and both the gel and water bath were placed in a refrigerator for 6 to 8 h to allow the gel to set before irradiation. Total fabrication time was approximately 1 h and 50 min for each gel. Blank gels used for background subtraction of CT images were fabricated using the same procedure but containing 94% deionized water, 5% gelatin, 0.5% NIPAM, and 0.5% BIS. Small amounts of these chemical were added to the blank gels to prevent the growth of mold.

3.1.2 Deformable Gels

For deformable, an identical recipe as for the non-deformable gels was used, but with 10 mM THPC to enhance oxygen scavenging because of the reduced oxygen barrier of the deformable container. Wax beads (ArtMinds, TX, USA), approximately 3 mm in diameter, were added to each gel during fabrication to allow for the tracking of deformation and positioning of the dosimeters. Wax beads were chosen as internal markers because their CT number is approximately -100 HU which makes them easy to detect and track on CT images of the water equivalent gel. An image of the beads embedded in a non-deformable gel can be seen in figure 3.2a and in figure 3.2b they are visible in the CT image of a deformable gel. The overall fabrication procedure was identical to the non-deformable gels' except that the mixture was allowed to cool down to 22.0 ± 0.5°C before the addition of THPC to make distribution of the wax beads throughout the gel possible. When gels were poured at a temperature of 30°C the beads would float to the top of the container very quickly, at 22°C the gel was still

Figure 3.1: An image of a 1 L non-deformable gel dosimeter that's been irradiated next to a 650 mL deformable gel dosimeter in a latex balloon vacuum sealed in low-density polyethylene.

fluid but starting to become more viscous, reducing the amount of bead drift after pouring. The gel was poured into a 24-inch (inflated size) latex balloon (Qualatex, KS, USA) which was then tied at the top. The balloon was then vacuum sealed in low-density polyethylene (Uline, WI, USA) as can be seen in figure 3.1 to create an additional oxygen barrier. For some gels a change in balloon type necessitated the addition of a layer of polyvinyl alcohol coating (HI-FLOAT, KY, USA) applied to the outside of the balloon before vacuum sealing, to provide an increased oxygen barrier [162, 163]. After filling and sealing the deformable gel, it was flipped and rotated at increasingly shorter intervals over a period of 25 minutes to allow the beads to distribute throughout the dosimeter. The gel was then stored upright, with the balloon stem at the top, in a refrigerator for 6 to 8 h to allow the gel to fully cool and set before irradiation. Unlike the non-deformable gels, the deformable gels were cooled without a warm water bath to accelerate the cooling process so the lower density beads would not float to the top of the gel as it set. Total fabrication time was approximately 3 h for each gel, the additional time compared to the non-deformable gel procedure largely arose from the extra time needed to reduce the temparture of

the gels to 22°C prior to the addition of wax beads and a longer agitation period after sealing.

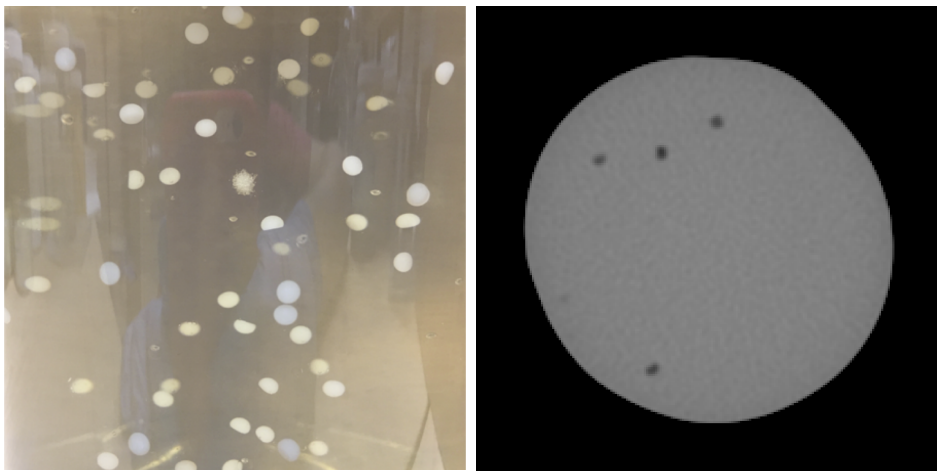

(a) (b)

Figure 3.2: (a) Wax beads embedded within a non-deformable gel in a 1 L jar and (b) wax beads visible in the CT image of a deformable gel.

3.2 Gel Positioning and Phantoms

3.2.1 Non-deformable Gels

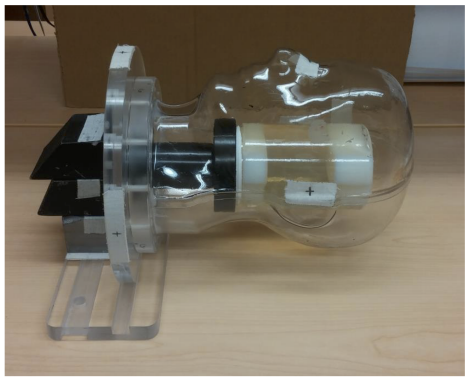

Figure 3.3: Anthropomorphic head and neck phantom used for gel irradiation and imaging with weights holding the phantom in place.

Non-deformable gels were positioned for both irradiation and CT imaging using an anthropomorphic head and neck phantom shown in figure 3.3. The custom-built

phantom, used in previous x-ray CT gel research [119, 122, 164], consists of an acrylic base and support arm designed to hold the 1 L gel jars with a press-fit and a 1 mm thick Perspex head that is attached to the base using plastic screws. Where the head connects to the base there is a rubber seal making it water tight when sealed so that the head can be filled with water when the gel is in place inside the head. The base connects to the CT or treatment unit couch using a locking bar to ensure reproducible and stable setup. Once the phantom is positioned and locked on the couch a set of weights can be placed on the base to further immobilize the gel and phantom. The head is marked with crosshairs on its sides and top so when it is connected to the base, the phantom can be setup on either the treatment unit or CT scanner via room lasers. The phantom, designed to undergo the entire radiation therapy process, has been shown to achieve sub-millimetre setup reproducibility and end-to-end tests have demonstrated localization of dose to within 1 mm using this phantom. It is also designed to allow removal of the head for CT scanning (described in section 3.5) while allowing only minimal impact (<0.5mm) on gel positioning [164].

3.2.2 Deformable Gels

Deformable gels were positioned using the base and support arm of the head and neck phantom, but without the attachable head. The gel filled balloons were setup inside a 1 L jar with the end removed and 1 cm diameter holes drilled in the side to allow setup marks to be made on the gel during setup for imaging or irradiation. The open ended jar was needed to allow for deformation of the gel in the superior-inferior direction, along the length of the jar as can be seen in figure 3.4. Deformation was achieved by means of an acrylic piston, 9 cm in diameter, which was attached to a BiSlide linear stage (Velmex Inc., Bloomfield, NY) and driven by a two phase stepper motor (Oriental Motor Co., Tokyo, Japan). Based on the manufacturers' specifications of the stepper motor and linear stage this system allowed for linear steps as small as 0.005 mm. As with the gel phantom base, the deformation apparatus can be locked into place using a CT locking bar to ensure a reproducible setup on both the CT and treatment unit couches. When deforming the gel for either imaging or irradiation the stepper motor was moved using a VXM controller (Velmex Inc.) connected to a laptop.

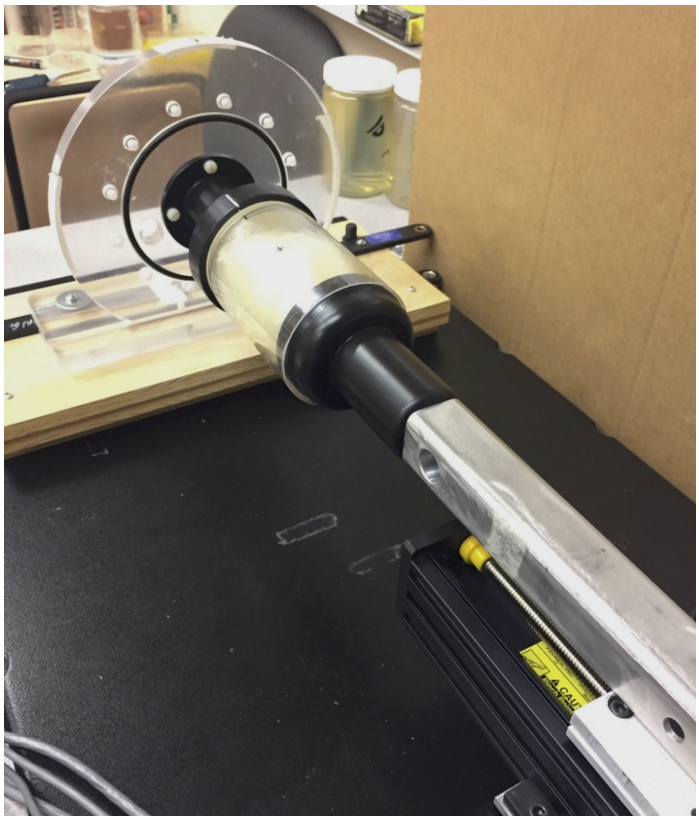

Figure 3.4: Deformable gel in open-ended 1 L jar with acrylic piston inserted for compression.

3.3 Gel Irradiation

All gels were irradiated using a Varian TrueBeam (Varian Medical Systems, Palo Alto, CA, USA) linear accelerator (or linac) at the BC Cancer Agency - Vancouver Island Centre (BCCA-VIC). All open field radiation deliveries to gel dosimeters used 6 MV photon beams at a dose rate of 400 MU/min. Gels that received radiation via a modulated treatment such as VMAT or IMRT had a dose rate that varied during delivery between 0 and 600 MU/min.

3.3.1 Non-deformable Gels

In the non-deformable dosimetry system, gels were irradiated with the head phantom filled with water and attached to the phantom base. Marks on the head were used to reproducibly setup the phantom via the linear accelerator room lasers. The temperature of the water in the head was measured before and after irradiation to ensure

a consistent temperature of the gel dosimeter when irradiated. After irradiation, all gels were returned to the refrigerated water bath and allowed to polymerize for 24 h prior to imaging.

3.3.2 Deformable Gels

In the deformable dosimetry system, the head was not used and gels were irradiated in the 1 L plastic jar shown in figure 3.4 surrounded by air. Crosshair marks made directly on the gel dosimeter were used for setup of the phantom on the linear accelerator. After irradiation the gel was returned to the fridge and again stored upright for 24 hours prior to imaging, with the balloon stem at the top and no water bath in a refrigerator.

3.4 Treatment Planning and Dose Calculation

3.4.1 Treatment Planning System

Radiation deliveries were planned using the ECLIPSE® treatment planning system (Varian Medical Systems, Palo Alto, CA). In general, for calibration of deformable and non-deformable dosimeters a simple 3-field calibration plan was delivered with small open fields at gantry angles of 45°, 270° and 315°. This plan was designed to cover a full range of doses up to approximately 27 Gy and to be used for dose calibration of x-ray CT gel dosimeters [119]. Specific details of the plans calculated and delivered to the gels will be described in the relevant results chapters.

3.4.2 Monte Carlo

To provide more accurate calculated dose for calibration, the Vancouver Island Monte Carlo (VIMC) system was also used to calculate the dose distributions. VIMC has been thoroughly validated for the calculation of complex dose deliveries [165]. BEAMnrc [127] was used to model the linear accelerator treatment head and either DOSXYZnrc [128] or VMC++ were used to calculate dose distributions within the gels. All Monte Carlo dose calculations used a dose grid size of $0.25 \times 0.25 \times 0.25$ cm^2 and calculated the dose to water with a statistical uncertainty of 0.5%. The dose distribution of a 3-field calibration plan on a non-deformable gel calculated by the TPS and Monte Carlo are shown in figure 3.5 .

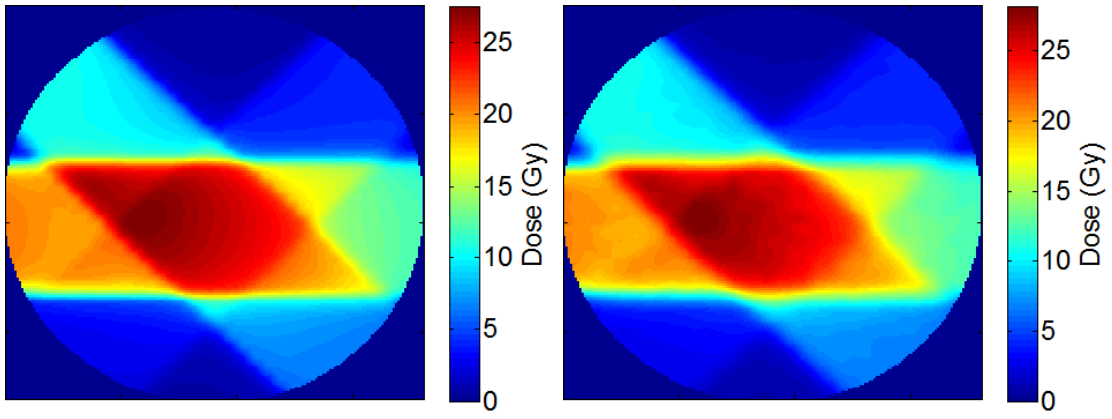

(a) (b)

Figure 3.5: Dose for a 3-field calibration plan calculated by (a) the TPS and (b) Monte Carlo.

3.4.3 Deformable Dose Calculation

Deformable dose calculations were performed by Dr. Emily Heath of the Carleton Laboratory for Radiotherapy Physics at Carleton University using a novel deformable dose calculation algorithm, defDOSXYZ [30]. The defDOSXYZ algorithm uses the same BEAMnrc algorithm to model the linear accelerator as VIMC and the differences in the systems lie in the calculation of dose within the patient or gel. As with VIMC dose calculations defDOSXYZ used a dose grid size of $0.2\times0.2\times0.25$ cm^2 and calculated the dose to water with a statistical uncertainty of 0.5%. Dose calculations using static beam deliveries from VIMC and defDOSXYZ were compared to ensure they produced similar dose calculations in the case where no deformation is present.

3.5 Gel Imaging

All gels were imaged using an Optima CT580 multi-slice CT scanner (GE Medical Systems, Milwaukee, WI, USA) at BCCA-VIC, which is a 3rd generation CT scanner as described in chapter 2. The multi-slice detector on this scanner is made up of 24 rows of individual detectors that can image up to 20 mm at a time in the axial direction. The central 10 mm of the detector is made up of 16 rows of detector elements 0.625 mm in width with 5 mm on either side made up of 4 rows, each 1.25 mm in width. The rows of detectors can be combined in a number of ways during each scan to control the slice thickness of each image and acquire multiple slices at

one time. In this work, for all gels imaged, 8 slices of 2.5 mm in thickness were acquired at each couch position in 20 mm steps over the length of the gel dosimeter. At each couch position, 25 images of the 8 slices were acquired for the purposes of image averaging. A summary of the CT parameters used for all image acquisitions can be found in table 3.1. These CT imaging settings are based on previous work to optimize gel dosimetry scanning protocols [121, 123]. Prior to each imaging session a short warm-up scan was performed, as recommended by Hilts et al [89], to minimize variations in x-ray tube temperature resulting from increasing tube load.

Table 3.1: Summary of CT settings used for gel image acquisition.

Setting	**Value**
Tube Current	200 mA
Tube Voltage	120 kV
Gantry Rotation Time	1 s
Slice Thickness	2.5 mm
Field of View	25×25 cm^2
Reconstruction Algorithm	Standard
Images Acquired per Slice	25

3.5.1 Non-deformable gels

Non-deformable gels were set up on the CT scanner bed using the head and neck phantom, as described in section 3.2, to ensure synchronized localization of the gel for imaging and irradiation. For imaging the head cast was removed, which has been shown to reduce imaging noise and artifacts without significantly affecting position reproducibility [164]. Prior to readout of an irradiated gel a background scan was taken of an unirradiated blank gel, whose fabrication was described in section 3.1, to be used for background subtraction.

3.5.2 Deformable gels

For the purpose of background subtraction each deformable gel was imaged prior to irradiation. This process differed from the non-deformable system and all prior work in CT gel dosimetry where background subtraction images are acquired using a blank gel. To perform an effective background subtraction the shape of the gel must be identical in the readout and background scan and it was possible to use a

blank gel for background scan when using identical 1 L jars as a container for all gels. With deformable gels, however, the variations in shape between each gel required that background and readout scan be performed on the same gel. For volumetric scanning using the scanning parameters in table 3.1 it is estimated, based on the results in Baxter et al. [124], that approximately 1 Gy of imaging dose was deposited prior to irradiation on the linear accelerator. After setting up the deformable gel for the background scan, a set of three crosshair marks were made directly on the gel to facilitate setup on the linear accelerator for irradiation and for the post-irradiation readout scan. Background scans of the deformable gels were taken immediately preceding irradiation.

3.6 Image Processing and Calibration

All analysis and image processing of gel dosimeters was performed using MATLAB® (version 2014b, The Mathworks, MA, USA). After imaging the data was processed to maximize the signal to noise ratio using previously established standard prodcedures for x-ray CT gel dosimetry [89, 117, 119]. The first step in image processing was to average the 25 images of each slice for both the background scan and the gel readout scan to decrease noise within the images. Background scan images were then subtracted from images of the irradiated gel to remove any artifacts caused by the container or from the CT scanner itself. The next step was to employ a 2D adaptive mean filter that is weighted by the ratio of local variance (σ_L^2) to overall image noise (σ_N^2). The value of pixels within the image after applying the filter are given by:

$$f(x,y) = g(x,y) - \frac{\sigma_L^2}{\sigma_N^2}[g(x,y) - m_L], \tag{3.1}$$

where $g(x,y)$ is the original pixel value and m_L is an estimate of the local mean around the pixel. This type of filter has been shown to be a highly effective tool for noise reduction while preserving edges in polymer gel dosimetry[116]. In this work a kernel size of 3x3 with 1 iteration was used for adaptive mean filtering as recommended by Jirasek et al. [117] when used in conjunction with the other filtering steps used in this work. The next step was to use a remnant artifact removal (RAR) technique introduced by Jirasek et al [117]. The RAR filter is designed to remove ring and streaking artifacts from the CT scan as well as noise intrinsic to the gel dosimeter caused by density fluctuations. The noise caused by inherent gel density

fluctuations is known to have some structure and is not purely random, which is why more standard noise reduction filters will not remove it [166, 167]. The RAR filter takes a 2D window and applies an n^{th} degree polynomial to fit the values over the defined span, which should be on the order of the size of the structured noise. Any value in this window that exceeds the polynomial fit is considered an unwanted structure or artifact and is redefined with the value from the polynomial. In this way the filter is stripping the signal from the data which, in this case, is the density fluctuations or CT artifacts. The filter is then rerun for a set number of iterations on the image. A number of different filter parameters were examined, but in this work the RAR filter was primarily set with a span = 7, degree = 3 and iterations = 2, unless otherwise indicated. In figure 3.6, a single slice of a gel irradiated with the 3-field calibration plan can be seen in the different stages of image processing described in this section.

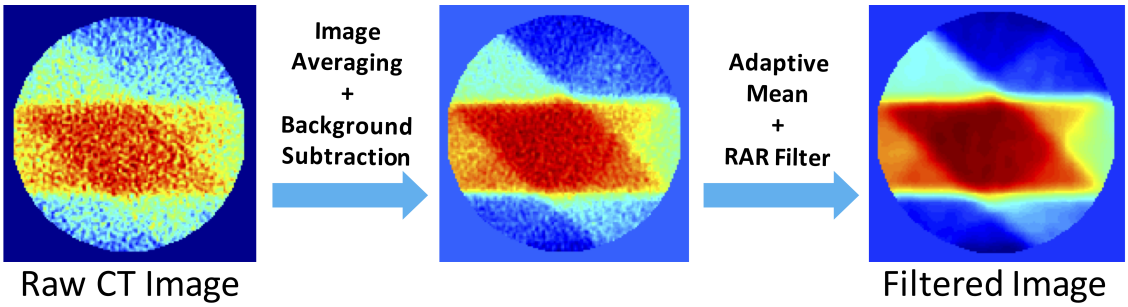

Figure 3.6: A single slice of an irradiated gel dosimeter as it undergoes the image proccesing steps described in this section.

Once the gel images were processed, calibration of the gel was necessary to establish a relationship between the change in CT number and dose for the gel dosimeters. The calibration method compares the dose from each pixel in the dose calculation to the CT number measured in the corresponding pixel in gel dosimeter image [119]. The calibration only compares points within the gel container and all other points are removed. This is done by creating a circular mask with a user-defined radius that is centred on the gel dosimeter; various radii for the mask were tested to optimize dose calibration. The CT images and calculated dose are registered using the shared DICOM coordinate system of the CT scanner and TPS; adjustments can be made to this registration to account for any setup error by visual comparison of the filtered gel image and calculated dose. Areas of high dose gradient are removed prior to calibration using a gradient threshold mask as any spatial errors in these regions

will cause large dosimetric errors in the calibration; an example of the calibration dose distribution with the high dose gradient regions removed can be seen in figure 3.7a. In this work a gradient threshold of 0.2 is used as recommended by Johnston et al [119]. Remaining pixels in the dose calculation data are then binned by dose and the average CT number for pixels within each dose bin are used to create data points for the calibration curve. Each pixel within the gel image has a CT number and associated uncertainty, errors are propagated through the mean calculation in the binning process [122]. A dose calibration curve is plotted based on the binned data points using an empirical model described by the following equation:

$$\Delta N_{CT} = \alpha + \beta \tanh(\gamma \mathrm{D} - \phi), \tag{3.2}$$

where ΔN_{CT} is the change in CT number, D is the dose and α, β, γ and ϕ are fit parameters. This type of function has been shown to provide better calibration compared to other tangential or sigmoidal functions [122]. An example of a calibration curve using a gradient threshold of 0.4 and dose bin size of 1 Gy is shown in figure 3.8. The generated calibration curve can then be used to perform a self-calibration on the gel used to create the curve or it can be used to calibrate a different gel dosimeter. More specific details of dose calibration of deformable and non-deformable gels will be given the respective results chapters.

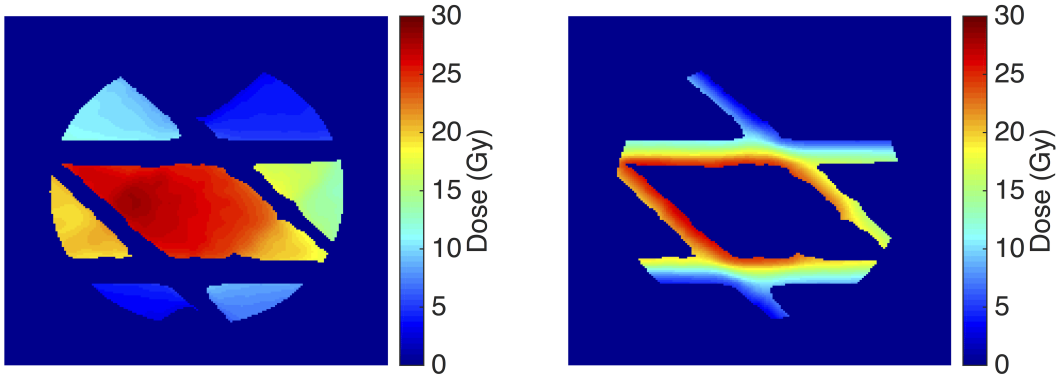

(a) (b)

Figure 3.7: (a) Low-dose gradient and (b) high-dose gradient regions of the 3-field calibration plan used for dose difference and DTA comparisons, respectively.

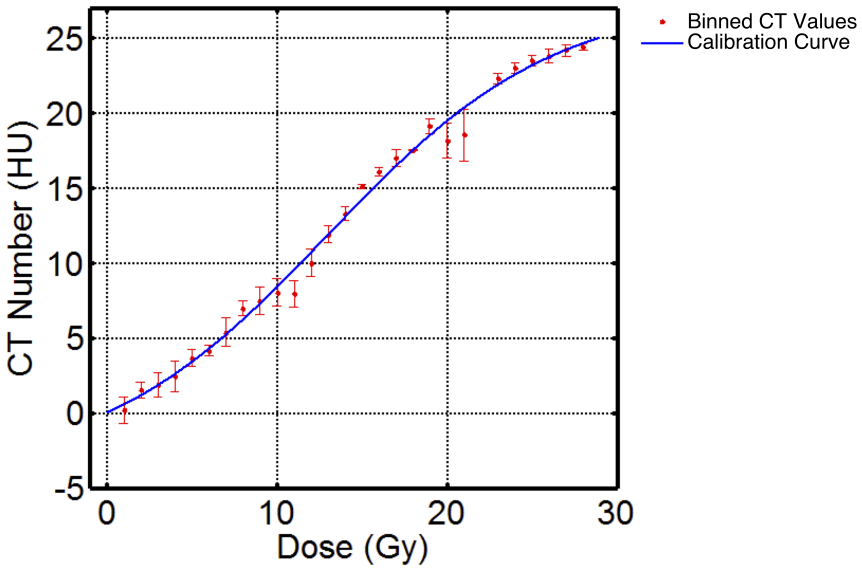

Figure 3.8: Example of a calibration curve used to convert CT number to dose.

3.7 Dose Evaluation Techniques

Once calibrated, measured gel dose distributions were compared to calculated dose in several ways. The first, and most natural, is a straight dose difference comparison. This is simply comparing the dose measured (D_M) at each point within the gel to the dose calculated (D_C) at the same spatial location. This can be represented as an absolute dose difference:

$$\text{Absolute Dose Difference} = D_M - D_C, \tag{3.3}$$

a dose difference relative to the calculated dose at the point of measurement:

$$\text{Local Relative Dose Difference} = \frac{D_M - D_C}{D_C}, \tag{3.4}$$

or a dose difference relative to the maximum dose within the calculated dose distribution (D_{max}):

$$\text{Global Relative Dose Difference} = \frac{D_M - D_C}{D_{max}}. \tag{3.5}$$

However, in regions of high-dose gradient small spatial errors or misalignments of either the calculated or measured dose can lead to large discrepancies in dose difference. For this reason, another metric known as distance-to-agreement (DTA)

was used to evaluate high-dose gradient regions of compared dose distributions. For each point within the dose distribution, DTA is the smallest distance between the measured data point and a data point in the calculated dose distribution that have the same dose. To evaluate the entire dose distribution at once a combination of these metrics known as the gamma-index, developed by Low et al [168], was also utilized. The gamma index calculation is dependent on setting dose difference and DTA criteria, ΔD_C and Δd_C, respectively. Given these two criteria the gamma index for the point $\mathbf{r}_m$ in the dose measurement is as follows:

$$\gamma(\mathbf{r}_m) = \min\{\Gamma(\mathbf{r}_m, \mathbf{r}_c)\}\forall\{\mathbf{r}_c\} \tag{3.6}$$

where,

$$\Gamma(\mathbf{r}_m, \mathbf{r}_c) = \sqrt{\frac{(\mathbf{r}_c - \mathbf{r}_m)^2}{\Delta d_C^2} + \frac{(D_c(\mathbf{r}_c) - D_m(\mathbf{r}_m))^2}{\Delta D_C^2}}, \tag{3.7}$$

$\mathbf{r}_c$ is a point in the dose calculation, $D_m(\mathbf{r}_m)$ is the dose at point $\mathbf{r}_m$, and $D_c(\mathbf{r}_c)$ is the dose at point $\mathbf{r}_c$. For a point to pass the gamma criteria it must have a gamma-index value of less than or equal to 1. The result of a dose distribution evaluated by the gamma test is often quoted as percentage of points passing the criteria. When calculating the gamma-index it is common for the dose difference, $D_c(\mathbf{r}_c) - D_m(\mathbf{r}_m)$, to be normalized to the maximum dose within the dose distribution (global normalization) and for points below a certain dose threshold, usually a percentage of the maximum dose, to be eliminated from the analysis. The dose difference and DTA criteria used in gamma analysis and the expected passing rates can vary based on the dose measurement tool being used and on the type of delivery being evaluated. The most common criteria used for treatment verification is 3%/3 mm with a global dose difference normalization [40]. These criteria are also suggested in the TG-119 report on IMRT commissioning [17], which also used a dose threshold of 10% of the maximum dose. TG-119 suggests acceptable pass rates of 90% for per field IMRT analysis and 88%-90% for composite irradiations analysed with film, with the caveat that gamma pass rates will strongly depend on the specific details of the procedure used. Basran et al. [169] has suggested that acceptable IMRT QA pass rates may be site dependant, with 95% suggested for non-head and neck IMRT plans and 88% for head and neck IMRT plans using a 3%/3mm gamma criterion and a 10% dose threshold. In March of 2018, the TG-218 report on *Tolerance limits and methodologies for IMRT measurement-based verification QA* recommended a gamma passing

rate tolerance limit of 95% and an action limit of 90% when using a 3%/2 mm criterion within a spatial domain defined above a 10% dose threshold [170]. Upon failure of these action level pass rates it is recommended that a medical physicist investigate the possible cause of this failure which could involve checking the setup of the dosimeter/phantom, the radiation beam, any QA software used, the MLC and the TPS. The ultimate solution may be as simple as a re-measurement of the delivery or lead to a complete re-planning of the delivery.

Chapter 4

Results and Discussion I: Evaluation of Accuracy and Precision in Polymer Gel Dosimetry

This chapter is reproduced from portions of an article entitled *Evaluation of accuracy and precision in polymer gel dosimetry* [1] published in the the journal of *Medical Physics* and is reproduced here with permission from John Wiley and Sons, Inc (Hoboken, NJ, USA). My contributions to this article included contributions to the conception and design of the experiments, collection of all data, production of all figures and tables, data analysis and interpretation, drafting of the article, critical revision of the article and final approval of the version to be published. Co-authors contributed to the conception and design of the experiments, data analysis and interpretation, critical revision of the article and final approval of the version to be published.

4.1 Introduction

Polymer gel dosimetry (PGD) is a branch of three-dimensional (3D) dosimetry where a carefully tuned recipe of radiosensitive chemicals dissolved in gelatin form a 3D dosimeter that will respond to delivered radiation in a predictable way. Once irradiated a gel is read out to acquire the dosimetric information and, traditionally,

polymer gels have been read out using magnetic resonance imaging (MRI). There has been a significant amount of research into the use of PGD with MRI readout [106–108, 171, 172], but the high cost and limited accessibility of MRI in a clinical setting have spurred research into other readout modalities such as optical CT [173, 174] and x-ray CT [89, 119, 155, 175] imaging. X-ray CT is a particularly interesting option as it is a well-developed and widespread imaging modality that is readily available in all modern clinical radiation therapy departments.

In x-ray CT PGD, changes in the linear attenuation coefficient within the irradiated gel are limited by the small size of the density changes (approximately 1 mg/cm^3 per 1 Gy of absorbed dose) [34] that occur due to the polymerization of the gel. X-ray CT PGD is therefore hampered by low signal-to-noise ratio and low contrast in its dose resolution. Research has focused on maximizing the signal by increasing the sensitivity of the gel recipe [74, 118], using filtering to decrease noise and remove artifacts [116, 117] and improving calibration techniques [122]. Recent research has moved toward preliminary clinical applications [119, 155].

PGD has natural advantages as a dosimetric tool as polymer gels are inherently 3D, tissue equivalent [176], and deformable. There has also been a significant amount of research into using less toxic, N-isopropyl-acrylamide (NIPAM)-based gel formulations to further increase clinical appeal [74, 96, 97, 177, 178]. Potential clinical applications of PGD include deformable dosimetry for verification of deformable dose calculations [158, 160], end-to-end validation of the clinical treatment chain, and the evaluation of other dosimetry systems used for clinical quality assurance. With the advancement of radiation therapy toward complicated clinical techniques in four-dimensional (4D) and image-guided adaptive radiation therapy, the need for a truly 3D dosimeter is essential and the promise of polymer gels in this regard is yet to be fully realized clinically [35]. To enable clinical implementation, the reproducibility, dosimetric accuracy, and spatial accuracy that can be expected of PGD systems need to be established.

The aim of this work is to assess the overall reproducibility and accuracy of an x-ray CT polymer gel dosimeter system initially characterized in a study by Johnston et al. [119] that investigated the temporal stability, spatial stability, dose rate dependence, and dose resolution of this system. This study also investigates the effect that calibration across different gel batches has on the accuracy of the system. Specifically, we investigate the use of interbatch gel calibration, average or generic calibration curves, and intragel calibration across different locations within the gel

dosimeter.

4.2 Materials and Methods

4.2.1 Fabrication

All active gel dosimeters and blank gels were fabricated as described in section 3.1.1 for non-deformable gels. In total, five 1 L gels were fabricated for analysis in this work with 4 gels manufactured from a single lot of NIPAM and 1 gel from a separate lot of NIPAM that was 2 years older. An irradiated gel fromt these experiment can be seen in figure 4.1a.

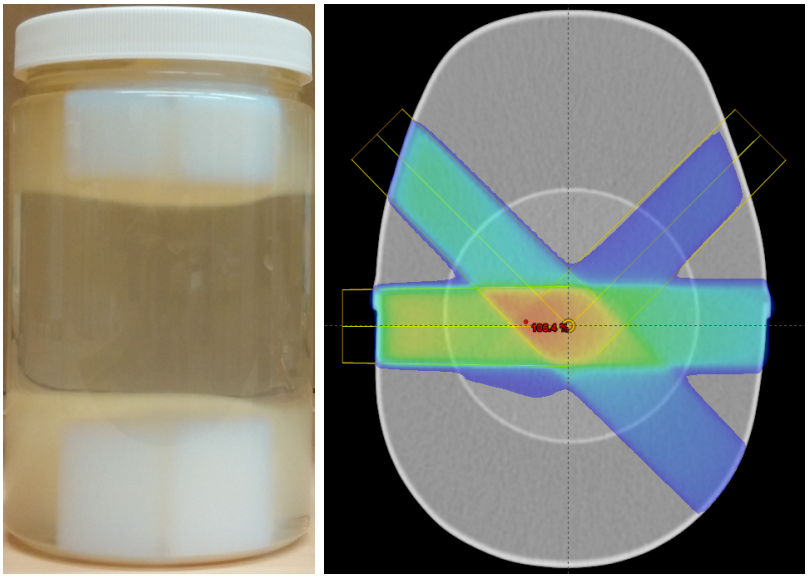

(a) (b)

Figure 4.1: (a) Irradiated 1 L gel dosimeter with calibration pattern delivered to both top and bottom of gel container and (b) treatment plan beam arrangement with color dose wash for calibration plan calculated in ECLIPSE®.

4.2.2 Treatment Planning and Irradiation

The 1 L gels were irradiated with three 3 × 7 cm^2 fields, at 45°, 270°, and 315° as shown in figure 4.1b. The plan was designed using the ECLIPSE® treatment planning system (Varian Medical Systems, Palo Alto, CA, USA) and covers a full range of doses up to a maximum of approximately 27 Gy. This treatment plan was

delivered to two separate locations within the gel at both the top and bottom of gel container and was used to calibrate the dose response of the gel dosimeter. The dose for this treatment plan was also calculated using the Vancouver Island Monte Carlo (VIMC) system which has been thoroughly validated for the calculation of complex dose deliveries as described by Bush et al [165]. The VIMC dose calculation was used for calibration of the gel dosimeter and as a comparison to assess the accuracy of the gel dosimeter.

During irradiation gels were setup using the anthropomorphic head and neck phantom introduced in section 3.2.1 and irradiated using the equipment and procedures described in section 3.3.1.

4.2.3 X-ray CT Imaging and Image Processing

After irradiation gels were imaged using the Optima CT580 multi-slice CT scanner described in section 3.5. The procedures and imaging parameters for all gel dosimeters and blank gels imaged in these experiments are given in detail in section 3.5.1 and Table 3.1.

After CT readout, image processing was performed using the procedures outlined in section 3.6. Briefly, these steps include image averaging, background subtraction using blank gel images, 2D adaptive mean filtering, and remnant artifact removal (RAR).

4.2.4 Dose Calibration

The general dose calibration steps used in these experiments are described in section 3.6 with calibration data fit using an empirical model defined in equation 3.2. In this study, we looked at different potential calibration methods for the gel dosimeter in an effort to determine any changes in accuracy when using different calibration techniques. The gels were calibrated in four different ways:

1. *Self-Calibration:* The gel image is calibrated using the calibration curve generated by its own image; it is essentially calibrated with itself. This eliminates any error introduced by differences between different gel batches and is a "best-case scenario" for the dosimeter.

2. *Intragel Calibration:* The gel image at the bottom of the container is calibrated using the calibration pattern at the top of the gel container. This removes

error produced by the differences between different gel batches but potentially introduces error produced by differences in the response of the gel at the top and bottom of the container.

3. *Average Calibration:* The gel image is calibrated using the average calibration curve of the four gels in the sample. The results from this type of calibration will determine the plausibility of using a generic calibration curve for this dosimetry system.

4. *Most Divergent Calibration:* The gel image is calibrated using the calibration curve which produces the least accurate dosimetric results. This is the "worst-case scenario" for this sample when attempting to use an intergel calibration.

The gel dose generated by each calibration method was compared to the VIMC calculated dose across the sample of four gels using (a) dose difference in low-dose gradient region (with a gradient threshold = 0.2), (b) distance-to-agreement (DTA) in high-dose gradient regions, and (c) gamma distributions and pass rates. An example of the high- and low-dose gradient regions for the calibration plan can be seen in figure 3.7.

4.3 Results

4.3.1 Gel Response and Reproducibility

Figure 4.2a is an example of the calibration curve for an individual gel dosimeter; this figure also includes all the binned CT values used in the fitting process. To demonstrate the interbatch reproducibility of the gel dosimeter, figure 4.2b illustrates an overlay of the calibration curves from each gel. Note that Gel 5 was the gel fabricated using a different lot of NIPAM, and this gel's calibration curve deviates significantly from the others; for this reason, it has been removed from the rest of the data in this work. Other gels made with this older lot of NIPAM showed a similarly decreased dose response when compared with the newer lot of NIPAM. The stark difference of the dose response for the gel made with a different chemical lot indicates the need for careful control and recording of chemicals used in the fabrication process, particularly for NIPAM. The consistency in the remaining calibration curves is an indication of reproducibility across different gel batches and allows for accurate

calibration of the gel dosimeter using an average calibration as described earlier. To further demonstrate consistency within calibration curves, Table 4.1 shows the calibration curve parameters as well as an average of these values which was used to perform the average calibration method.

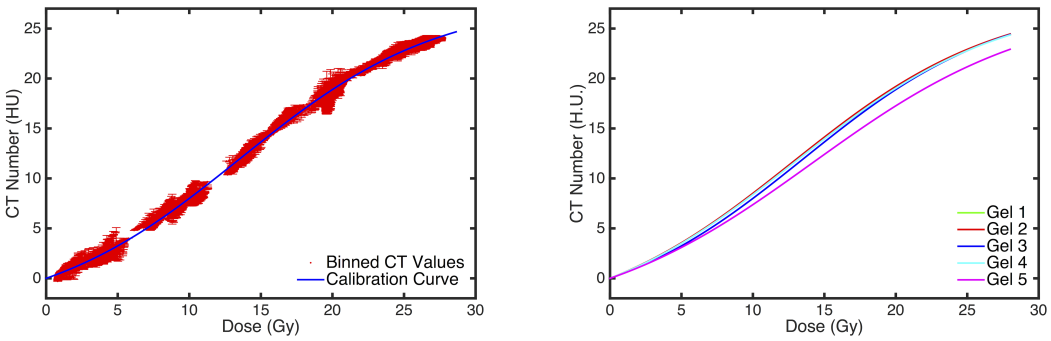

(a) (b)

Figure 4.2: Calibration curves for (a) an individual gel including all binned CT values used to produce the curve and (b) all five gels used in this work. Note Gel 5 in (b) was fabricated using a different lot of NIPAM.

Table 4.1: Summary of calibration curve parameters in reproducibility study.

	Fitting parameters (with 95% confidence bounds)			
	α	β	γ	ϕ
Gel 1	9.08 (9.03, 9.13)	16.6 (16.5, 16.8)	0.0674 (0.0666, 0.0682)	0.872 (0.859, 0.884)
Gel 2	8.74 (8.70, 8.79)	16.4 (16.2, 16.5)	0.0693 (0.0685, 0.0701)	0.885 (0.872, 0.897)
Gel 3	8.94 (8.90, 8.98)	16.0 (15.9, 16.1)	0.0717 (0.0710, 0.0725)	0.972 (0.960, 0.983)
Gel 4	8.76 (8.71, 8.80)	16.3 (16.2, 16.5)	0.0670 (0.0682, 0.0698)	0.893 (0.881, 0.905)
Average	8.88 ± 0.14 (1.6%)	16.3 ± 0.23 (1.4%)	0.0694 ± 0.0016 (2.2%)	0.905 ± 0.039 (4.3%)

4.3.2 Intragel Calibration and Correction

Figure 4.3a shows calibration curves created from the irradiation patterns delivered at the bottom and top of the gel container for Gel 1 and shows the difference in dose response at these two locations within the gel dosimeter. In figure 4.3b, the difference between the curves at the top and bottom of the gel container is plotted for the 4 gels included in this study along with an average of these differences. The curves appear to follow a similar overall shape and the differences between them span an overall range of less than 0.2 HU. As there is a consistent shape in these curves, the average curve is a representation of the average difference in gel response at the top and bottom of

the gel as a function of dose delivered. Using the average calibration curve difference between the top and bottom of the gels, a dose-dependent correction was calculated to be applied to calibration curves at the top of the gel container. Figures 4.3c and 4.3d shows the effect of this correction for an individual gels calibration curves and for the average calibration curves from all four gels. This correction is able to effectively account for the difference in the dose response of the gel and allowed for the possibility of accurate intragel calibration.

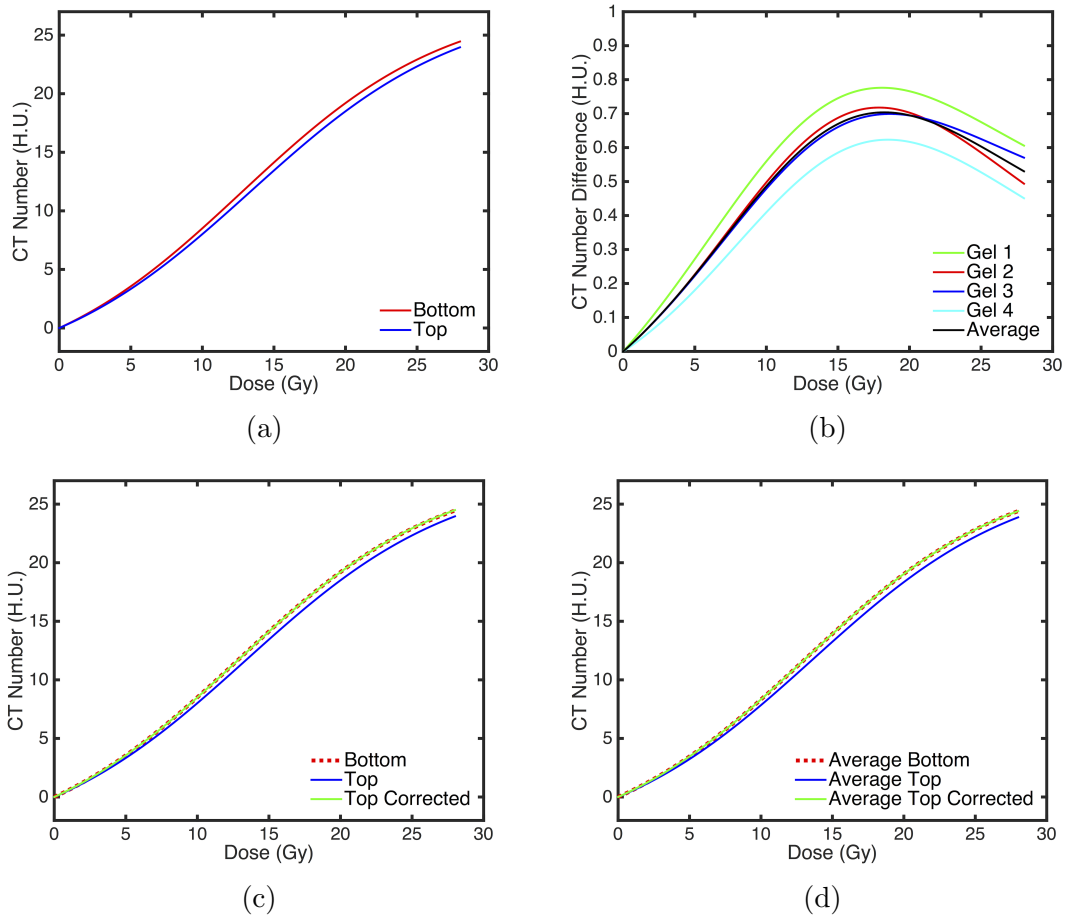

Figure 4.3: (a) Calibration curves at the bottom and top of an individual gel, (b) difference between the top and bottom calibration curve for each gel and an average of these differences which was used to create a dose-dependent correction, (c) calibration curves at the top and bottom of a gel with the corrected calibration curve overlaid, and (d) the average calibration curves from the top and bottom of all gels with the average corrected calibration curve overlaid.

4.3.3 Comparison of Calibration Methods

Dose Difference

Figure 4.4a displays the measured gel dose for a self-calibrated gel, and figure 4.4b displays Monte Carlo calculated dose for an individual gel dosimeter. The dose difference map between Monte Carlo and gel-measured dose is shown in figure 4.4c. Good agreement is seen in the low gradient regions outlined in figure 3.7a with the higher gradient regions outlined in figure 3.7b showing doses up to 2 Gy higher than calculated in Monte Carlo. There is also a region at the far left of the dose map near the entrance of the horizontal field where Monte Carlo calculates the dose to be around 20 Gy and the gel under responds by up to 2 Gy. This under response can also be seen in figure 4.5a at 20 Gy and in the binned data used for the calibration in figure 4.2a. Figures 4.5a and 4.5b show the effect that the amount of dose delivered has on dose difference. The gel dose is lower on average than calculated for the highest doses but is more accurate at other dose levels with an absolute mean dose difference of 0.46 Gy across all data points within the gel. In terms of variance within the local relative dose difference, figure 4.5b shows that this variance decreases as the delivered dose increases. This variance decreases because the absolute dose error is fairly constant across all dose levels, as seen in figure 4.5a, so as the amount of dose delivered to the gel increases, the variance in local relative dose error decreases.

A comparison of dose error produced using each of the described calibration methods is shown in figure 4.6. This figure shows the average dose error relative to the maximum delivered dose across all gel dosimeters used in this sample. The average calibration produces an average dose error of 1.8% which is similar to the best-case self-calibration with an average dose error of 1.6%. The similarity in dose error between these two calibrations methods indicates that the use of an average calibration curve can be effective. Even when using the most divergent calibration, the average dose error remains below 3%, and although the uncorrected intragel calibration method produces an average dose error of approximately 5%, the dose-dependent correction returns the accuracy to that of the average calibration method. In figure 4.7, the average dose error for the first three calibration methods is shown as a function of the dose delivered, and as seen previously in figure 4.5a, this dose error is relatively consistent across all dose levels. Figure 4.8 shows that although the intragel calibration error increases with the amount of dose delivered, the correction method is effective across all dose levels.

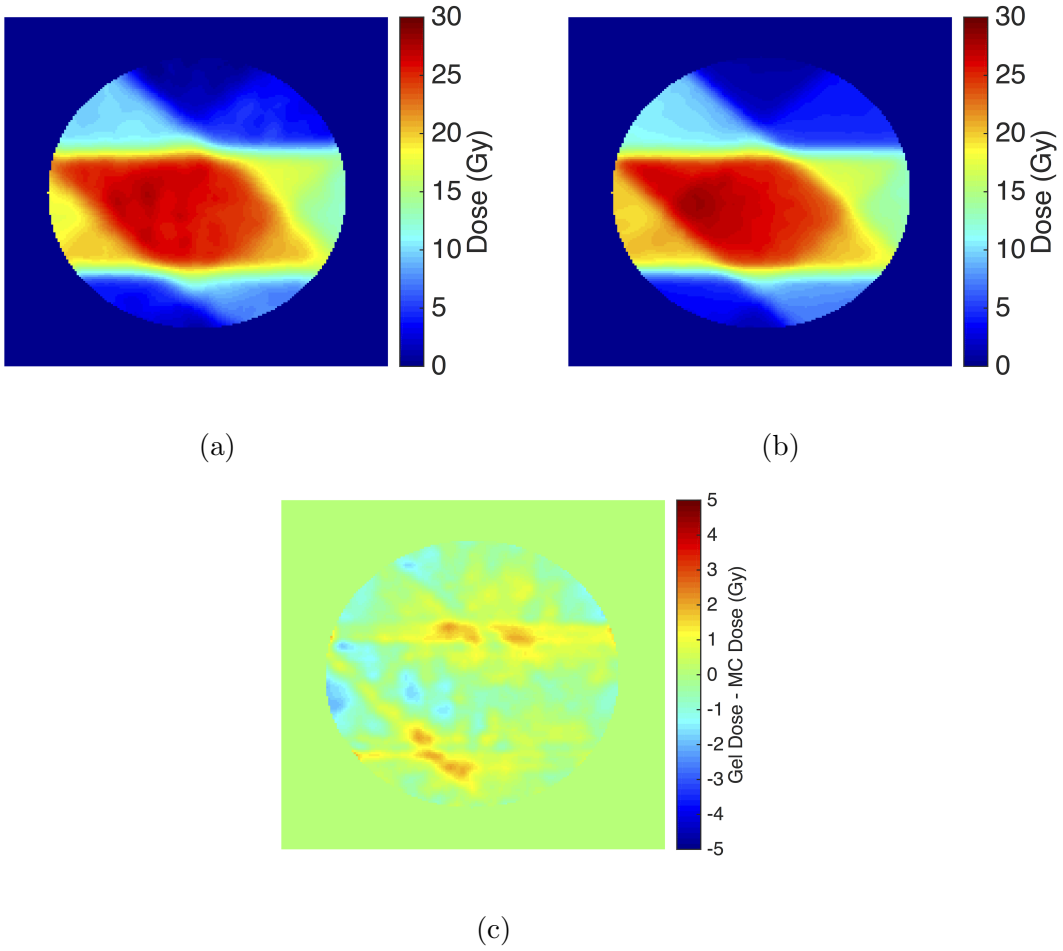

Figure 4.4: Dose maps for (a) measured gel dose, (b) Monte Carlo calculated dose, and (c) gel dose - MC dose for a self-calibrated gel dosimeter. The cross-sectional diameter of the gel is 10 cm.

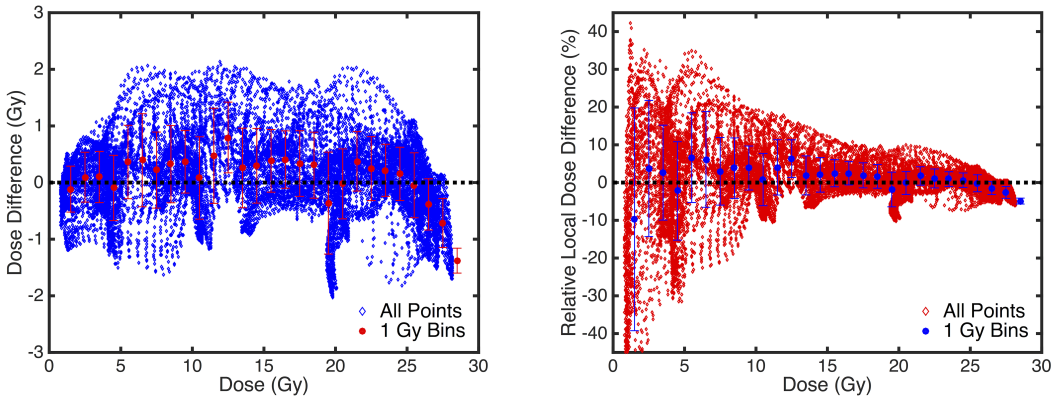

(a) (b)

Figure 4.5: Comparison of a single measured self-calibrated gel dose to Monte Carlo calculated dose using (a) dose difference in each voxel plotted as a function of dose delivered and (b) relative local dose difference as a function of dose delivered. Data points have also been binned into 1 Gy bins and overlaid onto these plots.

Distance-to-agreement

Figure 4.9a shows the distance-to-agreement (DTA) between measured gel dose and Monte Carlo calculated dose for the same gel dosimeter examined in section 4.3.3. In this gel, more than 90% of points in the high-dose gradient region have a DTA of less than 1 mm and more than 99% of points have a DTA of less than 2 mm. These DTA results indicate that there is good spatial accuracy in these high-dose gradient regions. Comparing the high-dose gradient regions in figure 4.9a to the dose difference map in figure 4.4c, these regions showed an absolute dose difference of up to 2 Gy. The low DTA values imply the cause of the high-dose error in the high-dose gradient region is due to small spatial inaccuracies. The cause of these spatial inaccuracies is unclear and previous work has shown that spatial integrity of this dosimetry system is excellent for gels imaged between 15 and 36 hours post-irradiation [119]. DTA analysis in the high-dose gradient regions complements dose difference values measured in the low gradient regions. Table 4.2 summarizes the data from this reproducibility study, and overall, the spatial accuracy is excellent for the self, average, and corrected intragel calibration methods with mean DTA values equal to approximately 0.6 mm and more than 99% points with a DTA less than 2 mm. The average calibration results again indicate good reproducibility within the sample set, and even when using the most divergent calibration within the sample, more than 97% of points in the high gradient region have a DTA of less than 2 mm.

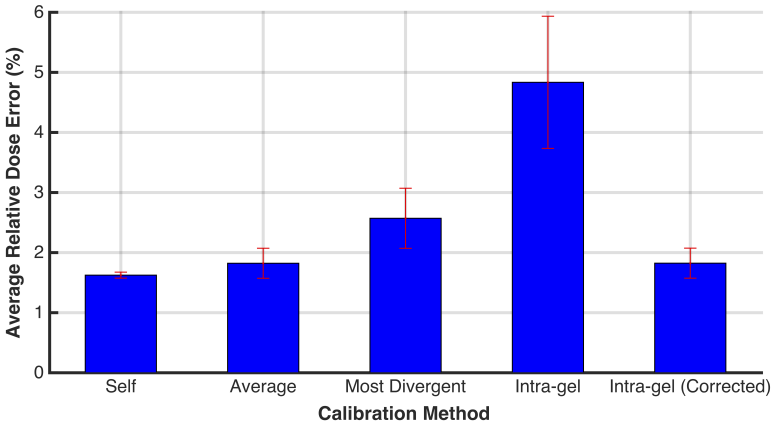

Figure 4.6: Average dose error relative to the maximum dose across all gels within the sample for each calibration method.

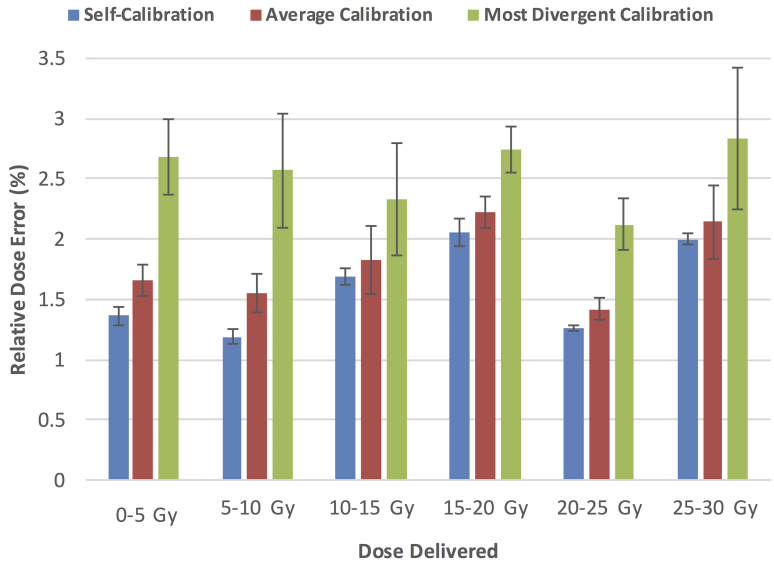

Figure 4.7: Average dose error relative to maximum dose across all gels within the sample binned into 5 Gy dose levels.

Gamma Analysis

Combining both the high and low gradient regions together and performing a full gamma analysis gives a sense of the dosimetric and spatial accuracy through the entire gel dosimeter. Figure 4.9b shows the gamma values for an individual gel dosimeter. In this example, fewer than 2% of points fail the gamma metric when using a 3%/3 mm criterion, with some points failing in areas that correspond to an under response of

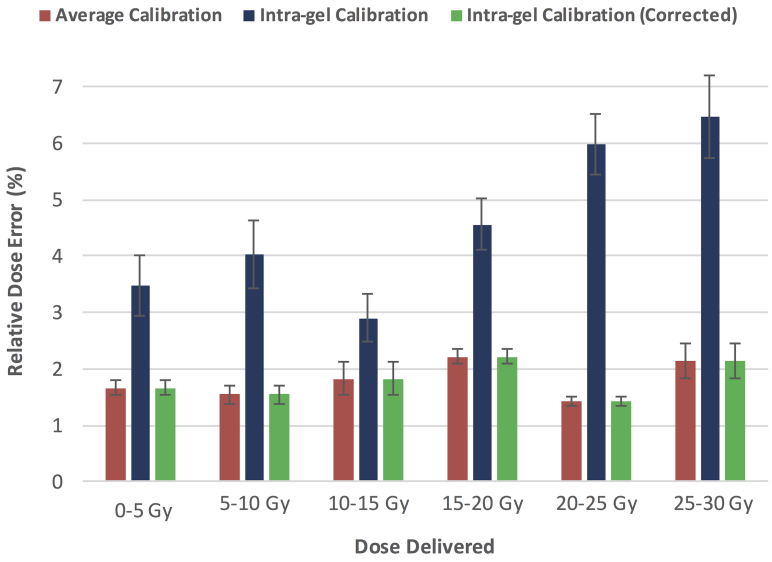

Figure 4.8: Average dose error relative to maximum dose across all gels within the sample binned into 5 Gy levels. A comparison of the average and intragel calibrations can be seen here; as well, the effectiveness of the dose-dependent correction factor used for intragel calibration.

Table 4.2: Summary of distance-to-agreement (DTA) results from high-dose gradient regions in reproducibility study.

Calibration method	Mean DTA (mm)	Mean pass rate DTA < 1 mm	Mean pass rate DTA < 2 mm
Self-calibration	0.61 ± 0.03	$92.2\% \pm 1.9\%$	$99.8\% \pm 0.2\%$
Average calibration	0.63 ± 0.07	$91.4\% \pm 2.4\%$	$99.6\% \pm 0.3\%$
Most divergent calibration	0.72 ± 0.17	$85.8\% \pm 6.3\%$	$97.2\% \pm 2.6\%$
Intragel calibration	1.34 ± 0.21	$52.1\% \pm 9.9\%$	$83.3\% \pm 5.9\%$
Intragel calibration (corrected)	0.63 ± 0.07	$91.4\% \pm 2.4\%$	$99.6\% \pm 0.3\%$

the gel dosimeter seen in figure 4.4c. One of these under responding regions is just to the left of the center of the gel dosimeter where the delivered dose is near a maximum [see figure 4.4b]. This discrepancy may be a result of the shape of the calibration curve. In the highest dose regions small changes in CT number can lead to large changes in calibrated dose because the calibration curve becomes flatter at higher doses. This effect may also be the cause of a systematic under response that can be seen in figure 4.5a for delivered doses greater than approximately 25 Gy. Another region of failing points corresponds to the region of gel under response on the left side of the dosimeter near the entrance of the horizontal field that can be seen in figure

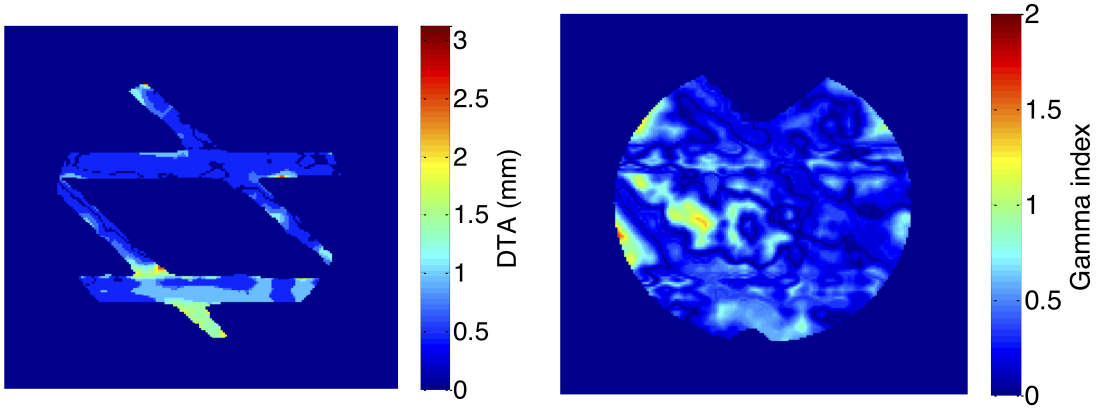

(a) (b)

Figure 4.9: Comparison of a single measured self-calibrated gel dose to Monte Carlo calculated dose using (a) a DTA map in the high-dose gradient regions and (b) gamma index through the whole gel with a 3%/3 mm criterion and 10% dose threshold. The cross-sectional diameter of the gel is 10 cm.

4.4c. The increase in dose error at the highest doses is a limitation of the ideal dose range of this dosimeter, which lies within the linear part of the calibration curve. For this reason, when using a gel dosimeter with this type of calibration, it may be best to limit the delivered dose to less than 25 Gy. In table 4.3, the average passing rates ($\gamma < 1$) at the 3%/3 mm criterion across the sample gels are greater than 95% for the average calibration and intragel calibration when corrected, although it should be noted that for Gel 3 the gamma pass rate drops below 95% for both of these calibration methods. Again we see the effectiveness of using an average calibration curve when compared to self-calibration and the effectiveness of the dose-dependent correction for intragel calibration.

Table 4.3: Summary of gamma analysis results in reproducibility study using 3%/3 mm gamma criterion with a 10% dose threshold.

	Gamma pass rates (3%/3mm)					
	Gel 1	Gel 2	Gel 3	Gel 4	Average pass rate	Mean gamma value
Self-calibration	98.4%	98.4%	98.2%	97.6%	98.2% ± 0.4%	0.320 ± 0.005
Average calibration	99.6%	99.1%	91.8%	96.6%	96.8% ± 3.6%	0.348 ± 0.040
Most divergent calibration	95.4%	96.6%	81.2%	90.3%	90.9% ± 7.0%	0.454 ± 0.074
Intragel calibration	64.0%	71.3%	91.1%	79.9%	76.6% ± 11.7%	0.706 ± 0.145
Intragel calibration (corrected)	99.6%	99.1%	91.8%	96.6%	96.8% ± 3.7%	0.348 ± 0.041

4.4 Discussion

4.4.1 Gel Response and Reproducibility

The difference in dose response between NIPAM lots was observed in other gels not shown in this work, and these results indicate that the use of NIPAM in this gel formulation must be carefully monitored. Using an average calibration or calibrating across different gel batches may not be effective without consistency in the chemical lot of NIPAM used or some form of correction to account for potential differing gel response. It should be noted that there was no issue with other ingredients in this formulation as gels made across different lots of Gelatin, BIS, or THPC, whose results are not shown in this work, showed no apparent difference in response. Overall, when NIPAM consistency is considered, the interbatch reproducibility is such that an average, or generic, calibration is possible and the potential of using a generic calibration curve is an important factor going forward for clinical applications of this gel dosimeter. Previous studies of NIPAM-based gel dosimeters have also looked at the reproducibility of gel dose response across a small sample of gel batches for both x-ray CT [89] and optical CT [171] readout. In neither case was an attempt to translate this toward generic calibration made.

4.4.2 Intragel Calibration and Correction

Gels manufactured in this work consistently showed a difference in response of up to 0.8 HU between the top and bottom of the gel container. The reason for this difference remains unclear despite attempts to resolve the discrepancy during the fabrication procedure. Gels were repeatedly flipped as they set to counteract any gravity induced settling of chemicals at the bottom of the gel container, but this was not effective in removing the discrepancy. Some gels were allowed to set in the fridge upside down, and although it was effective in reducing the difference in response between the top and bottom of the gel, cooling the gels in this manner also introduced a large amount of interbatch variability. The success of allowing the gel to set upside down does imply that the intragel variation is due in some part to gravitational effects on the cooling and setting of the gel. These initial attempts to resolve the issue are not conclusive about the exact cause of this intrabatch inconsistency and more work is needed. Given the consistency of the intragel variation, the most effective method to fix this issue was found to be a dose-dependent correction factor. This correction

factor effectively removed the difference in response at the top of the gel, however further work is needed to investigate the extent of this intragel variation and whether it can be corrected for the entire volume of the dosimeter.

4.4.3 Comparison of Calibration Methods and Accuracy of Gel Dosimeter

The four calibration methods investigated in this work provide valuable information in the future applications of this dosimeter. The self-calibration sets a baseline for the achievable accuracy of the system, stripping away error introduced by day-to-day variations in gel fabrication, irradiation, and imaging. Controlling for these factors was a priority in this work but variations in gel cooling, storage and handling, irradiation and imaging setup, and radiation delivery can contribute to interbatch variation [179]. Remarkably, the increase in the mean absolute dose error was less than 0.3% when comparing the average calibration and self-calibration. The mean DTA increased by less than 0.1 mm, DTA pass rates decreased by less than 1%, and average gamma pass rates decreased by less than 2% when moving from a self-calibration to an average calibration. Even when performing intergel calibration and choosing the single gel that produces the most divergent results as the calibration, the mean absolute dose error was less than 3% and the average gamma pass rate was greater than 90%. These results further demonstrate the excellent interbatch reproducibility achievable with this gel dosimetry system and demonstrate the effectiveness of the average calibration method. It is conceivable that with this level of consistency even a single gel could be used to calibrate multiple future dosimetry measurements, if all gels are made with the same lot of NIPAM. For 3D measurements using the entire volume of the gel however, one must consider the intragel variability displayed in this work as it will effect dose accuracy along the length of the dosimeter. A correction for this effect along the entire length of the dosimeter may be possible and could improve the accuracy of 3D dose measurements.

Overall when looking at the average calibration method, the mean dose error was 1.8% in the low-dose gradient region. Vandecasteele and De Deene [171] performed a study with a sample of eight acrylamide PAGAT gels using an MRI readout and with doses up to 12 Gy delivered. Mean dose discrepancies at isocenter when compared to an ion chamber measurement were found to be as high as 13.0% intrabatch and 13.7% interbatch. Note that these values are the maximum dose discrepancies and

that mean dose discrepancies as low as 2.7% intrabatch and 6.3% interbatch were found using different scanning timing and methods. The poor accuracy of these results was largely attributed to temperature fluctuations between the calibration and test phantoms. A further study by Vandecasteele and De Deene [107] repeated this experiment and reduced the mean dose discrepancy to 2.58% when temperature stabilization was held within 0.2°C. These improved results are comparable to those found in this work, and although the increased dose sensitivity of the MRI readout allows for dose measurements at a lower dose level, temperature sensitivity requires careful environmental control to avoid large dose errors. Chiu et al. [155] evaluated a NIPAM-based polymer gel with x-ray CT readout and when evaluating the percent depth dose (PDD) found discrepancies between gel measurement and EBT3 film than ranged from 0.17% to 4.94%. Overall, they found a 3.57% difference between the gel and film measurements when comparing PDDs.

When looking at the spatial accuracy of the average calibration method, the sample of gels in this work produced mean DTA of 0.63 mm in the high-dose gradient region and on average 99.6% of points in this region had a DTA less than 2 mm. Chiu et al. [155] also found a high degree of spatial accuracy in the high-dose gradient region with only a 0.5 mm difference between EBT3 film and the gel dosimeter when comparing the physical penumbras.

When evaluating all regions of the dosimeter with a gamma metric, the average passing rate in this work was found to be 96.8% using a 3%/3 mm criterion for gels calibrated using an average calibration curve. A large number of the failing points occurred in the region with the highest dose delivered to the gel, and the pass rates might be improved by limiting the maximum dose delivered to this gel dosimeter to less than 25 Gy. With renormalization, Vandecasteele and De Deene [171] found gamma pass rates using a 3%/3 mm criterion were as high as 97% and 99% for intrabatch and interbatch experiments, respectively. Chiu et al. [155] found pass rates greater than 96% using a 3%/3 mm criterion when comparing gel measurement to the TPS and EBT3 gafchromic film. Chang et al. [174] found gamma pass rates at the 3%/3 mm criterion were less than 90% with many points failing in the high-dose gradient region due to positioning errors, scattering, and edge enhancement effects. The scattering of light and edge enhancement effects in high gradient dose regions are known issues found in optical CT gel dosimetry [180, 181].

Other studies on the accuracy of gel dosimetry have focused on dose differences and gamma pass rates for clinical IMRT and VMAT plans. Oldham et al. [182] found that

a radiochromic 3D dosimeter made of solid polyurethane plastic and using optical CT readout had a gamma pass rate of 96% at the 3%/3 mm criterion for a complex IMRT delivery when compared to the TPS. Further study of this polyurethane dosimeter by Jackson et al. [183] found gamma pass rates of 99.6% for an IMRT plan and 94.5% for a VMAT plan.

The results in this work are on par with results in other gel studies, including those using optical CT and MRI as readout methods. When using the average calibration method, the results in this work are still comparable to those found with other gel dosimetry systems that use intragel or individual gel calibration. Given that the low-dose sensitivity of this dosimetry system requires the delivery of higher doses to achieve accurate dosimetry and the excellent spatial accuracy achieved in this work, this system may be best suited clinical applications that require highly accurate localization of large doses such as hypofractionated treatments or stereotactic radiosurgery (SRS).

4.4.4 Summary of Recommendations

1. The reproducibility between gel batches with this dosimetry system allows for the use of an average or generic calibration curve to calibrate individual dosimeters with a high level of dosimetric and spatial accuracy.

2. The use of NIPAM must be carefully monitored in the fabrication of this gel dosimeter. Differences in the age or chemical lot of the NIPAM used can affect the dose response and reproducibility of gel measurements.

3. At low doses, the absolute dose error is large relative to the dose delivered which leads to large relative uncertainty. At high doses, the gel becomes saturated and small changes in CT number can lead to large dose errors. It may be necessary to limit the dose delivered when using this gel formulation and calibration method to less than 25 Gy.

4. Intragel calibration is possible, however, due to gravitational induced differences in response at the top and bottom of the gel container, a correction factor is required to avoid large dose errors.

5. Overall, the results for this gel formulation and the average calibration method produce results comparable to other 3D gel dosimeters and readout techniques,

and this dosimeter has achieved sufficient accuracy and reproducibility to move forward toward clinical applications.

4.5 Conclusions

This work evaluates the reproducibility and accuracy of an x-ray CT PGD system as well as the feasibility of generic and interbatch calibration in PGD. Comparison of gel measurements with Monte Carlo dose calculations found excellent dosimetric accuracy when using an average (or generic) calibration (mean dose discrepancy of 1.8% in low-dose gradient region) and minimal accuracy was lost when compared to a "best-case scenario" self-calibration method (mean dose discrepancy of 1.6% in low-dose gradient region). An intragel calibration method was also investigated but required a dose-dependent correction to avoid large dose discrepancies. Spatial accuracy was also found to be excellent for the average calibration method (mean DTA of 0.63 mm and 99.6% of points with a DTA < 2 mm in high-dose gradient region) and again little accuracy was lost when compared to the self-calibration method (mean DTA of 0.61 mm and 99.8% of points with a DTA < 2 mm in high-dose gradient region). Gamma analysis using a 3%/3 mm criterion also found good agreement between the gel measurement and Monte Carlo dose calculation when using either the average calibration or self-calibration methods (96.8% and 98.2%, respectively). It should be noted that these results were limited to localized slices within the dosimeter and the intragel variability may need to be addressed to achieve this level of accuracy throughout the entire volume of the dosimeter

Overall, this work has demonstrated the effectiveness of interbatch calibration and the use of a generic calibration method with an x-ray CT PGD dosimetry system and we have achieved sufficient accuracy and reproducibility to begin investigating clinical applications.

Chapter 5

Results and Discussion II: Development of a Deformable Dosimetry System

This chapter is reproduced from portions an article entitled *Introduction of a deformable x-ray CT polymer gel dosimetry system* [184] published in the the journal of *Physics in Medicine and Biology* and is reproduced here with permission from IOP Publishing (Bristol, UK). My contributions to this article included contributions to the conception and design of the experiments, collection of all data, production of all figures and tables, data analysis and interpretation, drafting of the article, critical revision of the article and final approval of the version to be published. Co-authors contributed to the conception and design of the experiments, data analysis and interpretation, critical revision of the article and final approval of the version to be published.

5.1 Introduction

Technological advances in radiation therapy are pushing towards more complex treatment techniques that attempt to address issues that could not previously be considered. For example, four-dimensional and image-guided adaptive radiation therapy are used to correct for radiation dose delivered to patient anatomy that undergoes motion or deformation during treatment [19, 185]. To adapt treatment plans to deforming patient anatomy it is necessary to perform deformable image registration and

dose warping in order to assess the impact of the changing patient geometry on the delivered dose. To this end, a variety of different dose warping methods have been developed [28–30, 186–188]. To be confident in the ability of these algorithms to accurately predict how dose will be deposited in deforming tissue there is a need for independent dosimetric measurements that are three-dimensional, tissue equivalent, integrating, and deformable.

Several deformable dosimeter systems have been recently proposed, using a variety of manufacturing techniques and readout imaging modalities [72, 156–158]. Preliminary dosimetric and deformation characteristics of a polymer gel dosimeter that is read out using optical CT imaging have been determined [157, 159] and these gels were subsequently used in the initial validation of a range of dose-warping and deformable image registration algorithms [160, 161]. There has been preliminary work using an optically read out leuco dye based dosimeters that has primarily focused on initial dosimteric and mechanical characterizations [71, 72, 99, 100]. A methacrylic acid based gel dosimeter using magnetic resonance imaging (MRI) readout has been used to validate a deformable dose accumulation algorithm [156]. Finally, a deformable elastic polyurethane matrix doped with radiochromic leuco dye with an optical CT readout has been initially characterized and used in the verification of a commercial deformable image registration (DIR) algorithm [158]. These deformable dosimeters have shown promising results, however several issues remain outstanding. For example, MRI can be an inaccessible and expensive readout method and optical CT imaging is a developing imaging technology and requires a dedicated scanner that is outside the radiation therapy treatment workflow. To date there has been no attempt to develop a deformable dosimeter that uses x-ray CT imaging as a readout method. An x-ray CT read out deformable dosimetry system would have the advantage of an already established and widespread imaging modality that is readily available in radiation therapy departments and directly integrated within the radiation therapy workflow and, unlike optical CT, has no limitations on imaging geometry and can potentially scan dosimeters up to the size of a patient.

X-ray CT polymer gel dosimetry (PGD) measures the changes in linear attenuation coefficient caused by polymerization within a gel that has been irradiated. These changes are relatively small and therefore the development of x-ray CT PGD has been focused on maximizing this low signal by increasing dose sensitivity with improved gel recipes [74, 118], improving image filtering [116], removal of image artifacts [117], and optimizing calibration techniques [122]. More recent work has focused on potential

clinical implementations of an x-ray CT PGD system [1, 119, 155].

In this work, we introduce the first 3D deformable dosimetry system based on x-ray CT polymer gel dosimetry by building upon a previously established NIPAM based x-ray CT polymer gel dosimetry system [119]. We perform an initial characterization of this deformable dosimetry system and establish the setup reproducibility, deformation characteristics and dose response of the deformable dosimeter to determine the feasibility of future applications in the validation of dose warping and deformable image registration algorithms.

5.2 Materials and Methods

The fabrication of deformable gels is described in section 3.1.2 with figures of a deformable gel and wax fiducial markers shown in figures 3.1 and 3.2, respectively. For one gel, referred to as "Deformable Gel 3" for the remainder of this chapter, a thin layer of polyvinyl alcohol coating (approximately 1 mm thick) was applied to the outside of the balloon before vacuum sealing. The addition of this coating was needed to provide further oxygen barrier after a change in balloon type caused several consecutive deformable gels to show signs of significant oxygen contamination.

5.2.1 Dose Response Tests

Four deformable gels were irradiated to determine the dose response of the dosimeter. Three gels were irradiated with calibration plans to measure the dose response over a wide range of doses and one gel was irradiated uniformly to determine the spatial uniformity of the dose response.

Treatment Planning and Irradiation

The calibration irradiation plan, figure 5.1a, was designed using the ECLIPSE® treatment planning system (Varian Medical Systems, Palo Alto, CA, version 11.0.47) and consisted of three 3 x 6 cm^2 fields at gantry angles of 45°, 270° and 315°; this plan is based on previous work and designed to cover a full range of doses up to approximately 27 Gy [1, 119]. The third calibration gel, to be used for dosimetric analysis, was irradiated with an identical irradiation pattern, but with lower beam weighting so that the maximum dose was only 20 Gy. The lower dose plan was delivered to better visualize the dose response in the optimal dose range of the gel dosimeter.

The dose for these plans was also calculated using the Vancouver Island Monte Carlo (VIMC) system, which has been thoroughly validated for the calculation of complex dose deliveries, for comparison with measured gel dose [165]. In these calculations the Monte Carlo dose was calculated as the dose to water with a statistical uncertainty of 0.5%.

For the delivery of the calibration plans, the gels were setup in a 1 L plastic jar (Modus Medical Devices, London, ON, Canada) with the end removed and fit into an acrylic base that has been previously used and validated for the reproducible setup of gel dosimeters [164] and as can be seen in figure 5.2a.

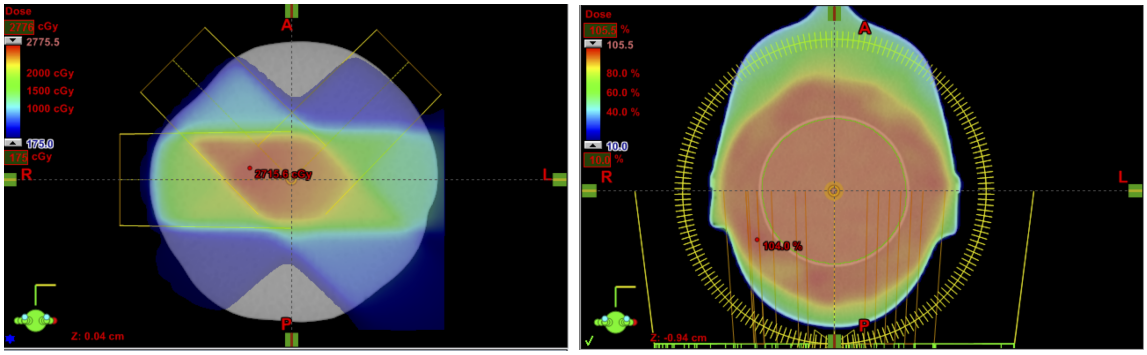

(a) (b)

Figure 5.1: The treatment plan beam arrangement for the (a) calibration plan and (b) uniform irradiation calculated in ECLIPSE® shown with a colour dose wash.

To test the spatial uniformity of the dose response another gel was irradiated using a volumetric modulated arc therapy (VMAT) plan optimized in ECLIPSE® to deliver a uniform dose throughout the gel dosimeter. This plan had less than 3% dose variation throughout the dosimeter from the mean dose of approximately 15 Gy and as shown in figure 5.1b. For the uniform irradiation the gel was placed inside an anthropomorphic head and neck phantom filled with water to provide buildup and facilitate the delivery of the uniform dose distribution.

X-ray CT Imaging, Image Processing and Calibration

For dose response tests, the deformable gels were read out using the Optima CT580 multi-slice CT scanner described in section 3.5. The procedures and imaging parameters for the read out and background scans of gels used in this work are outlined in section 3.5.2.

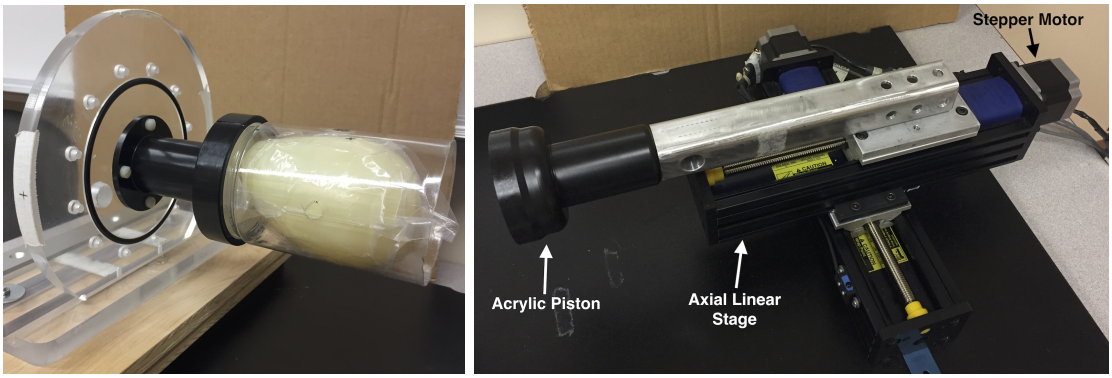

(a) (b)

Figure 5.2: (a) Deformable gel dosimeter setup in 1 L plastic jar for irradiation and CT imaging and (b) an acrylic piston attached to a linear stage which is driven by a two-phase stepper motor for deformation of the gel in the axial direction.

Image processing and dose calibration was performed in same manner as in Chapter 4 and as initally described in section 3.6. The measured gel doses shown in this work were calibrated using the self-calibration method used in Chapter 4, a technique which eliminates any error introduced by differences between different gel batches.

5.2.2 Deformation Tests

For setup positioning and deformation tests, the wax beads were used to track the position of the gel dosimeter and its deformed states. A volumetric CT scan of the gel was taken using the same scanning parameters as the dose response tests (without image averages). Bead positions were determined by setting a CT number threshold on the images and finding the centre of mass of the voxels that fell below the set threshold. All analysis of bead positions was performed using MATLAB® (version 2014b, The Mathworks, MA, USA).

Deformation Apparatus

Gels were setup as for the calibration irradiations (figure 5.2a). The gels were deformed in the superior-inferior direction using an acrylic piston driven by a stepper motor as outlined in section 3.2.2 and as can be seen in figure 5.2b.

Setup Tests

Due to the potential for a balloon confined gel to deform between irradiation and CT readout the reproducibility of gel positioning during setup was determined by analyzing the position of wax beads within a single gel over a series of 10 intra-day and 8 inter-day CT setups. Intra-day setups were all performed in one CT scanning session and in-between each image acquisition the gel was removed from the acrylic base and the base removed from the CT couch and both were re-setup for the subsequent measurement. The inter-day measurements were taken over a series of days with the entire setup apparatus and gel transported back and forth between the gel lab and the CT scanner. The inter-day measurements include uncertainty added from this transportation as well as uncertainty in laser and couch positions on a day-to-day basis. A set of control measurements was also taken where there was no movement of the gel or setup apparatus between scans and where the CT couch was shifted by a known amount between scans. The position of each bead within the gel was determined for every setup and the average shift of these beads determined the positional shift of the gel for each setup. A reproducible setup is crucial for the accurate comparison of dose read out in CT images to calculated dose and for effective artifact removal in background image subtraction.

Limits of Deformation

The limits of dosimeter deformation were tested by tracking the positions of wax beads throughout a single gel at various levels of deformation and tracking the positions of these beads once the gel had relaxed back to the undeformed state. The deformation tests determine how much the gel is able to relax for a given amount of deformation as well as give an indication of the average internal deformation within the gel for a given compression. Gel deformation measurements were performed for compressions between 15 mm and 30 mm.

Deformation Reproducibility

The reproducibility of the gel deformation was measured by comparing the positions of wax beads within a single gel in both relaxed and deformed states over 100 consecutive deformations. This was tested for compressions of 15 mm, 20 mm and 25 mm.

5.3 Results

5.3.1 Dose Response Tests

Dose Calibration

Figure 5.3a displays calibration data for two deformable gels irradiated with a calibration pattern as described in section 5.2.2; one with a maximum delivered dose of 27 Gy and one with a maximum delivered dose of 20 Gy. The dose response starts to decrease, becoming flatter for doses greater than 20 Gy and thus to maximize dose resolution a gel irradiated to a maximum dose of 20 Gy was used for dosimetric analysis. The fitted calibration curve as well as the binned CT values with measured uncertainty used in the curve fitting process are shown in figure 5.3a; an inset magnifies a portion of the curve to illustrate the uncertainty observed in the CT data. In figure 5.3b the fitted calibration curves are shown for all three deformable gels and compared to the average calibration curve for a non-deformable dosimetry system determined by Maynard et al. [1] using the same gel recipe. Note that the gels analyzed in the non-deformable study were fabricated using a different lot of NIPAM and changes in the lot of NIPAM can have significant effects on the overall dose response [1]. It is also possible that the increase in THPC concentration could have some effect on the dose response [94], although this is expected to be minor for the range of THPC concentrations used here. Overall there is consistency in the dose response between the three deformable gels, and when comparing the deformable gels to the non-deformable system. Most importantly there does not appear to be a significant drop in the dose response of the deformable system due to oxygen contamination; the oxygen barrier employed in this system appears to be as effective as that which is employed in the non-deformable system.

Figure 5.4 shows the dose difference and gamma analysis for a single slice within the 20 Gy gel dosimeter. Overall good dosimetric agreement is observed in the low-dose gradient regions of the gel with larger errors, up to 1.4 Gy, in some of the high-dose gradient regions near the edge of the calibration fields. These dosimetric errors in the high-dose gradient region, however, do not fail the gamma criterion. The mean relative dose difference for this gel was 1.5% and the gamma pass rate was 97.9% when using a 3%/3mm criterion with a dose difference calculated using global normalization and a 10% dose threshold. These results are an improvement to those seen for non-deformable gels when using self-calibration [1], likely due to using

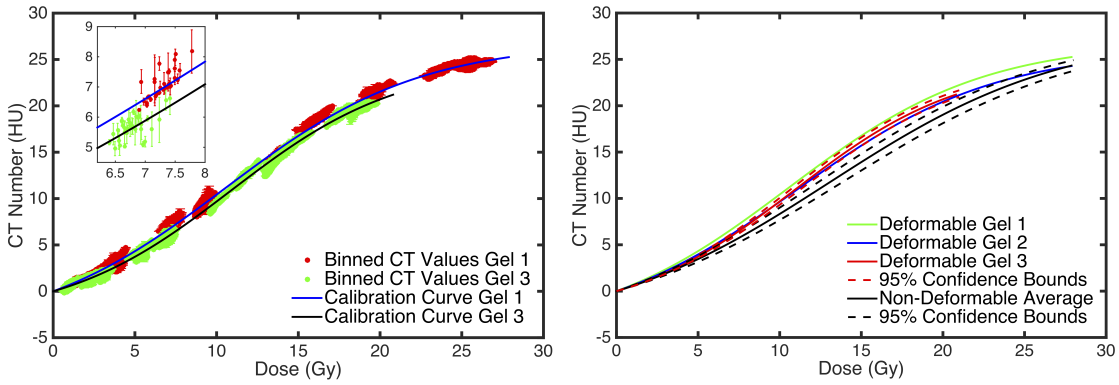

(a) (b)

Figure 5.3: (a) Dose response curves for two deformable gels with maximum delivered doses of 27 Gy and 20 Gy including all points used in the calibration and an inset figure showing an enlarged section of the plot with some data points removed to more clearly illustrate the uncertainty in the CT data, and (b) dose response curves of three deformable gels compared to the average dose response curve of non-deformable gels from a previous reproducibility study [1]. Confidence bounds based on the fitting parameters have been added to the curves for deformable gel 3 and the non-deformable average to give an example of the uncertainty on these fits.

a lower maximum dose of 20 Gy as recommended in that work.

Figure 5.5 shows the dose difference as a function of the dose delivered for every point within the self-calibrated dosimeter when compared to the Monte Carlo calculated dose. In figure 5.5a the standard deviation in the absolute dose difference error is consistently at approximately 0.5 Gy across all dose levels and again these results are comparable to those seen in the non-deformable dosimetry system.

Dose Uniformity

The results of the uniform irradiation of the gel dosimeter can be seen in figure 5.6, showing the uniformity of the dose response in a single slice in figures 5.6a and 5.6b and the dose uniformity in successive slices in the axial direction in figure 5.6c.

In the single slice of the dosimeter there is still some noise from the inherent structure of the gel [166, 167]. This type of noise is typically reduced by a remnant artifact removal filter [117], but persists to some degree in filtered gel images. Accounting for this inherent noise, there appears to be no overall spatial dependence of the dose response. There is, however, a decrease in CT number near the edge of the dosimeter over the entire circumference of the gel in figure 5.6a. The decrease in CT number

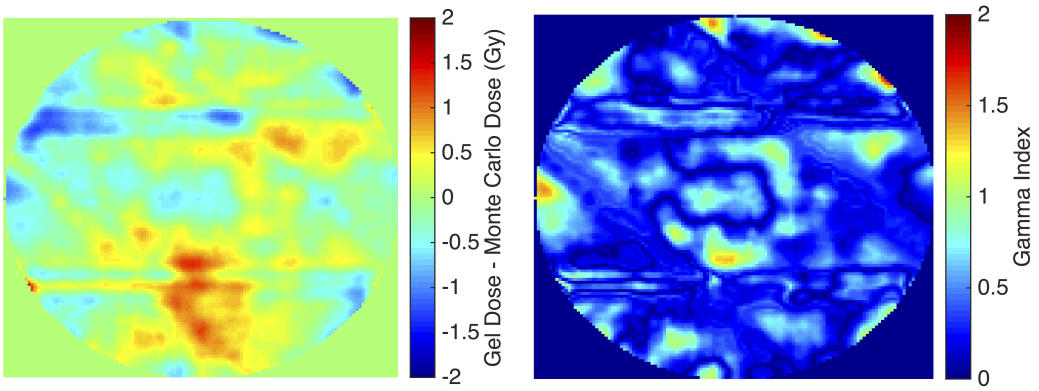

(a) (b)

Figure 5.4: (a) Dose difference map comparing deformable gel measured dose to Monte Carlo calculated dose and (b) Gamma index comparison using 3%/3mm criteria (global normalization) and 10% dose threshold.

can also be observed in the profiles in figure 5.6b and appears to have a magnitude of approximately 1 HU. It should be noted that the increase in CT number in the posterior region of the gel in figure 5.6a and in the vertical profile in figure 5.6b is due to a slight misalignment of the pre- and post-irradiation scans of this gel creating an artifact during background subtraction; it is not a characteristic of the uniformity of the dose response and is not present when the edges of the gel in the images are properly aligned. A drop in CT number near the edges of a gel has been seen in x-ray CT gel dosimetry in non-deformable systems and it has been suggested it may be related to temperature gradients during the cooling and storage of the dosimeter [1, 121, 172]. This drop in CT number could also be related to alignment of the gel between pre- and post-irradiation CT scans as any mismatch in these scans will lead to a change in CT number at the air-gel boundary related to the background subtraction of the gel images. It is also possible that this drop is related to oxygen contamination near the edge of the gel which would cause a decrease in dose response. Even if this edge effect remains uncorrected, this system has a spatially stable dose response in the axial plane within 0.5 HU over a diameter of approximately 65 mm.

Moving along the length of the dosimeter in the axial direction, figure 5.6c displays a spatially uniform dose response. There is a significant decrease in the gel response over the initial 10 mm of the dosimeter near the stem of the balloon where the diameter shrinks and edge effects begin to compromise the centre of the gel. Beyond this initial portion of the dosimeter, the average CT number of 75% of slices fall in a 0.5 HU

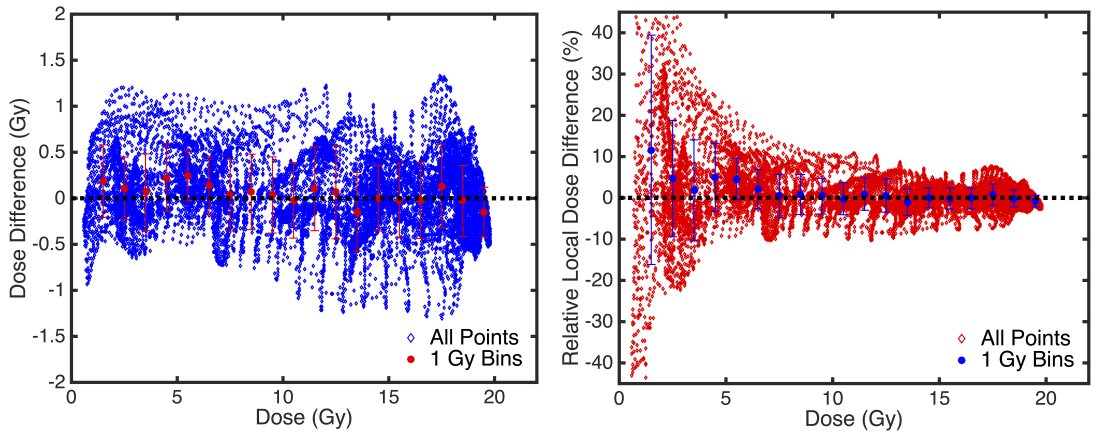

(a) (b)

Figure 5.5: Comparison of deformable measured gel dose to Monte Carlo calculated dose using (a) absolute dose difference in each voxel plotted as a function of dose delivered and (b) relative local dose difference as a function of dose delivered. Data points have also been binned into 1 Gy bins and overlaid onto these plots.

range and all slices are in a 0.8 HU range. There is an increase of approximately 0.4 HU in CT number moving along the length of the gel which is consistent with a vertical dose response effect seen with this type of gel dosimeter [1]. The vertical dose effect is relevant in this case as these deformable gels were allowed to set vertically, with the stem at the top. Overall there is an 80 mm range in the axial direction over which there is a spatial stability in the dose response for this deformable dosimeter.

5.3.2 Deformation Tests

In the following section the X,Y and Z directions are defined as the left-right, anterior-posterior and superior-inferior directions, respectively. Gels were compressed in the superior-inferior direction.

Setup Tests

The control measurements of the deformable gel and apparatus are shown in table 5.1. In the measurements where there is no gel movement between scans there is uncertainty in the wax bead position due to variation in which CT voxels fall below the CT number threshold that are used to determine bead positions. However this uncertainty is less than 0.05 mm in any direction and less than 0.1 mm overall. When a known couch shift was introduced between scans the bead measured movement was

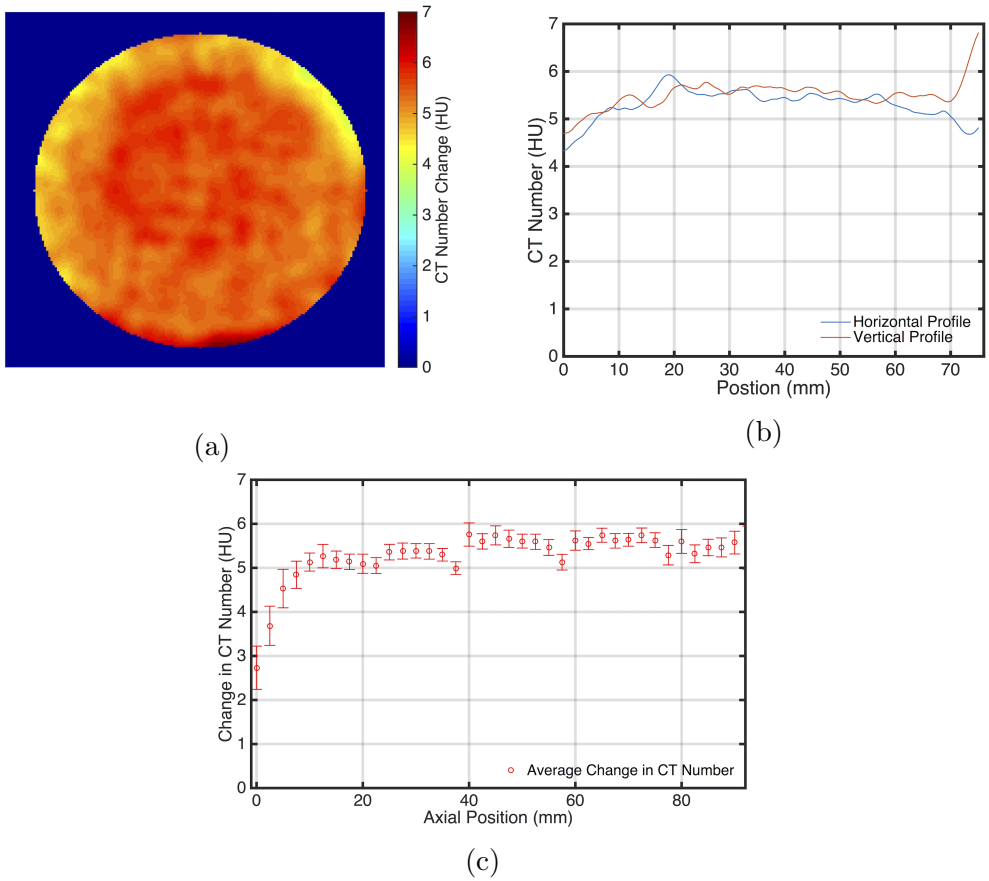

Figure 5.6: (a) A map of the change in CT number in a single slice of a deformable gel that has been uniformly irradiated with (b) horizontal and vertical profiles through this slice and (c) the average change in CT number in a region of interest at the centre of each slice of the gel with the stem of the balloon at 0 mm .

within 0.1 mm of the expected movement except in two instances, and in these cases the measured movements were within 0.15 mm of the expected result.

In table 5.2 the results of the intra-gel and inter-gel setup measurements are presented. For intra-day setups the results show that repeated set-up of this deformable gel dosimetry system within a single session is highly reproducible, with maximum uncertainty in gel position of <0.5 mm. When moving to an inter-day setup the positioning errors increase, however, even the least accurate setup of all 18 inter- and intra-day setups maintains sub-millimetre accuracy. Results also demonstrate there is no preferential direction for setup errors with this apparatus as the magnitude of the errors is similar in all directions. Figure 5.7 shows the positions of wax beads within the dosimeter for four representative inter-day setups. From these images it can be

seen that the differences in bead positions are not entirely based on identical shifts from every bead; some beads move more or less than others, indicating deformations of the gel or uncertainty in bead position. Note that these potential deformations were minor and there are no major deviations for any beads in these setups. Based on these results the set-up for CT imaging of this dosimetry system is highly reproducible, within 1 mm for all measurements, and despite a flexible container the dosimeter is stable over a large number of individual setups and imaging sessions.

Table 5.1: Average shift of wax beads within a deformable gel when the couch is shifted a known amount. A control measurement was also taken, measuring the average change in bead position with no movement of the gel between CT scans.

	X shift (mm)	Y shift (mm)	Z shift (mm)	3D shift (mm)
1 mm Y couch shift	0.00 ± 0.01	0.94 ± 0.03	0.02 ± 0.02	0.96 ± 0.03
2 mm Y couch shift	0.05 ± 0.02	1.86 ± 0.08	0.06 ± 0.10	1.97 ± 0.09
1 mm Z couch shift	0.04 ± 0.02	0.13 ± 0.05	0.92 ± 0.12	1.04 ± 0.11
2 mm Z couch shift	0.00 ± 0.02	0.10 ± 0.02	1.98 ± 0.08	2.00 ± 0.08
No gel movement	0.03 ± 0.01	0.03 ± 0.01	0.02 ± 0.01	0.09 ± 0.01

Table 5.2: Average and maximum shift of wax beads within a deformable gel over 10 intra-day and 8 inter-day setups on the CT couch.

	X shift (mm)	Y shift (mm)	Z shift (mm)	3D shift (mm)
Average intra-day setup error	0.12 ± 0.03	0.15 ± 0.03	0.08 ± 0.02	0.32 ± 0.04
Maximum intra-day setup error	0.24	0.21	0.17	0.48
Average inter-day setup error	0.25 ± 0.05	0.19 ± 0.04	0.23 ± 0.06	0.81 ± 0.04
Maximum inter-day setup error	0.46	0.28	0.54	0.99

Limits of Deformation

Figure 5.8a shows the effect of different levels of external compression by the piston in the axial direction on the wax bead positions within the gel. As expected, larger external compressions create larger bead shifts and the majority of bead motion is in

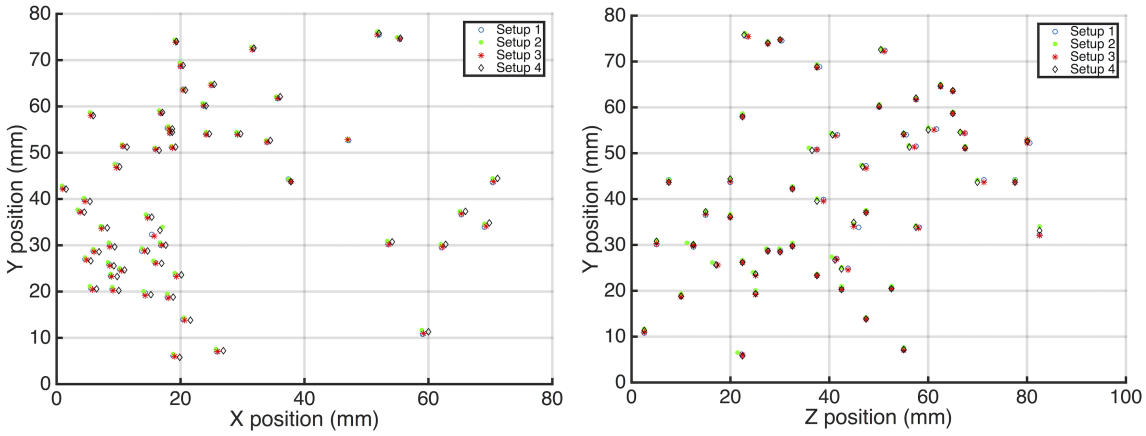

(a) (b)

Figure 5.7: (a) Scatter plot showing positions of wax beads within a deformable gel in the XY-plane for four different inter-day setups and (b) the same wax bead positions shown in the YZ-plane.

the direction of the piston movement. This primary bead shift in the Z-direction can be seen for a 15 mm external compression in figure 5.9b. There is also significant bead motion in the X and Y directions, the plane perpendicular to the piston compression, showing that there is deformation occurring as the gel expands outward when it is compressed. A visual representation of this effect can be observed in figure 5.9a. Overall there are significant deformations within the gel dosimeter when compressed by the piston, up to 13 mm, on average, in the direction of compression and up to 4 mm in plane perpendicular to compression.

Figure 5.8b shows the average bead displacement from the original gel state for the same compressions as in figure 5.8a after the piston is pulled back and the compression is removed. The beads return to, on average, within 0.4 mm of the original position for all levels of external deformation. Figures 5.9c and 5.9d show the positions of wax beads in their original position and after the gel has been released from a 15 mm external compression. For this compression, the majority of beads return to their original position with only a small number of beads showing significant deviation. In figure 5.8b there is a small, less than 0.2 mm, increase in the bead displacement as the external compression size increases from 15 mm to 30 mm. These results show that there is not a significant lasting effect on the deformable gel when compressed up to 30 mm externally and it is possible to achieve average internal deformations of up to 13 mm with the gel returning to its initial state afterwards.

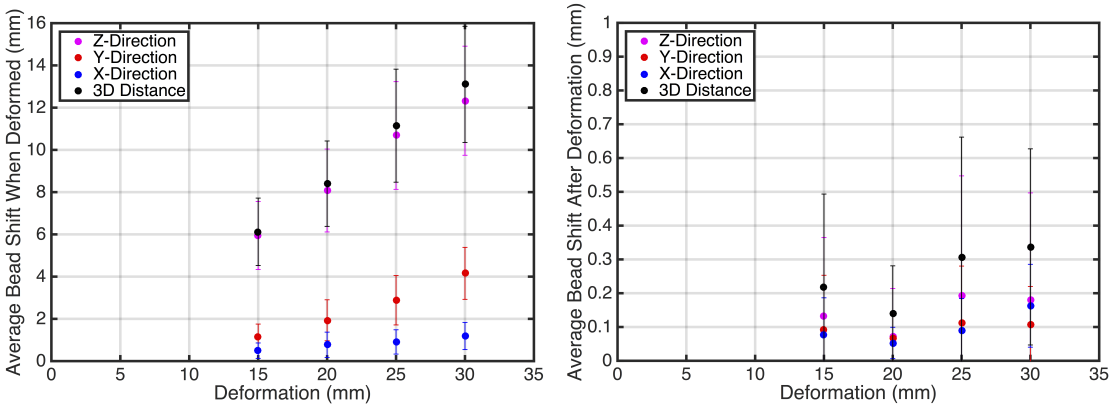

(a) (b)

Figure 5.8: (a) Average bead shift from setup position within the deformable dosimeter when it is externally compressed in the Z-direction and (b) the average bead shift from the original setup position after the compression is removed.

Deformation Reproducibility

In figure 5.10a the average shift in bead position from the original gel state is shown over 100 consecutive external compressions of 15 mm. The gel deformations are shown to be consistent as the positions of the beads in the deformed state are, on average, less than 0.3 mm apart when comparing the first and 100th gel compression. In figure 5.10b, however, the same cannot be said of the gel when it is released from compression. There is a clear and steady increase in the deviation of the bead positions as the number of deformations increases. It should be noted that these deviations are not driven primarily by motion in the direction of compression and that the majority of bead movement in this case is in the X and Y directions. This movement can be seen in figure 5.11, which shows the progression of the wax beads' positions in the relaxed gel states over 100 consecutive deformations. From these plots it is clear that the bead movement in the relaxed states is caused by an increasing rotation of the gel dosimeter rather than a permanent deformation of the gel from repeated deformations. There is some lasting effect in the Z direction caused by the repeated deformations but is limited to 0.5 mm over 100 compressions. Figures 5.10c and 5.10d show more reproducibility results for external compressions of 20 mm and 25 mm over 25 consecutive deformations. At these levels of external compression there are similar results to those seen with 15 mm of compression. Overall there was excellent reproducibility in gel deformations, with some permanent compression effects seen in the relaxed state of the gel and an issue with rotation of the gel as the

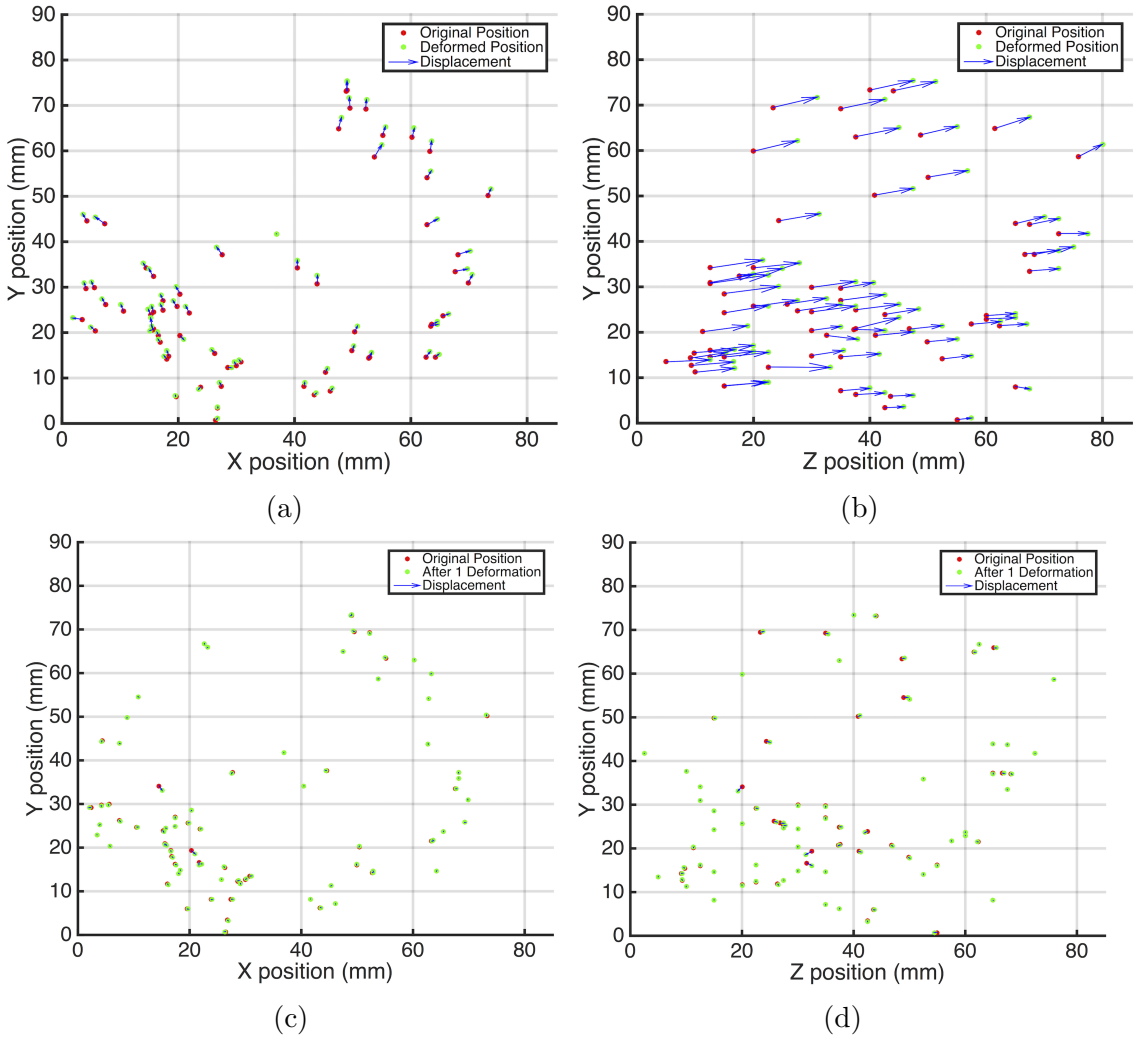

Figure 5.9: (a) Scatter plots showing the original and deformed positions of wax beads within a gel in the XY-plane when compressed externally by 15 mm, (b) the same wax beads positions shown in the YZ-plane, (c) the positions of wax beads within a gel in the XY-plane before and after a 15 mm external compression, and (d) the same wax beads positions shown in the YZ-plane.

number of deformations increased.

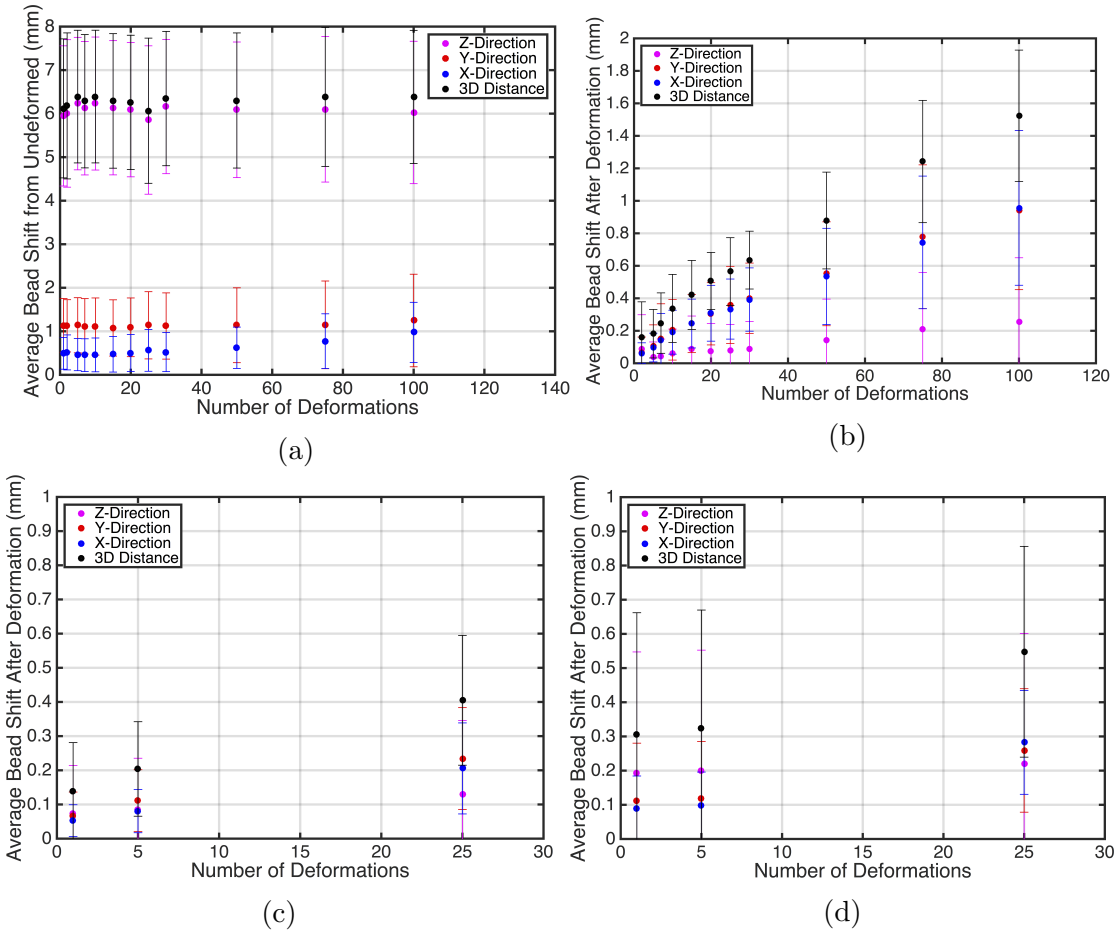

Figure 5.10: (a) Average bead shift from setup position within the deformable dosimeter when it is externally compressed 15 mm in the Z-direction over 100 consecutive deformations and the average bead shift from the original setup position after the gel is released for external compressions of (a) 15 mm, (b) 20 mm and (c) 25 mm.

5.4 Discussion

5.4.1 Dose Response

There are two major differences in the dose response between the deformable and non-deformable dosimetry systems. The first is the slope of the dose response curve in the linear region between 5 and 20 Gy, which is steeper for the deformable gels, and the second is that the dose response starts to flatten out earlier for the deformable

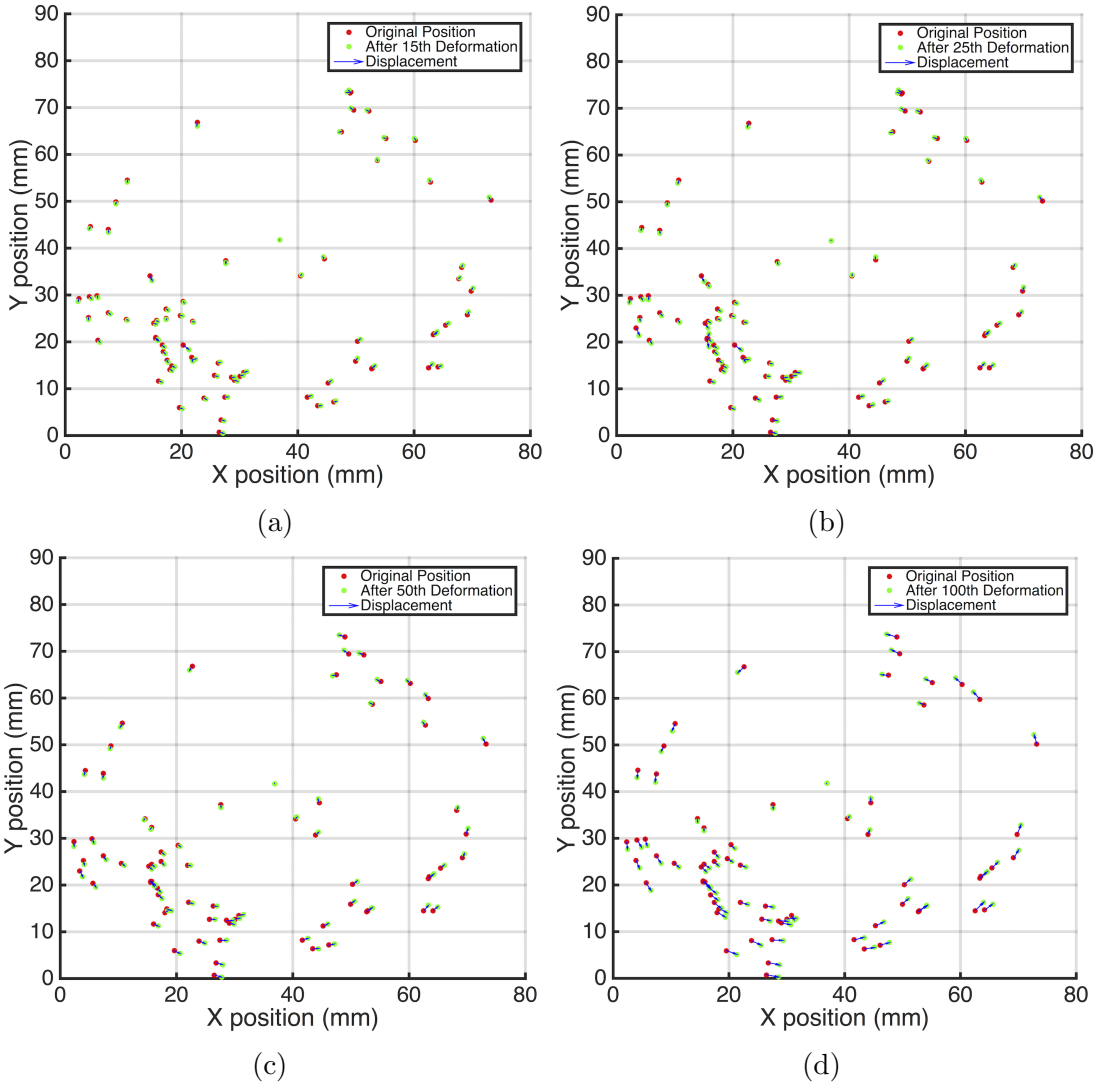

Figure 5.11: Scatter plots comparing the positions of wax beads within a deformable gel in the XY-plane before and after (a) 15, (b) 25, (c) 50, and (d) 100 external compressions of 15 mm.

system, especially for doses above 25 Gy. This flattening of the dose response at higher doses limits the optimal dose range of the dosimeter, at higher doses small changes in CT number can lead to large changes in the calibrated dose. The dose response at higher doses was also an issue in the non-deformable system, with the flatter dose response of the deformable dosimeter this issue is more pronounced for this system and is why a gel irradiated to a maximum dose of 20 Gy was used for dose analysis in this work.

The differences between these two systems has several potential causes, with the most likely being a different lot of NIPAM used. Changing chemical lots of NIPAM specifically has been shown to have significant impacts on the dose response of x-ray CT gel dosimetry [1]. Another potential factor is the increase in the concentration of THPC used for the non-deformable system; although this has been shown to decrease the slope of dose response curves, it should not be significant over the range of THPC concentrations used here [94]. Finally, the dose delivered to the gels, approximately 1 Gy, in pre-irradiation scans that are now required for background subtraction could contribute to the flattened dose response at higher doses for the deformable system. Overall for the best results, careful control of NIPAM used in calibration is critical and it is likely necessary to deliver no more than 20 Gy to this dosimeter to remain in its optimal dosimetric range.

The spatial uniformity of the dose response was limited by issues for points within 20 mm of the edge of the deformable dosimeter. Johnston et al. [121] found a difference of between 2 HU and 7 HU between the centre and edge of an active but unirradiated non-deformable gel in a jar 10 cm in diameter; these issues similarly affected the outer 20 to 25 mm of the dosimeter. This effect decreased for slices near the bottom of the gel container. In this work the decrease near the edges was found to be only 1 HU, however, the deformable gels are smaller in volume and diameter, and have a different cooling history than the gels produced in the non-deformable system. For this system, removal of the outer 20 mm of the gel from calibration and dosimetric evaluation limits the usable volume of the dosimeter but is effective in eliminating calibration errors. Due to this limitation it would be impossible to perform surface dosimetry or dosimetry on volumes with a diameter larger than 65 mm without the use of a larger container. Further study is required to eliminate or attempt to further mitigate this limitation of the dosimetry system so that full dosimetric use of the gel volume is possible.

5.4.2 Setup Reproducibility

The positions of wax beads within the gel dosimeter showed good agreement with their predicted positions when shifted a known amount on the couch. Also, when there was no movement of the gel the average perceived movement of the beads based on CT scans was less than 0.1 mm. Given potential uncertainty in the couch position, uncertainty introduced by the CT scan, and uncertainty in tracking bead positions, these results show the positions of beads within the gel can be accurately tracked in CT scans and the beads can be used to determine shifts and deformations of the gel dosimeter.

The setup errors determined for this deformable dosimetry system are comparable to those found when tracking fiducial markers within other deformable dosimetry systems. For example, Franich et al. [159] found mean setup errors of 0.53 mm, 0.44 mm and 0.15 mm in the AP, LR and SI directions with the optically read out DEFGEL system compared to 0.19 mm, 0.25 mm, and 0.23 mm, respectively, for this system. Yeo et al. [157] found a mean 3D setup error of 0.23 mm with a maximum setup error of 0.99 mm compared to 0.81 mm and 0.99 mm, respectively, in this work.

5.4.3 Deformation Limits and Reproducibility

For a single external compression of the gel up to 30 mm, no large permanent deformations to the gel dosimeter occured as the mean bead position shift was less than 0.2 mm from its original position in all directions. This deviation would not be detectable in a dosimetry measurement based on CT voxel size and setup limitations of the system. The limitation in this case was in the strength of the apparatus setup and compressibility limit of the gel as the whole system began to flex and bend when compressions beyond 30 mm were attempted. This 30 mm compression limit puts the deformations of this system within the range of intrafraction and interfraction motion of many organs [19].

In terms of deformation reproducibility, in the direction of compression the marker deviation from original position was less than 0.3 mm for up to 30 consecutive compressions and less than 0.5 mm for up to 100 consecutive compressions. The overall size of the external compression did not appear to affect these results. In directions perpendicular to compression the marker shifts were larger, but this was attributed to a rotation of the gel under compression rather than permanent deformations caused by the compressions. Franich et al. [159] found deformation errors up to 0.25 mm,

0.38 mm and 1.8 mm in the AP, LR and SI directions, respectively, over 30 deformation cycles compared to 0.45 mm, 0.41 mm and 0.29 mm in this work. Yeo et al. [157] found mean 3D deviations in deformation reproducibility up to 0.25 mm over 50 consecutive deformations compared to 1.1 mm in this work.

5.4.4 Summary

There are several other deformable dosimetry systems that are currently in development or currently being used. DEFGEL [157] is a polymer gel; Presage-Def [158] and FlexyDos [72] are radiochromic leuco dye based systems, and all three are read out using optical CT imaging. A methacrylic acid based gel dosimeter using MRI readout [156] has also been developed and used to measure deformable dose. These dosimeters all vary slightly in their composition, but each one certainly exceeds the dose resolution of the x-ray CT read out dosimeter described in this work and they can be used at much lower dose ranges whereas this system cannot. However, it has been shown that accurate measurement of higher doses, up to 20 Gy, is possible with this system which makes it ideal for measuring the delivery of multiple fractions or high dose fractionation schemes such as stereotactic body radiation therapy (SBRT). Also, the use of an accessible, existing imaging modality that is integrated into the clinical treatment process as is the case with x-ray CT not only removes a layer of uncertainty in the dose measurement process, but makes its clinical utility more appealing. Overall this deformable dosimetry system has produced excellent dosimetric and deformation results and its unique read out technique gives the system potential for use in unique clinical applications.

5.5 Conclusion

This work introduces a deformable x-ray CT polymer gel dosimetry system. The dose response of the deformable system was similar to a previous non-deformable dosimetry system indicating a successful transition to a deformable gel container with no effects from oxygen contamination on the overall dose calibration. It is however possible that oxygen contamination may have contributed to a drop in dose response near the edge of the gel container. When compared to a Monte Carlo dose calculation, a self-calibrated deformable gel had a mean dose difference of 1.5% relative to the maximum delivered dose of 20 Gy and a gamma pass rate of 97.9% using a 3%/3mm

criterion. The deformable dosimeter showed good overall spatial dose uniformity throughout the dosimeter with some discrepancies near the edges. Fiducial markers were able to accurately track shifts and deformations within the dosimeter and it was determined that the deformable dosimetry system was able to achieve sub-millimetre setup accuracy on the CT couch. The dosimeter was found to resist any permanent damage when externally compressed by up to 30 mm, with these compressions causing average internal deformations of 13 mm. Finally, the deformable dosimeter was shown to deform and relax in a reproducible manner over 100 consecutive deformations. In summary, a new x-ray CT polymer gel deformable dosimetry system has been developed with characteristics suitable for clinical application to the validation of deformable dose for high dose treatments such as SBRT.

Chapter 6

Results and Discussion III: Evaluation of a Deformable Dose Accumulation Algorithm

6.1 Introduction

As was described in Chapter 5 a number of deformable dosimeters have been developed and some of these systems have moved towards preliminary clinical applications, evaluating the results of deformable dose accumulation algorithms and deformable image registration (DIR) algorithms [156, 158, 160, 161]. This chapter will present the results of a comparison of dose measured by the deformable dosimeter introduced in the previous chapter and dose calculated by a novel deformable dose accumulation algorithm, defDOSXYZ, developed by Dr. Emily Heath of the Carleton Laboratory for Radiotherapy Physics at Carleton University [30]. This is also the first example of warped dose measured using an x-ray CT read out gel dosimetry system. In chapter 4, the accuracy and precision of dose measurements made with this type of dosimetry system were established and in chapter 5 this system was extended to allow for deformable dose measurements including an initial characterisation. In this work, the correspondence between the dose distribution measured with the deformable gel and the dose distribution calculated with defDOSXYZ was studied.

In this chapter dose comparisons between the deformable gel and defDOSXYZ are initially performed in a static case to provide a control measurement and to evaluate the results without the added uncertainty of an applied deformation. Following these

results is a comparison of warped dose calculated by defDOSXYZ and dose measured by a deforming gel. Possible error sources are discussed and suggestions for improvement are proposed. An article reporting on the work in this chapter is currently in preperation. Section 6.2 will provide detailed experimental procedures specific to these measurements, section 6.3 presents the results of these experiments, section 6.4 discusses the significance of these results and their relation to other deformable dosimetry systems and section 6.5 summarizes the conclusions of this work.

6.2 Materials and Methods

In the following sections the X, Y and Z directions are defined as the left-right, anterior-posterior and superior-inferior directions, respectively. Gels were compressed in the superior-inferior, or Z, direction.

6.2.1 Gel Fabrication

Deformable gels were fabricated and stored as described in section 5.2.1 and an example of one of these dosimeters can be seen in figure 3.1. Wax beads, approximately 3 mm in diameter, were added to these gels to evaluate gel deformation and setup, as well as to provide guidance for the DIR algorithm to register the gel image sets. As with previous deformable gels, no blank gels were made as the deformable gels were imaged prior to irradiation to allow for background subtraction. For these experiments three deformable gels were made: two as control gels for static deliveries and one for deformable measurements.

6.2.2 Treatment Planning and Irradiation

All gels were irradiated with a treatment plan calculated in ECLIPSE® which consisted of a single 3.5 $\times$ 5 cm^2 open field at a gantry angle of 270°. Both secondary collimators for this field were set up with one jaw at isocentre to create an asymmetrical field. This plan and collimator configuration was chosen to provide a simple dose distribution to more easily evaluate and visualize the deformed dose distribution and to maximize the dose gradient at one edge of the delivered dose field. The maximum dose in the single field plan was 20 Gy as recommended in sections 4.4.4 and 5.4.4 to minimize any dose saturation effect while still producing a significant dose response

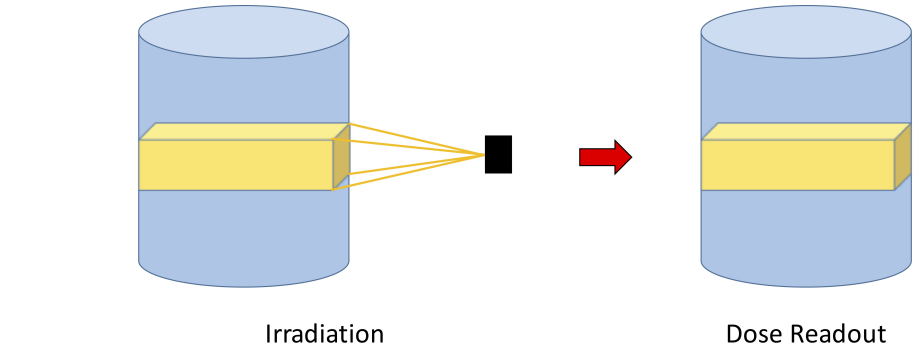

(a)

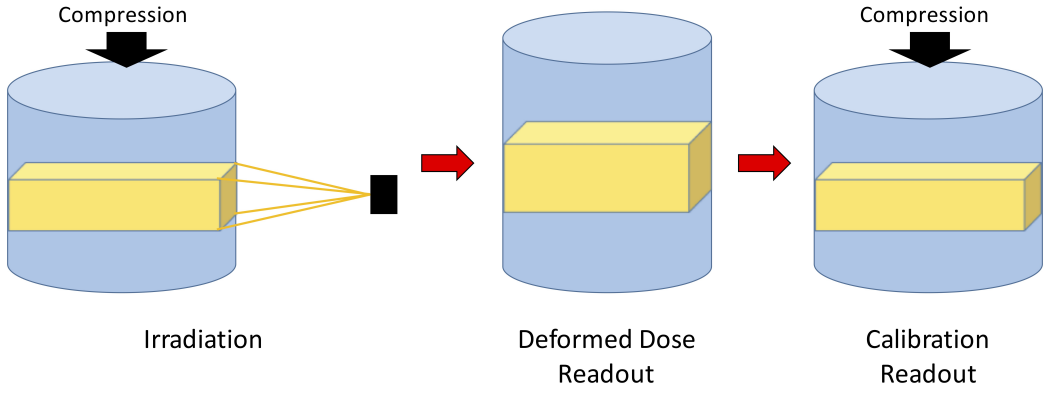

(b)

Figure 6.1: (a) For static measurements, first a background scan of the gel was acquired, then it was irradiated and read out in an uncompressed state to serve as a control measurement. (b) For the deforming measurement, first background scans of the gel were acquired in the compressed and uncompressed state. The gel was then irradiated in a compressed state, read out in an uncompressed state to measure the deformed dose, and read out in a compressed state for calibration.

[1, 184]. For the static measurements the gels were irradiated in an uncompressed state and read out in the same uncompressed state as can be seen in figure 6.1a. The deformable measurement was performed by irradiating the gel in a compressed state and reading out the deformed dose in an uncompressed state as seen in figure 6.1b. The treatment plans for irradiating compressed and uncompressed gels can be seen in figure 6.2. Gels were setup in a 1 L plastic jar that fit into an acrylic base as described in chapter 5 and as seen in figure 5.2a; this setup was shown to be reproducible with sub-millimetre setup errors. For static measurements, the gels were simply set up in the acrylic base phantom and irradiated. For the deformable measurement the gel was compressed externally by 25 mm using an acrylic piston with the same procedure for gel compression described in chapter 5; an image of a deformable gel compressed in this manner can be seen in figure 6.3.

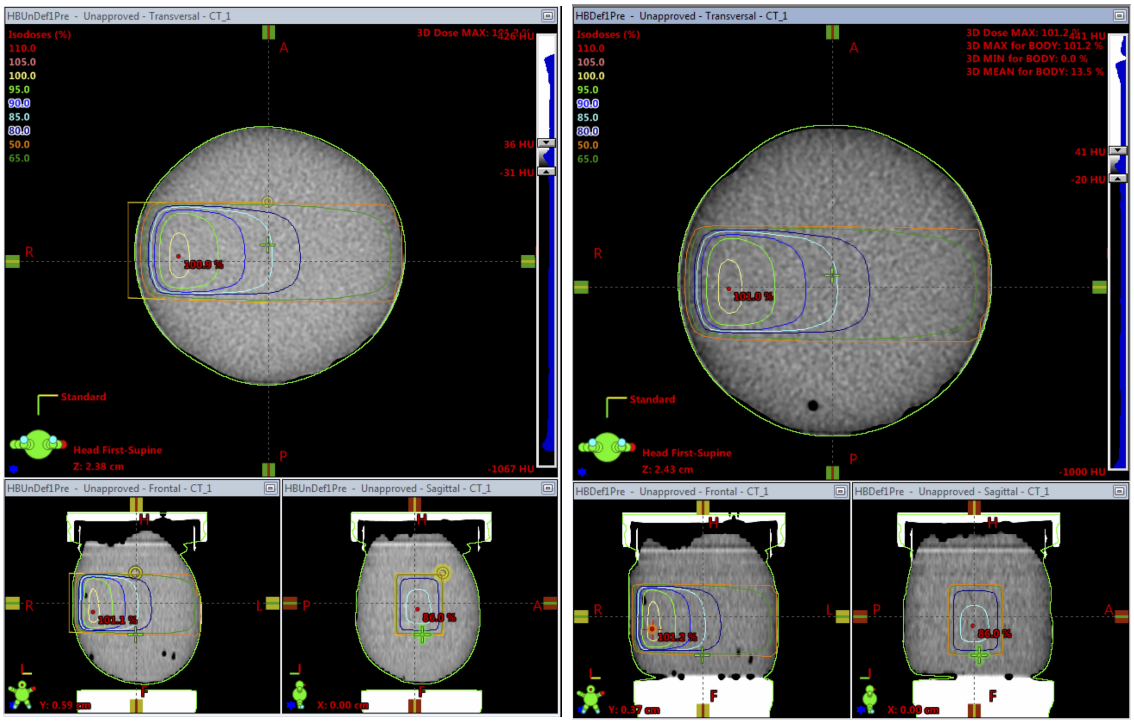

(a) (b)

Figure 6.2: Treatment plans calculated in ECLIPSE® of the single-field plan delivered to deformable gels in (a) an uncompressed state and (b) a compressed state. Dose distributions are shown for each plan in the XY (top), ZX (bottom left) and ZY (bottom right) planes.

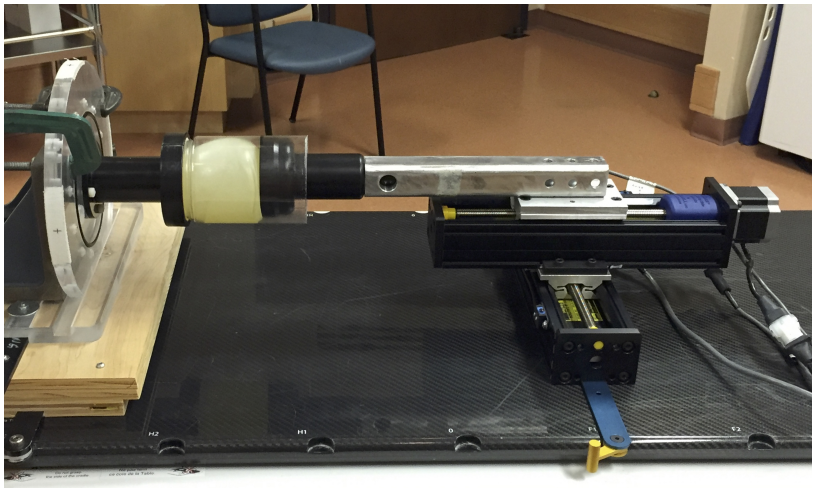

Figure 6.3: A deformable gel setup on the CT scanner bed as it is compressed by the acrylic piston connected to a stepper motor.

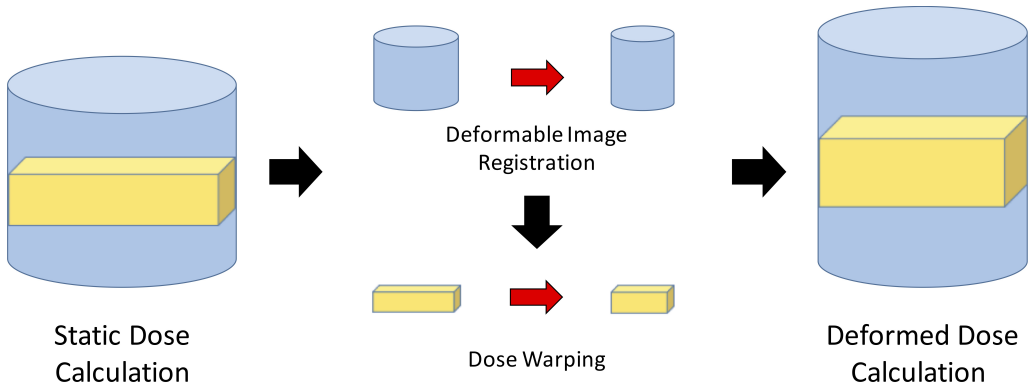

Figure 6.4: A simple diagram showing the process by which dose is warped from the compressed gel state to the uncompressed gel state.

6.2.3 Dose Calculation

Dose delivered to the gel dosimeter was calculated in multiple ways. For static measurements dose was calculated using the TPS, as shown in figure 6.2a and also by the Vancouver Island Monte Carlo (VIMC) system [165]. The dose calculation from VIMC was calculated as dose to water with 0.5% statistical uncertainty in voxels of size 2.5 × 2.5 × 2.5 mm^3 and this dose was used to perform calibration of the static gels. Dose was also calculated using defDOSXYZ so as to compare this dose calculation algorithm to gel measured dose in the static case. Dose calculated using defDOSXYZ had 0.5% statistical uncertainty and voxels of size 2 × 2 × 2.5 mm^3. For both VIMC and defDOSXYZ dose calculations the dose was resampled to 0.5 × 0.5 × 2.5 mm^3 to match the voxel size of gel measurements.

For the deforming measurement, dose was calculated by the TPS, VIMC and defDOSXYZ on the gel in the compressed state and then the dose was warped to the uncompressed state by defDOSXYZ. This dose warping used deformation vectors obtained using the commercial DIR algorithm Velocity AI (Velocity Medical Solutions, Atlanta, GA, Version 3.2) [130]. Velocity AI was used to register the uncompressed gel images to the compressed gel images using a structure-guided registration; this process used wax bead locations within the gel images to guide the registration. The accuracy of the registration was quantified using the target registration error, which is a measure of the distance between actual and estimated positions of targets (wax beads). For the gel deformation the target registration error in Velocity was found to be 1.1 ± 0.6 mm. A simple diagram of the dose warping process can be seen in figure 6.4. All defDOSXYZ dose calculations and DIR calculations were performed by Dr. Emily Heath of the Carleton Laboratory for Radiotherapy Physics at Carleton University [30].

6.2.4 CT Imaging

All gels were imaged using the procedures described in chapters 4 and 5 with parameters that have been optimized for x-ray CT gel dosimetry [121, 123]. For static measurements the gels were imaged in the uncompressed state prior to irradiation to acquire background images and imaged after irradiation for readout. For the deformable measurement the gel was imaged in both the compressed and uncompressed state prior to irradiation to acquire background images; both of these image sets were also needed to facilitate the DIR as seen in figure 6.4. After irradiation the gels were

imaged in the compressed state for a calibration readout and imaged in the uncompressed state for the deformed dose readout, as seen in figure 6.1b. It is expected that the volumetric scan prior to irradiation with the static measurements would deposit 1 Gy of imaging dose and the two scans for the deforming measurement would deposit 2 Gy of imaging dose [124].

6.2.5 Image Processing and Calibration

Image processing of CT images prior to calibration was performed as described in detail in Chapter 3. Due to the variability in dose response seen in deformable gels, interbatch calibration was not possible and it was necessary to perform a self-calibration for each dosimeter. Calibration was performed as described in previous chapters using the VIMC calculated dose, however, due to the nature of the single field plan that was delivered to the dosimeters in this work a gradient threshold was not used during calibration as had been done in previous chapters. Removing areas of high dose gradient from the calibration using this type of plan would have removed large sections of data from the calibration and many dose levels in the optimal range of the dosimeter would not have been represented. The outer 20 mm of the dosimeter was removed from calibration and dosimetric data and is not displayed in any of the results here; this was due issues with the uniformity of the dose response at the edge of the gel as was previosuly discussed in Chapter 5. To ensure positioning agreement between the gel measurement and dose calculation in these high-dose gradient regions, the gel measurement data was shifted for calibration so that field edges matched. In the case of the static measurements these shifts were no more than 1 mm.

For the deforming measurement the gel was irradiated in the compressed state, deformed dose was read out in the uncompressed state, and calibration data was read out in the compressed state. Due to a discrepancy in compression of the gel between irradiation and readout, the planned and read out dose distributions in the compressed state did not match. This can be seen in profiles comparing the gel read out dose and VIMC calculated dose for the compressed gel in figure 6.5. The compression of the gel has been slightly released between irradiation and readout causing the dose profile across the field to shrink slightly as the field gets smaller in this direction when the gel becomes less compressed. In order to calibrate this gel the plan was shifted in the Y direction so that one edge of the profiles matched and could provide data in the dose ranges covered by the edge of the field; the other edge of the

field was removed from the calibration data. The plan was not shifted in the X or Z direction as it was not necessary to match the field edges for calibration. Figure 6.6a shows the shifted profiles with one edge of the field matched and figure 6.6b shows an image of the gel measured data that was used for calibration with the mismatched edge of the field removed.

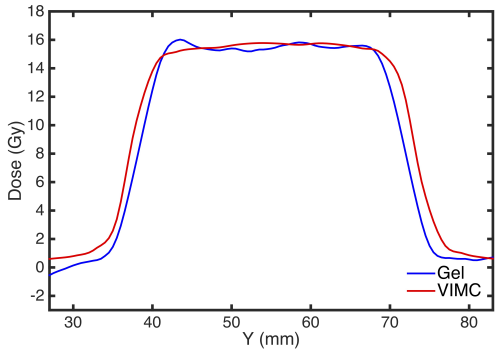

Figure 6.5: Profiles in the Y direction comparing the compressed deformable gel measurement used for calibration compared to VIMC dose calculated in the compressed gel.

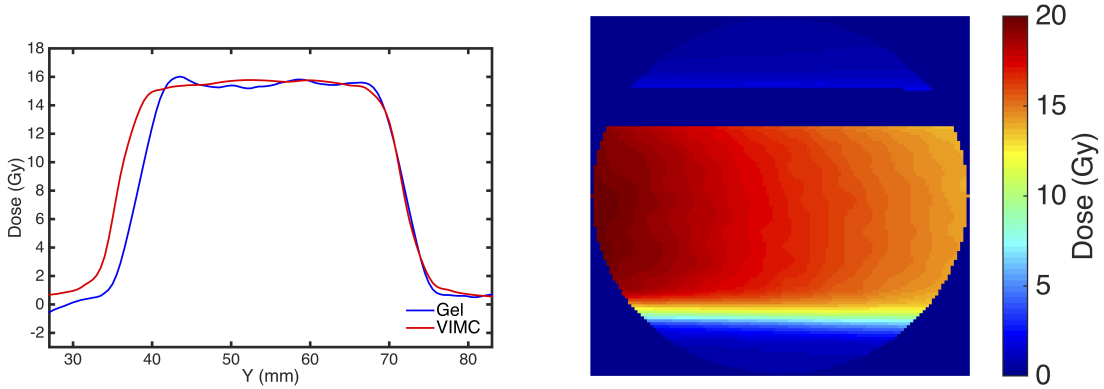

(a)

(b)

Figure 6.6: (a) Profiles in the Y direction comparing the compressed deformable gel used for calibration compared to VIMC dose calculated in the compressed gel after shifting the the calculated dose to align one edge of the profile and (b) a masked image of the calculated dose that was used for calibration so as to only include the matched field edge.

6.3 Results

6.3.1 Static Dose Measurements

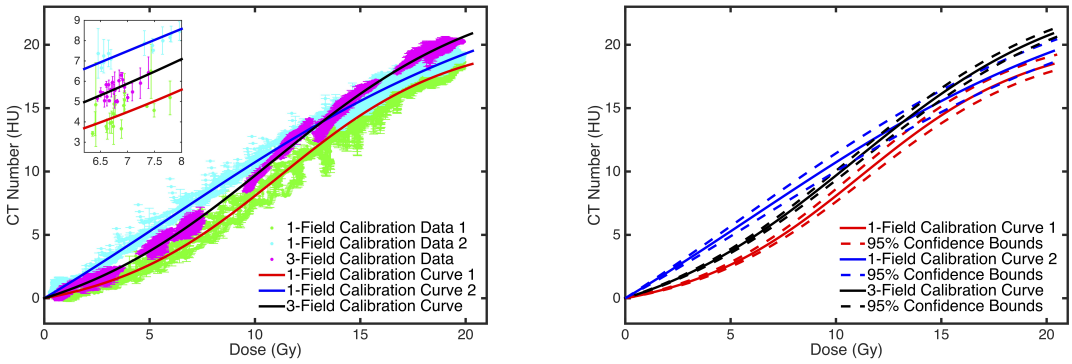

(a) (b)

Figure 6.7: (a) Dose response curves for two deformable gels calibrated using single field plan and one deformable gel calibrated using a 3-field calibration plan as in chapters 4 and 5. All points used in the calibration are included and an inset figure showing an enlarged section of the plot with some data points removed to more clearly illustrate the uncertainty in the CT data. (b) Dose response curves of the same three deformable gels including confidence bounds that are based on the fitting parameters to give an example of the uncertainty on these fits.

Figure 6.7 displays calibration data for the two static single-field gel measurements as well as calibration data from a static deformable gel irradiated with a 3-field calibration plan from Chapter 5. In figure 6.7a these curves are shown with all binned CT data points used in the fitting process for each curve and an inset shows an enlarged portion of the curves to illustrate the uncertainty in the CT data. The same curves without the CT data and including 95% confidence bounds are displayed in figure 6.7b; the confidence bounds are based on uncertainty in the fitting parameters (described in Chapter 3) and give a measure of the uncertainty on these fits. These calibration results show that calibration using a single field without a gradient threshold has been successful as the single-field calibration curves follow the same general shape as the 3-field calibration curve. The inclusion of the high-dose gradient region in this calibration method has caused an increase in uncertainty of the fit as both the binned CT data in figure 6.7a and the confidence bounds in figure 6.7b are spread wider for the single-field calibrations. There is also more variation in the dose response between each gel than was seen in Chapter 4 with the non-deformable gels

or in Chapter 5 using 3-field calibration plans on deformable gels. In figure 6.7, for a given ΔN_{CT} measured in two different deformable gels, the dose delivered differed by up to 13% relative to the maximum dose. This large difference in dose response lead to the requirement of self-calibration for each gel in these results rather than interbatch or generic dose calibration.

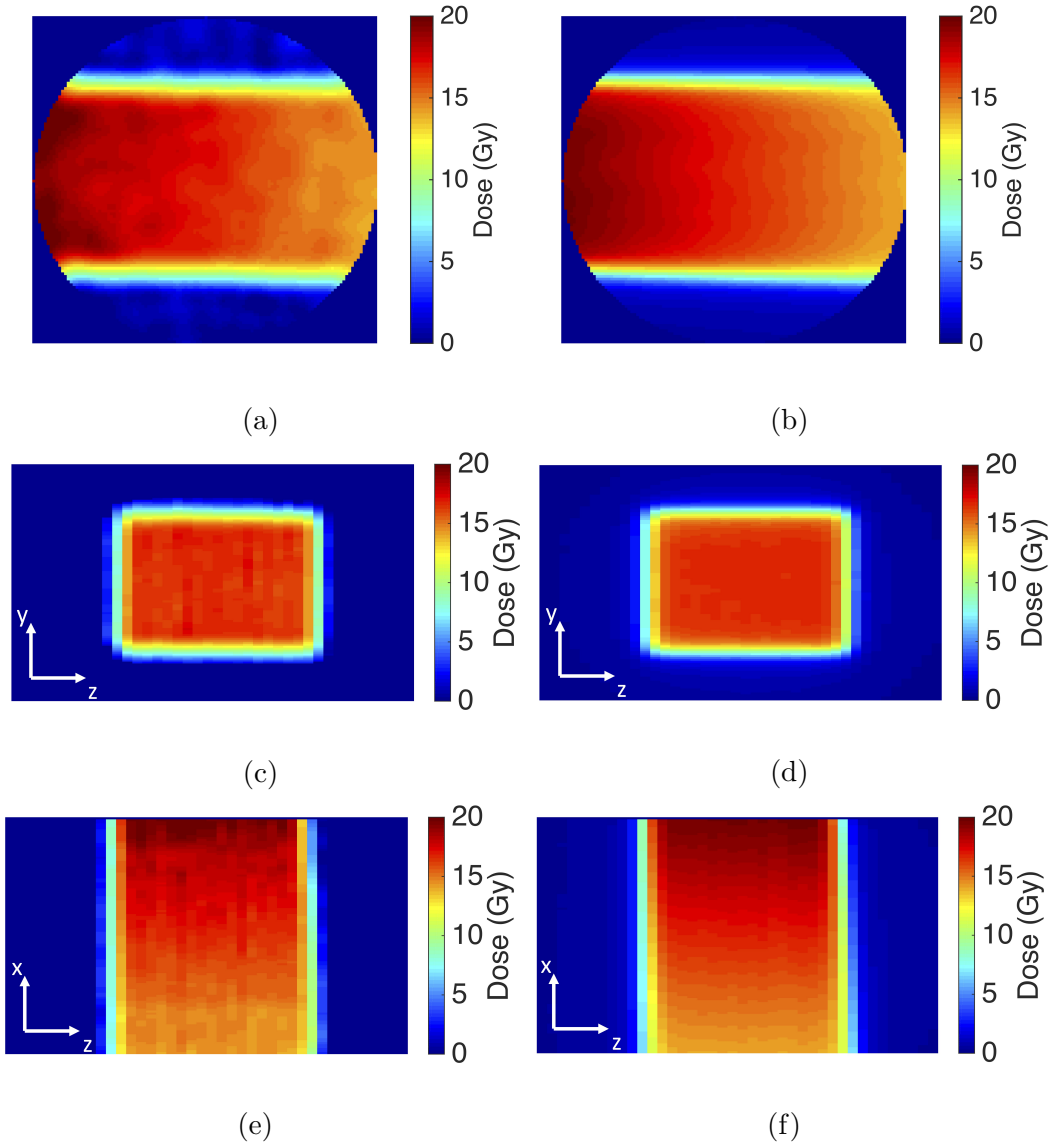

Figure 6.8: Gel measured dose in the (a) XY plane, (c) ZY plane and (e) ZX plane and defDOSXYZ calculated dose (b) XY plane, (d) ZY plane and (f) ZX plane for a static, single field delivery.

The calibrated dose for a static gel and the dose calculated by defDOSXYZ can

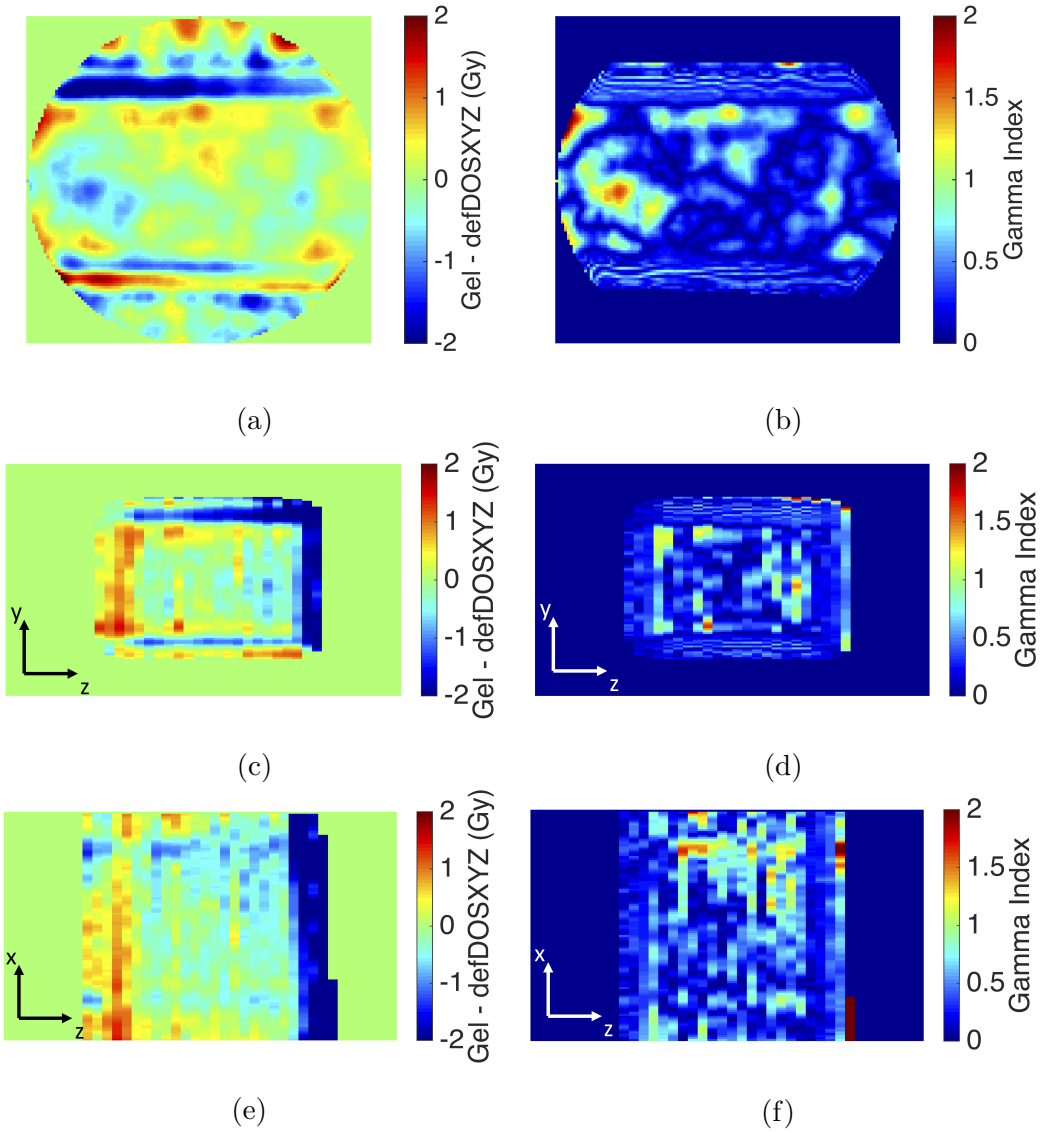

Figure 6.9: Dose comparisons of gel measurement and defDOSXYZ calculation for a static, single field delivery. Dose is compared in the XY plane by (a) dose difference and (b) gamma index, in the ZY plane by (c) dose difference and (d) gamma index, and in the ZX plane by (e) dose difference and (f) gamma index. Gamma index was calculated using a 3%/3mm criteria and 10% dose threshold.

be seen in figure 6.8 with the dose displayed in three different planes; these are the same planes visible in figure 6.2. Figure 6.9 displays dose difference and gamma index comparison of the measured and calculated dose in the same planes. Overall there is good agreement between measured and calculated dose in these comparisons with the largest dose difference discrepancies (up to 2.7 Gy) occuring near the field

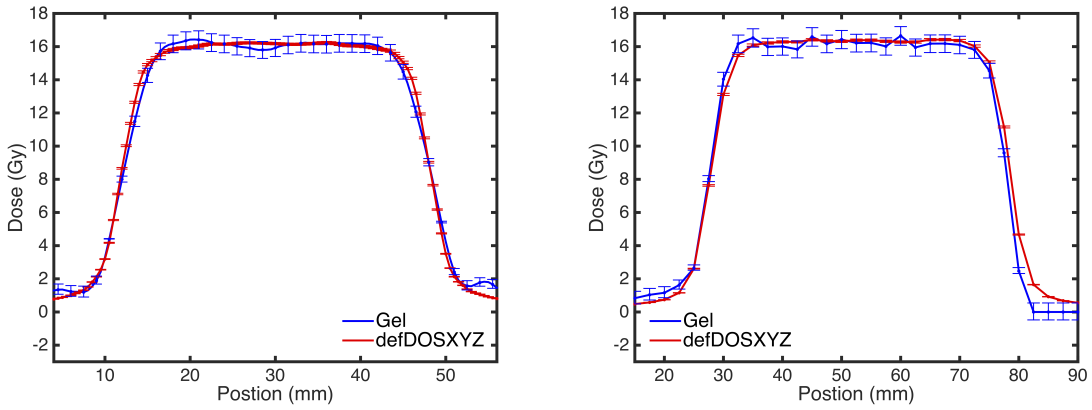

Figure 6.10: Dose profiles comparing gel measurement and defDOSXYZ calculation in the (a) Y and (b) Z directions for a single, static field delivery.

edges. These large dose differences could be the result of a small setup error or field size difference because of the high dose gradient in these regions. When gamma analysis is considered these dose differences do not generally lead to failing gamma index values. The 3D gamma pass rates for this gel when compared to defDOSXYZ was 94.5% when using a 3%/3 mm criterion and 93.3% when using a 3%/2 mm criterion with a dose difference calculated using global normalization and a 10% dose threshold. This is a slight decrease in gamma pass rate when compared to non-deformable gels (98.2%) and deformable gels (97.9%) using a 3-field calibration and a 3%/3 mm criterion as seen in previous chapters. Gamma pass rates with the high-dose gradient regions removed dropped to 93.6% when using a 3%/3 mm criterion and 91.2% when using a 3%/2 mm criterion indicating agreement between gel and calculation was excellent in the high-dose gradient region. These results show that matching of the field edges for calibration was succesful and did not have a negative impact on the dose measurement in that region. In figure 6.10, dose profiles through the centre of the gel comparing measurement and defDOSXYZ calculated dose are displayed. These profiles show good agreement between measurement and calculation with some differences in the low dose region outside the field and an apparent field size discrepancy in the Z direction where the gel measured field is 0.5 mm smaller than the calculated field. The low dose region differences in these profiles are below the 10% dose threshold used for the gamma analysis and therefore do not contribute any failing points. The field size difference led to some of the largest dose differences

at the inferior edge of the gel, seen on the right side of figures 6.9c and 6.9e but did not lead to failure of the gamma criterion.

6.3.2 Deforming Dose Measurements

The position of wax beads within the gel dosimeter in the uncompressed state before and after irradiation are shown in figure 6.11. The first set of bead positions was determined from the background scan on the day of irradiation, the gel was then compressed and irradiated; the second set of bead positions is taken from the readout scan which was performed on the uncompressed gel 24 hours post irradiation. Table 6.1 shows the mean bead displacement over all wax beads within this gel. In Chapter 5, the maximum inter-day setup error over 8 measurements was found to be 0.99 mm and the expected bead shift after a compression of 25 mm was found to be 0.3 $\pm$ 0.3 mm. The results for bead positional error in this gel are higher than would be expected from Chapter 5's results but the increased error could be related to the added transportation and setup required during the irradiation of this gel. The extra transportation and setup of the dosimeter could increase the possibility of rotation or skewing of the dosimeter within the plastic jar which can be difficult to correct during setup.

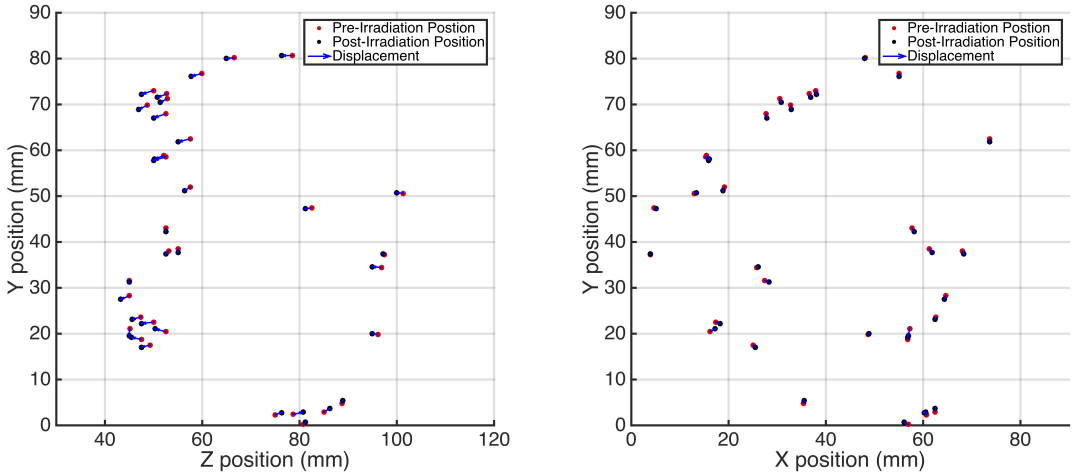

(a) (b)

Figure 6.11: Bead positions within a deformable gel in an uncompressed state before irradiation and after irradiation in the (a) ZY and (b) XY planes.

Figure 6.12 shows the position of wax beads within the gel dosimeter in the un-

Table 6.1: Mean shift of wax beads within the deforming gel for pre- and post-irradiation scans.

	Mean Bead Displacement (mm)	Standard Deviation (mm)
X direction	0.34	0.25
Y direction	0.58	0.32
Z direction	1.47	0.83
3D Movement	1.75	0.63

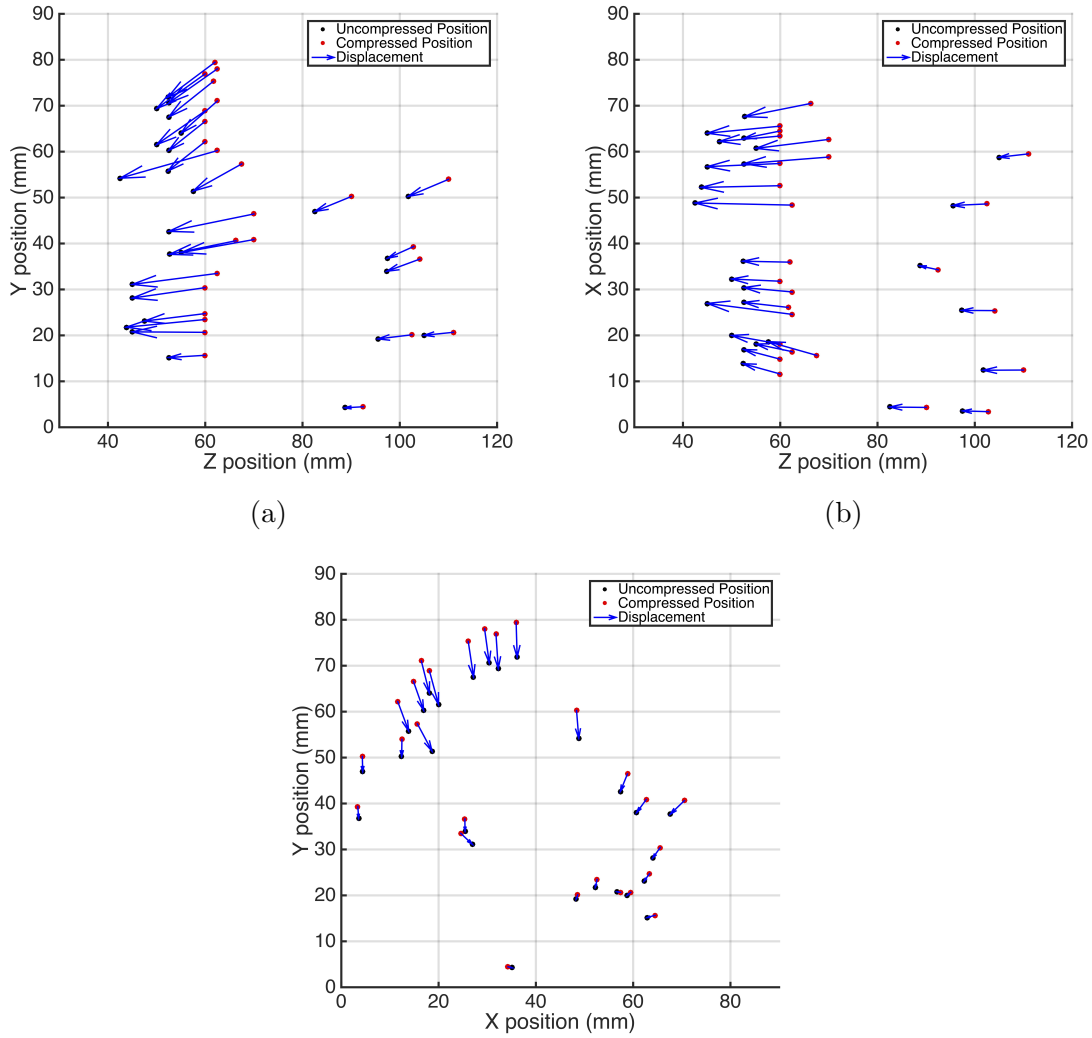

Figure 6.12: Bead positions within a deformable gel comparing uncompressed and compressed states before irradiation in the (a) ZY, (b) ZX and (c) XY planes.

compressed state and the compressed state just prior to irradiation and table 6.2 shows the mean displacement of these beads. The mean internal motion was almost 12 mm for the external compression of 25 mm which agrees with what was found for this level of compression in Chapter 5.

Table 6.2: Mean shift of wax beads within the deforming gel between the uncompressed and compressed state prior to irradiation.

	Mean Bead Displacement (mm)	Standard Deviation (mm)
X direction	1.17	0.90
Y direction	3.90	2.66
Z direction	10.62	4.32
3D Movement	11.75	4.19

The calibration data for the deforming measurement can be seen in figure 6.13. Figure 6.13a shows the calibration curve with all binned CT data used in the calibration and when compared to the data from figure 6.7a there is less data in the mid-range doses because of the need to remove one edge of the field for this calibration. In figure 6.13b the calibration for the deforming gel is compared to a single-field static calibration curve and a three-field calibration curve previously shown in figure 6.7b. Comparing the uncertainty and spread in the CT data between figures 6.7a and 6.13a the modified calibration method does not seem to have had an obvious impact nor has it seem to have affected the confidence bounds of the fit in a drastic way.

Figure 6.14 shows dose calculated by the TPS as it was delivered to compressed gel, and dose warped into the uncompressed gel by the gel measurement and the defDOSXYZ calculation. These dose distributions are shown in the XY, ZY and ZX planes. In the XY plane, the gel measurement shows the field narrowing in the Y direction when the gel is released from compression, with more narrowing at the centre of the gel than near the edges. This agrees with the bead motion seen in figure 6.12c which shows beads with more motion in the Y direction at the centre of the field than near the edges. The dose warping calculation appears to have less narrowing of the field overall, but a larger difference between the centre and edges of the gel. In the ZY plane, figures 6.14e and 6.14f show both a shift and expansion of the dose field in the Z direction when the gel is released from compression. As in figures 6.14b and 6.14c, the field can be seen narrowing in the Y direction as it expands in the Z direction; defDOSXYZ shows more narrowing at the centre of the

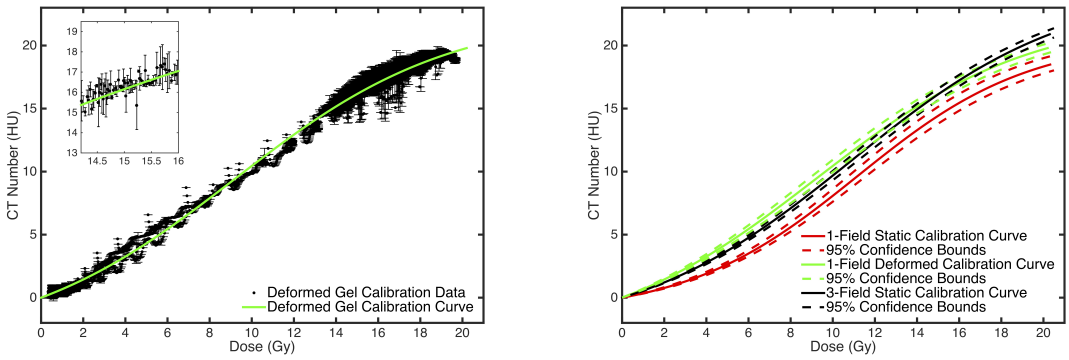

(a) (b)

Figure 6.13: (a) Dose response curve for a deformable gel in a compressed state calibrated using a single field plan with one edge of the field aligned between gel measurement and calculated dose. All points used in the calibration are included and an inset figure showing an enlarged section of the plot with some data points removed to more clearly illustrate the uncertainty in the CT data. (b) Dose response curves from two static deformable gels previously shown in figure 6.7b compared to the deforming calibration curve from figure (a). Confidence bounds have been included that are based on the fitting parameters to give an example of the uncertainty on these fits.

gel and less near the edges whereas the measurement shows a more uniform decrease of the field size in the Y direction. The defDOSXYZ warped dose also shows more expansion of the field in the Z direction than was measured by the gel and the field, in general, is larger in the calculated warped dose distribution. Figure 6.15 displays dose difference and gamma analysis comparing the gel measurement and warped dose calculation in the same planes as shown in figure 6.14. As would be expected, there are large dose differences where the gel measurement and defDOSXYZ disagree on the shape of the field which also leads to the majority of points in these regions failing gamma analysis. The regions with the highest percentage of failing points are at the superior and inferior portions of the field in the Z direction where the defDOSXYZ field extends well beyond the gel measured field. Apart from field shape disagreements, in figure 6.15a and 6.15b there is a region on the right side of the gel where the gel dose is higher than defDOSXYZ by up to 1.8 Gy leading to a large number of points failing the gamma criteria. This difference indicates a sharper drop off in dose with depth for defDOSXYZ compared to measurement. At the bottom of figures 6.15e and 6.15f this disagreement at beam exit is shown to extend throughout the gel in the Z direction. This was not observed in the static case which indicates

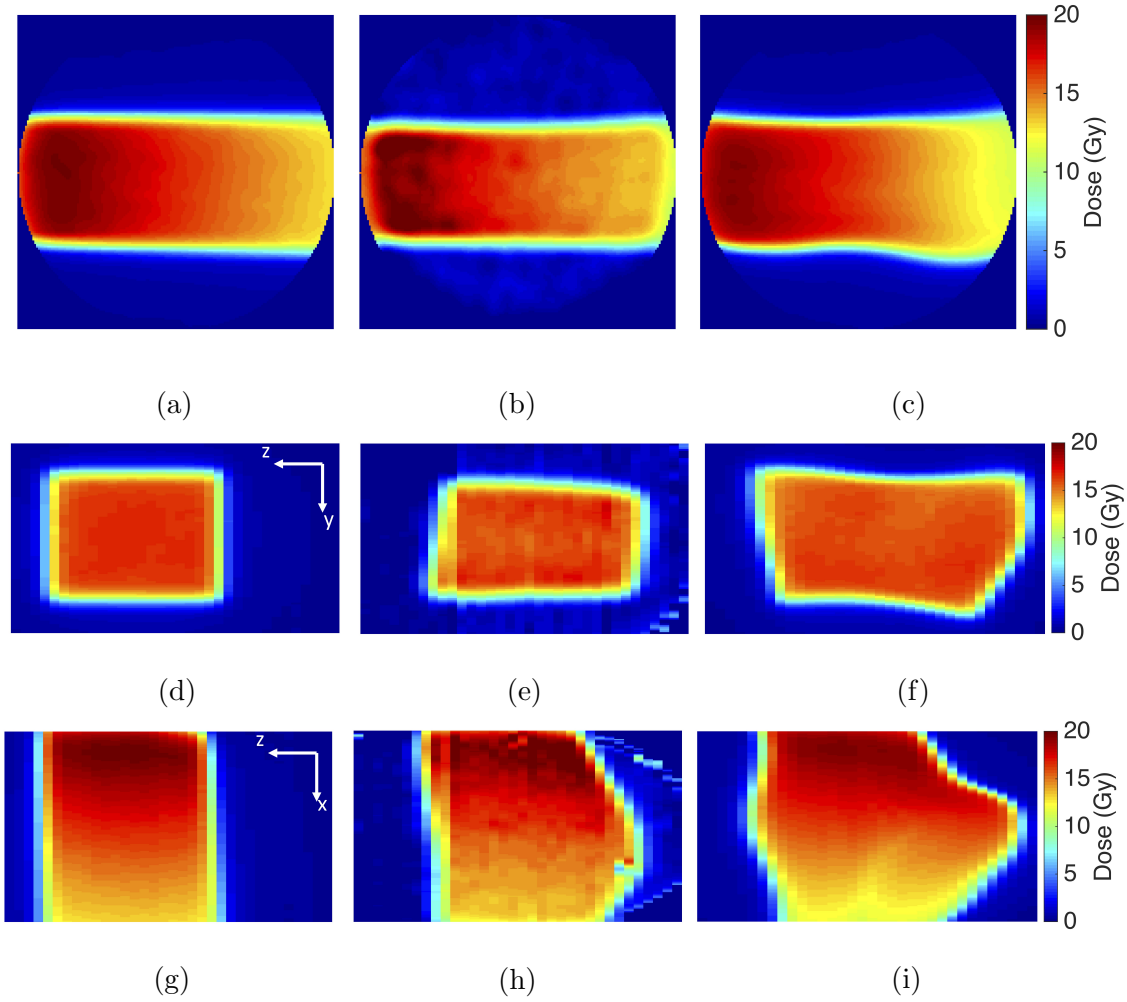

Figure 6.14: Dose maps in the (a-c) XY plane, (d-f) ZY plane and (g-i) ZX plane. Figures (a), (d) and (g) show dose calculated by the TPS in the compressed state, figures (b), (e) and (h) show dose measured by the gel in the uncompressed state, and figures (c), (f) and (i) show dose calculated by defDOSXYZ in the uncompressed state.

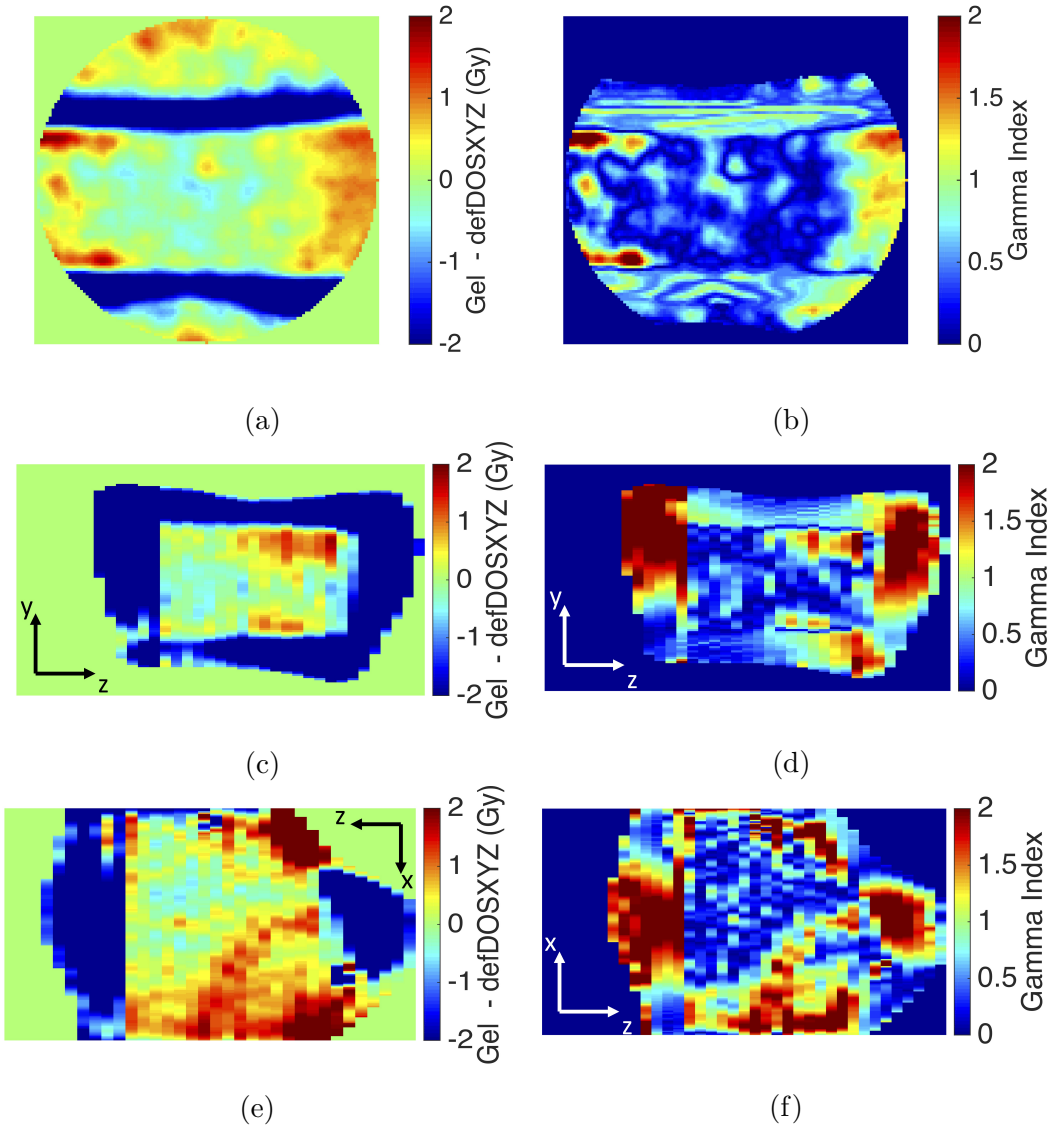

Figure 6.15: Dose comparisons of gel measured dose and defDOSXYZ deformed dose in the uncompressed state of a gel that was irradiated in a compressed state. Dose is compared in the XY plane by (a) dose difference and (b) gamma index, in the ZY plane by (c) dose difference and (d) gamma index, and in the ZX plane by (e) dose difference and (f) gamma index. Gamma index was calculated using a 3%/3mm criteria and 10% dose threshold.

the difference was induced during the deformation of dose; a more compressed field in the X direction would cause the depth dose to fall off more quickly so it is possible that the defDOSXYZ calculation is predicting more compression of dose in X direction than what is seen in measurement. Overall these differences between the defDOSXYZ calculated and gel measured warped dose are significant as the 3D gamma pass rates throughout the gel are 66.0% when using a 3%/3 mm criterion and 56.8% when using a 3%/2 mm criterion which are considerably lower than what was seen for the control measurement.

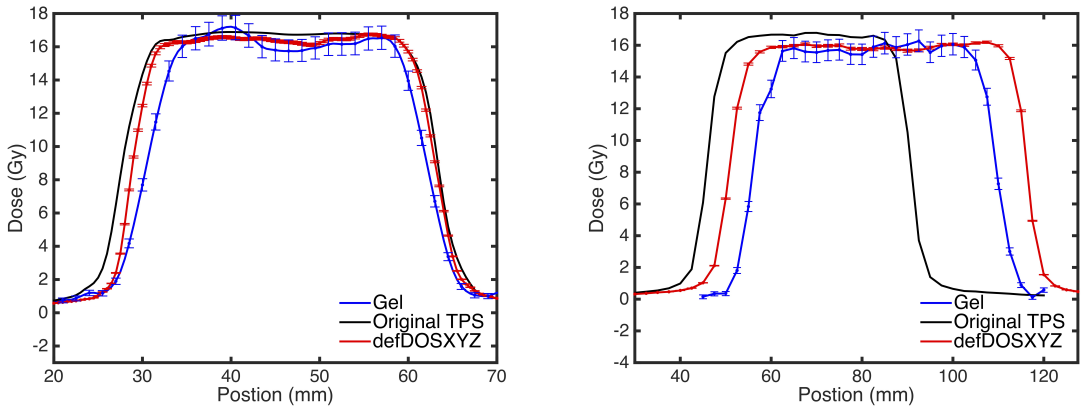

(a) (b)

Figure 6.16: Dose profiles in the (a) Y and (b) Z direction comparing gel measured dose and defDOSXYZ deformed dose in the uncompressed state of a gel that was irradiated a compressed state. The TPS profile is from a dose calculation on the gel in the compressed state.

Figure 6.16 show profiles in the Y and Z direction through the centre of the gel comparing the original TPS calculated dose as delivered to the compressed gel and the warped dose calculated in defDOSXYZ and measured by the gel. In 6.16a the deformation has caused the field to both shift and narrow from the original dose distribution in both the gel and defDOSXYZ dose profiles. The profiles in figure 6.16b show a shift in the Z direction and an expansion of the field from the original calculation with the defDOSXYZ profile displaying a larger shift and expansion than the gel measurement. A comparison of the changes in field position and size from these profiles can be seen in table 6.3. It should be noted that the centre of the gel is where we see the largest disagreement between calculation and measurement in the Z direction. The expansion of the field calculated by defDOSXYZ is not as large near the edges of the gel and there is better agreement with the gel measurement.

Table 6.3: Changes in profile position and width compared to the original dose calculation as measured by the gel and calculated in defDOSXYZ through the centre of the gel.

	Gel Measured Profile Shift	defDOSXYZ Profile Shift	Difference
Y-Profile	0.8 mm	0.5 mm	**0.3 mm**
Z-Profile	14.5 mm	15.3 mm	**0.8 mm**
	Gel Measured Field Width Change	defDOSXYZ Field Width Change	Difference
Y-Profile	-3.7 mm	-1.4 mm	**2.3 mm**
Z-Profile	8.9 mm	20.8 mm	**11.9 mm**

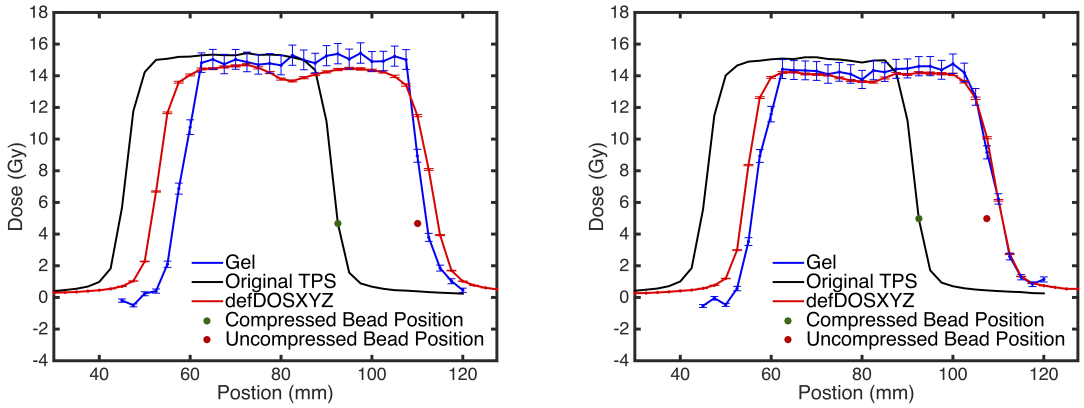

Figure 6.17: Dose profiles in the Z direction from two different locations ((a) and (b)) within the gel showing gel measured dose and defDOSXYZ deformed dose in the uncompressed state of a gel that was irradiated in a compressed state overlaid with the compressed and uncompressed z-coordinates of a wax bead near the orignal TPS dose calculation field edge. From this data the movement of the edge of the field can be compared with the movement of the bead.

In attempt to compare bead movement and the warping of the dose distribution under deformation, figure 6.17 shows the position of beads in the compressed and uncompressed state of the gel overlaid with dose profiles in vicinity of these beads. Table 6.4 compares the movement of these beads from the compressed to uncompressed state to the shift in the inferior edge of the profiles for both the gel measured and defDOSXYZ calculated dose distributions. When compared to the original dose calculation field edges, the gel measured field edges shifted 2.1 and 3.4 mm further than the beads compared to 4.6 and 3.4 mm in the defDOSXYZ dose calculation.

Table 6.4: Inferior field edge shift from the original dose calculation as measured by bead movement, measured in gel dose distribution and measured in defDOSXYZ.

	Bead Movement	Gel Measured Field Edge Shift	defDOSXYZ Field Edge Shift
Z-Profile Near Bead 1	17.5 mm	19.6 mm	22.1 mm
Z-Profile Near Bead 2	15 mm	18.4 mm	18.4 mm

6.4 Discussion

6.4.1 Static Dose Measurements

There is a difference in batch consistency between the non-deformable and deformable dosimetry system that can be seen in figure 6.7b. Due to this difference in dose response between gel batches for the deformable dosimeter, interbatch or generic calibration is not possible as it was for the non-deformable system. In this work the gel has been calibrated with itself, in essence creating a relative dose measurement for the static case; other deformable dosimetry systems have generally used a single large batch of dosimeter material using a portion for calibration and the remaining material for test measurements [156–158]. One possible source of this interbatch inconsistency is oxygen contamination. During the development of the dosimeter finding a deformable container, while keeping the oxygen level within the gel sufficiently low, proved to be a challenge. As described in Chapter 5, it was necessary to increase the amount of oxygen scavenger (THPC) added to the gel from 5 mM to 10 mM when moving to the deformable system and in some cases the addition of additional oxygen

barrier via PVC coating was required. Further investigation is required to determine the exact cause of this interbach variability for the deformable system, as the ability to calibrate between gel batches is a useful feature for a gel dosimetry system.

There are a handful of factors that must be considered when comparing the control measurement for the single field plan to the results of the 3-field calibration of the deformable dosimeter in chapter 5. The maximum dose error in the high dose gradient region is higher (2.7 Gy in single-field compared to 1.4 Gy in 3-field) which can be explained by an increase in dose gradient for the single field plan; in the 3-field calibration plan dose gradients reach a maximum of only 3.5 Gy/mm compared to nearly 6 Gy/mm for the single field plan. One must also consider that in the dose calibration for the single field gel it was not possible to remove regions of high-dose gradient. Comparing the calibration data for the 3-field plan to the single field plan in figure 6.7a illustrates the effect of this change as there is an increase in the range of CT number for a given delivered dose. In addition to this factor, in chapter 5 the deformable dosimeter was both calibrated and compared to VIMC calculated dose whereas in the measurement in this work the gel is calibrated using VIMC but compared to defDOSXYZ as it the dose calculation algorithm that is being evaluated. Although the differences between VIMC and defDOSXYZ are small in the case of static dose delivery its possible this could contribute to the decrease in gamma pass rate in these results.

Overall the results from the static control measurement of this deformable dosimeter (94.5% gamma pass rate using a 3%/3mm criterion) are comparable to those found for other deformable dosimetry systems. For example when using a 3%/3mm criterion, Niu et al. [156] found gamma pass rates of 93.4% and 95.7% for two static measurements of a 12-field plan delivered to a MRI read out deformable gel, Juang et al. [158] found a gamma pass rate of 96.4% when delivering a checkerboard pattern to a static Presage-Def deformable dosimeter, and Yeo et al. [160] found gamma pass rates 99.9% and 96.1% using the optically read out DEFGEL when delivering a single 1×1 cm^2 field and complex stereotactic treatment, respectively.

6.4.2 Deforming Dose Measurements

The warped dose distribution calculated by defDOSXYZ diverges significantly from what is measured by the deforming gel and in general shows more warping of the dose fields than what is measured by the gel. These differences are apparent from both the

dose distributions shown in figure 6.14 and the drastic drop in gamma pass rate when compared to the static measurement. Although there was a change in calibration method between the static and deforming case it did not induce a large change in the uncertainty of the calibration fit to the data and cannot account for the differences between the dose warping calculation and gel measurement. The calculation and measurement generally disagree on the shape of the field but where the fields do overlap there is good agreement between measurement and calculation; the exception to this is in the depth dose where differences in compression of the field in the X direction may have caused disagreement.

The calculated and measured warped fields do seem to agree on the position of the field as in both the Y and Z profiles displayed in figure 6.16 the gel and defDOSXYZ agree within 1 mm on the shift of the field when released from compression. For the changes in field size summarized in table 6.3, however, the measured and calculated warped profiles show larger disagreements that fall outside the spatial accuracy of the setup and deformation that was established in chapter 5. These values are significantly different even when considering the increased position error that was found when comparing the wax beads in the pre- and post-irradiation gel image sets in figure 6.11.

Juang et al. [158] found similar errors when comparing gel measurement and a dose warping calculation with a maximum difference in field size of 14.0 mm compared to 11.9 mm in this work; they also found much larger field position errors with maximum field shift of 9.0 mm compared to 0.8 mm in this work. Niu et al. [156], however found excellent spatial agreement when comparing deformed gel measurement to the MORFEUS deformable dose accumulation algorithm. By comparing isodose levels in measurement and calculation they measured mean vector distances of 1.2 mm between the two.

The agreement between defDOSXYZ and the gel measurement improved when in close proximity to one of the wax beads inserted in the gel to track deformations and used by the DIR algorithm to deform the gel images. In the two instances where a wax bead fell near a dose field edge the predicted field edge locations by defDOSXYZ were within 2.5 mm and 0.1 mm of the gel measured field edge. Although this is a limited sample of data it suggests that the dose warping calculation may improve with a more uniform distribution of trackers to provide better information to the DIR algorithm.

Overall, this work found the deformable dose accumulation algorithm and de-

formable gel dose measurement showed significant disagreement with a gamma pass rate of 66.0% when using a 3%/3mm criterion and 56.8% when using a 3%/2 mm criterion. Other deformable dose calculations have had varying degrees of success when compared with deformable dose measurements. Niu et al. [156] found that MORFEUS, a model-based deformable registration and dose accumulation algorithm, found excellent agreement when comparing calculated warped dose to gel measurement with a gamma pass rate of 96.9% using a 4.7%/3mm criterion. It should be noted, however, that this dose comparison was limited to doses less than 50% of the prescribed dose as oxygen contamination limited the usable region of the dosimeter. Juang et al. [158] found a similar gamma pass rate to this work with 60.0% of points passing using a 3%3mm criterion when comparing gel measured dose and dose warped using the same commercial DIR algorithm, Velocity AI. Yeo et al. [160] evaluated dose warping using 11 different DIR algorithms finding a wide range of gamma pass rates with the best algorithm producing gamma pass rates (3%/3mm criterion) of greater than 99% for simple plans and 95.8% for a dynamic stereotactic plan. They also found that smaller deformations (9 mm) produced better results than larger (20 mm) deformations.

A possible source of error in the gel measurement is the increase in the estimated imaging dose in the background scan of the deforming measurement (approximately 2 Gy) compared to the static measurement (approximately 1 Gy). The calibration readout for the deforming measurement was performed on the same gel after the imaging dose had been deposited so it should be factored into the calibration but this could still have contributed to a change in the shape of the calibration curve. By depositing extra dose prior to irradiation, one would expect the gel to approach a saturation point at a lower dose, but it is not apparent that this has occurred by examining the calibration curves in figure 6.13b. Baxter et al. [124] showed that a volumetric scan of a gel using similar imaging protocols as in this work would induce a ΔN_{CT} of less than 0.2 HU, however that result is based on a gel recipe with a lower dose sensitivity. Given the increased dose sensitivity of the gels in this work and the potential need to take two volumetric scans of the gels prior to irradiation in this deformable dosimetry protocol, this issue may need to be revisited.

Given the poor results here and in other works using Velocity AI with deformable dosimeters [158, 161], it may be beneficial to use a different DIR algorithm to deform the gel images which could improve dose warping in defDOSXYZ. A limited set of results in this work, however, suggest that a more uniform distribution of markers, or

markers strategically implanted near the dose field edge could improve results using this DIR algorithm. A smaller compression of the gel could also lead to improved results as at this deformation level (25 mm) the calculation seemed to overestimate the amount of warping the dose distribution would undergo. Although the comparison between the deformable dose accumulation algorithm and deformable dose measurement showed large disagreement this evaluation has provided valuable information on potential avenues of improvement in the dose calculation method.

6.5 Conclusions

This work evaluates the performance of a novel deformable dose accumulation algorithm, defDOSXYZ, against dose measured by a deformable x-ray CT polymer gel dosimetry system. Agreement between gel measurement and defDOSXYZ in the static case was excellent with gamma pass rates of 94.5% using a 3%/3 mm criterion and 93.3% using a 3%/2 mm criterion. However, when comparing dose warped with a 25 mm compression the gamma pass rates between the gel measurement and dose warping calculation dropped to 66.0% and 56.8%, respectively. In general, the warped dose distribution calculated by defDOSXYZ underwent larger changes to its shape and size than was measured by the gel dosimeter. It was determined that in regions near fiducial markers used to guide the deformable image registration there was better agreement between measurement and calculation which suggests that providing more contrast to the deformable image registration may improve results. This work has also provided a preliminary example of the feasibility of measuring warped dose with a dosimeter that is read out using x-ray CT imaging, an accessible imaging modality that is integrated into the clinical treatment process.

Chapter 7

Conclusions

The work presented in this dissertation investigated the advancement of an x-ray CT polymer gel dosimetry system. Previous work with this system had focused on the initial characterization of the system and with this work builds off those results in an attempt to find its potential role in clinical applications including, primarily, deformable dosimetry. The results are separated into three major parts: an evaluation of the accuracy and precision of the dosimetry system with an investigation into generic and interbatch calibration, the development of a deformable dosimetry system, and the evaluation of a deformable dose accumulation algorithm using the new deformable gel dosimetry system. This chapter will summarize the results presented in this dissertation and discuss future work that could improve or expand on research related to this system.

7.1 Summary of Results

In the first stage of this work, a reproducibility study of an established x-ray CT gel dosimetry system was undertaken to determine the accuracy and precision of dose measurements made using this dosimeter. In this study, there was careful control of factors that could potentially affect dose response with the hope of making interbatch or generic calibration possible. Four calibration methods were investigated for this system: self-calibration, intragel calibration, average or generic calibration and a "most-divergent" or interbatch calibration. When comparing gel measurements to Monte Carlo dose calculation there was excellent agreement when using a generic calibration curve with a mean dose error of 1.8%, mean distance-to-agreement (DTA)

of 0.63 mm and mean gamma pass rate of 96.8% using a 3%3mm criterion. This was only a small decrease in performance from the self-calibration method which had a mean dose error of 1.6%, mean DTA of 0.61 mm and mean gamma pass rate of 98.2%. The most divergent interbatch calibration saw the mean gamma pass rate fall to 90.9% and a difference in dose response between the top and bottom of the gel dosimeter dropped the mean gamma pass rate for intragel calibration to 76.6%. A dose dependent correction factor was developed to address the difference in dose response between the top and bottom of the gel, improving the intragel calibration mean pass rate to 96.8%. Other recommendations that emerged from this work included the need for careful control of the age and chemical lot of NIPAM in the manufacture of gel dosimeters, the limitations of using this system in low-dose regions and an upper limit of 20-25 Gy for the optimal measurement range of this system. The results of this reproducibility study were on par with other gel dosimetry systems including those read out by MRI or optical-CT imaging [107, 155, 171, 174]. Given the excellent spatial accuracy and resolution of the measurements in this work it suggests that this dosimetry system is ideally suited for the measurement high-dose fractionation treatments such as SRS or SBRT. Overall, the work in this study demonstrated the feasibility of interbatch and generic calibration in x-ray CT polymer gel dosimetry and determined some benchmarks for the accuracy and precision of this dosimetry system.

The second study in this dissertation was the development and characterization of a deformable version of the x-ray CT polymer gel dosimetry system. This work introduced the first 3D deformable dosimetry system based on x-ray CT polymer gel dosimetry and established the setup reproducibility, deformation characteristics and dose response of the system. The deformable dosimetry system used the same gel recipe as the non-deformable system but needed a suitable container that would provide the oxygen barrier necessary to allow for full polymerization and still allow for the free deformation of the gel. The container for the deformable gels was a large latex balloon with polyvinyl alcohol and low-density polyethylene serving as additional oxygen barriers. Wax beads were also added to the gel as fiducial markers to track the deformation and setup of the gels. To establish that the dose response of this system did not change with the new container, it was irradiated in the same way as in the reproducibility study of the non-deformable system. The new gel container and setup was effective as an oxygen barrier as the dose response for the new system was comparable to that of the non-deformable system with no apparent effects of oxygen

contamination. Comparison of gel measurements with Monte Carlo dose calculations found excellent dosimetric accuracy, similar to that of the non-deformable dosimetry system, with a mean dose discrepancy of 1.5% in the low-dose gradient region and a gamma pass rate of 97.9% using a 3%/3 mm criterion. To determine the spatial uniformity of the dose response, a deformable gel was irradiated with a plan designed to deliver a uniform dose throughout the gel. The deformable gel showed good overall spatial dose uniformity with a decrease in response within 20 mm of the edge of the container. Setup reproducibility of the system was measured via fiducial markers within the gel that were tracked over 10 intra-day and 8 inter-day setups on the CT scanner. From these measurements it was determined that sub-millimetre setup accuracy was achievable with an average intra-day setup error of 0.32 ± 0.04 mm and an average inter-day setup error of 0.81 ± 0.04 mm. Tracking these markers when the gel was compressed and released from compression allowed for measurements on the limits and reproducibility of gel deformation. Compressing a deformable gel externally by up to 30 mm produced average position errors of the markers that were less than 0.4 mm when released from compression. Compressing a gel over 50 consecutive compressions produced average marker position errors of approximately 1 mm, and a small rotation of the dosimeter led to marker position errors of up to 1.5 mm over 100 consecutive compressions. This study established several important characteristics of the new deformable dosimetry system and set it up for use in the evaluation of deformable dose accumulation algorithms.

The final component of this dissertation was the use of the deformable dosimetry system to measure deforming dose and evaluate its measurements against a novel deformable dose accumulation algorithm, defDOSXYZ. First, gel measurement and defDOSXYZ were compared in a static case, with no deformation, to establish benchmarks for the deformable dose measurements. In the static case there was excellent agreement between measurement and calculation with a gamma pass rate of 94.5% when using a 3%/3mm criterion and 93.3% when using a 3%/2 mm criterion. A single-field plan was then delivered to a gel that was compressed externally by 25 mm which was then read out in the uncompressed state of the gel allowing the dose distribution to deform within the dosimeter. This deformed dose measurement was compared with dose warped by a commercial deformable image registration algorithm and defDOSXYZ. The dose warped by defDOSXYZ underwent significantly more deformation that what was measured by the gel dosimeter, predicting expansions of the field by up 20.8 mm compared to 8.9 mm measured by the gel. Gamma anal-

ysis comparing dose warped by defDOSXYZ and that measured in the deformable dosimeter found only 66.0% of points passing a 3%/3mm criterion and 56.8% passing a 3%/2 mm criterion, a significant drop from the static comparison. These dosimetric errors were well outside the uncertainty in gel dose measurements, gel setup and gel deformations established in the first two studies of this dissertation. A limited set of data in this study suggested that in regions near fiducial markers the agreement between defDOSXYZ and gel measurement improved. This indicates that a better distribution or strategic placement of fiducial markers may improve results. The results from these experiments provide useful information on improvements that could be made in the deformable dose measurement and calculation and represent the first measurement of deforming dose using an x-ray CT gel dosimetry system.

7.2 Future Work

Based on the results of this dissertation, there are clinical applications for which this dosimetry system, both deformable and non-deformable, is equipped. These include the measurement of high-dose fractionation schemes such as SRS and SBRT and the evaluation of deformable dose accumulation algorithms. One issue that could hinder the use of this system in certain clinical situations is the effect of lower dose response near the edge of the gel container. This was an issue in both the non-deformable and deformable systems and has also been seen in other gel dosimetry systems. It is worth investigating whether storage and cooling of the dosimeter or oxygen contamination near the edge of the container are potential causes of this effect and whether it can be mitigated in any way. If mitigation of this effect is unsuccessful, a correction factor could be calculated to recover the dosimetric information near the edge of the container. This would require the irradiation of several dosimeters with a uniform dose, as was performed for one gel in Chapter 5, to determine the average expected drop off in dose response in order to generate a correction factor. One would need to establish whether the correction would be uniform along the length of the gel, is dose dependent, and whether it is affected by the shape of the container. An additional benefit of this type of study would be the ability to calculate a correction factor for the change in dose response at the top and bottom of the dosimeter. This was done between two specific locations in the non-deformable dosimeter in Chapter 4, but a set of uniform irradiations would allow for the calculation of a correction factor along the entire length of the gel. A successful correction for dose measurements at

the edge of gel dosimeters would allow for surface dosimetry measurements and dose measurements at boundaries where there are large changes in density, both of which are clinically relevant scenarios. In terms of advancement of the deformable dosimetry system there are two major areas where improvements are possible. The first is the issue of oxygen contamination which significantly affected the interbatch variability of the dose response for the deformable dosimeters and made cross batch calibration impossible. The second was the distribution and placement of fiducial markers within the gel which, if improved, could aid in the deformable image registration of warped gel images and deformable dose calculations. One possible solution to both of these problems could be the implementation of 3D printing in the gel fabrication process. With 3D printing, a more oxygen impermeable container with a more consistent oxygen barrier could be constructed and, with the use of dissolvable support material, fiducial markers could be printed with the container to more strategically place the markers. A 3D printed container could also allow for more anthropomorphic dosimeters or facilitate the use of a deformable gel dosimeter in an anthropomorphic phantom, creating more clinically relevant dose measurements. One can imagine the ideal end goal of this area of research where an adaptive radiation therapy treatment is required to pass an end-to-end test in which a deforming anthropomorphic phantom containing one or more deformable gel dosimeters is irradiated. A deformable dosimeter would be uniquely able to address this challenge and the dosimetry system investigated in this dissertation is approaching the capability to make this type of measurement.

Bibliography

[1] E. Maynard, M. Hilts, E. Heath, and A. Jirasek, "Evaluation of accuracy and precision in polymer gel dosimetry," *Med. Phys.*, vol. 44, no. 2, pp. 736–46, 2017.

[2] Canadian Cancer Societys Advisory Committee On Cancer Statistics, *Canadian Cancer Statistics 2017*. Canadian Cancer Society, 2017.

[3] G. Delaney, S. Jacob, C. Featherstone, and M. Barton, "The role of radiotherapy in cancer treatment: Estimating optimal utilization from a review of evidence-based clinical guidelines," *Cancer*, vol. 104, no. 6, pp. 1129–1137, 2005.

[4] H. E. Johns and J. R. Cunningham, *The Physics of Radiology*. Charles C Thomas, 1969.

[5] F. M. Kahn, *The Physics of Radiation Therapy*. Lippincott Williams and Wilkins, 2003.

[6] M. Joiner and A. van der Kogel, *Basic Clinical Radiobiology*. Hodder Arnold, 2009.

[7] S. Webb, "The physical basis of IMRT and inverse planning," *British Journal of Radiology*, vol. 76, no. 910, pp. 678–689, 2003.

[8] J. Staffurth, "A review of the clinical evidence for intensity-modulated radiotherapy.," *Clin. Oncol. (R. Coll. Radiol).*, vol. 22, no. 8, pp. 643–57, 2010.

[9] K. Otto, "Volumetric modulated arc therapy: IMRT in a single gantry arc," *Med. Phys.*, vol. 35, no. 1, p. 310, 2008.

[10] C. C. Popescu, I. a. Olivotto, W. a. Beckham, W. Ansbacher, S. Zavgorodni, R. Shaffer, E. S. Wai, and K. Otto, "Volumetric modulated arc therapy improves

dosimetry and reduces treatment time compared to conventional intensity-modulated radiotherapy for locoregional radiotherapy of left-sided breast cancer and internal mammary nodes.," *Int. J. Radiat. Oncol. Biol. Phys.*, vol. 76, no. 1, pp. 287–95, 2010.

[11] D. Palma, E. Vollans, K. James, S. Nakano, V. Moiseenko, R. Shaffer, M. McKenzie, J. Morris, and K. Otto, "Volumetric modulated arc therapy for delivery of prostate radiotherapy: comparison with intensity-modulated radiotherapy and three-dimensional conformal radiotherapy.," *Int. J. Radiat. Oncol. Biol. Phys.*, vol. 72, no. 4, pp. 996–1001, 2008.

[12] L. Van Benthuysen, L. Hales, and M. B. Podgorsak, "Volumetric modulated arc therapy vs. IMRT for the treatment of distal esophageal cancer.," *Med. Dosim.*, vol. 36, no. 4, pp. 404–9, 2011.

[13] E. J. Hall, "Intensity-modulated radiation therapy, protons, and the risk of second cancers.," *Int. J. Radiat. Oncol. Biol. Phys.*, vol. 65, no. 1, pp. 1–7, 2006.

[14] E. Shaw, C. Scott, L. Souhami, R. Dinapoli, R. Kline, J. Loeffler, and N. Farnan, "Single dose radiosurgical treatment of recurrent previously irradiated primary brain tumors and brain metastases: Final report of RTOG protocol 90- 05," *Int. J. Radiat. Oncol. Biol. Phys.*, vol. 47, no. 2, pp. 291–298, 2000.

[15] S. Benedict, K. Yenice, D. Followill, J. Galvin, W. Hinson, B. Kavanagh, P. Keall, M. Lovelock, S. Meeks, L. Papiez, T. Purdie, R. Sadagopan, M. Schell, B. Salter, D. Schlesinger, A. Shiu, T. Solberg, D. Song, V. Stieber, R. Timmerman, W. Tome, D. Verellen, L. Wang, and F.-F. Yin, "Stereotactic body radiation therapy: The report of AAPM Task Group 101," *Med. Phys.*, vol. 37, no. 8, 2010.

[16] G. A. Ezzell, J. M. Galvin, D. Low, J. R. Palta, I. Rosen, M. B. Sharpe, P. Xia, Y. Xiao, L. Xing, and C. X. Yu, "Guidance document on delivery, treatment planning, and clinical implementation of IMRT: Report of the IMRT subcommittee of the AAPM radiation therapy committee," *Med. Phys.*, vol. 30, no. 8, p. 2089, 2003.

[17] G. A. Ezzell, J. W. Burmeister, N. Dogan, T. J. LoSasso, J. G. Mechalakos, D. Mihailidis, A. Molineu, J. R. Palta, C. R. Ramsey, B. J. Salter, J. Shi,

P. Xia, N. J. Yue, and Y. Xiao, "IMRT commissioning: Multiple institution planning and dosimetry comparisons, a report from AAPM Task Group 119," *Med. Phys.*, vol. 36, no. 11, p. 5359, 2009.

[18] Intensity Modulated Radiation Therapy Collaborative Working Group, "Intensity-modulated radiotherapy : current status and issues of interest," *Int. J. Radiat. Oncol. Biol. Phys.*, vol. 51, no. 4, pp. 880–914, 2001.

[19] K. M. Langen and D. T. L. Jones, "Organ Motion and its Management," *Int. J. Radiation Oncology Biol. Phys.*, vol. 50, no. 1, pp. 265–278, 2001.

[20] A. Bel, M. van Herk, H. Bartelink, and J. V. Lebesque, "A verification procedure to improve patient set-up accuracy using portal images," *Radiother. Oncol.*, vol. 29, no. 2, pp. 253–260, 1993.

[21] J. P. Bissonnette, T. G. Purdie, J. A. Higgins, W. Li, and A. Bezjak, "Cone-Beam Computed Tomographic Image Guidance for Lung Cancer Radiation Therapy," *Int. J. Radiat. Oncol. Biol. Phys.*, vol. 73, no. 3, pp. 927–934, 2009.

[22] B. W. Fischer-Valuck, L. Henke, O. Green, R. Kashani, S. Acharya, J. D. Bradley, C. G. Robinson, M. Thomas, I. Zoberi, W. Thorstad, H. Gay, J. Huang, M. Roach, V. Rodriguez, L. Santanam, H. Li, H. Li, J. Contreras, T. Mazur, D. Hallahan, J. R. Olsen, P. Parikh, S. Mutic, and J. Michalski, "Two-and-a-half-year clinical experience with the world's first magnetic resonance image guided radiation therapy system," *Adv. Radiat. Oncol.*, vol. 2, no. 3, pp. 485–493, 2017.

[23] A. M. Berson, R. Emery, L. Rodriguez, G. M. Richards, T. Ng, S. Sanghavi, and J. Barsa, "Clinical experience using respiratory gated radiation therapy: Comparison of free-breathing and breath-hold techniques," *Int. J. Radiat. Oncol. Biol. Phys.*, vol. 60, no. 2, pp. 419–426, 2004.

[24] D. Yan, F. Vicini, J. Wong, and A. Martinez, "Adaptive radiation therapy," *Phys. Med. Biol.*, vol. 42, pp. 123–132, 1997.

[25] S. Lim-Reinders, B. M. Keller, S. Al-Ward, A. Sahgal, and A. Kim, "Online Adaptive Radiation Therapy," *Int. J. Radiat. Oncol. Biol. Phys.*, vol. 99, no. 4, pp. 994–1003, 2017.

[26] L. Xing, J. Siebers, and P. Keall, "Computational Challenges for Image-Guided Radiation Therapy: Framework and Current Research," *Semin. Radiat. Oncol.*, vol. 17, no. 4, pp. 245–257, 2007.

[27] A. Sotiras, C. Davatzikos, and N. Paragios, "Deformable medical image registration: A survey," *IEEE Trans. Med. Imaging*, vol. 32, no. 7, pp. 1153–1190, 2013.

[28] K. K. Brock, D. L. McShan, R. K. Ten Haken, S. J. Hollister, L. A. Dawson, and J. M. Balter, "Inclusion of organ deformation in dose calculations," *Med. Phys.*, vol. 30, no. 3, pp. 290–295, 2003.

[29] M. Rosu, I. J. Chetty, J. M. Balter, M. L. Kessler, D. L. McShan, and R. K. Ten Haken, "Dose reconstruction in deforming lung anatomy: Dose grid size effects and clinical implications," *Med. Phys.*, vol. 32, no. 8, pp. 2487–2495, 2005.

[30] E. Heath and J. Seuntjens, "A direct voxel tracking method for four-dimensional Monte Carlo dose calculations in deforming anatomy," *Med. Phys.*, vol. 33, no. 2, p. 434, 2006.

[31] J. Bernier, E. J. Hall, and A. Giaccia, "Radiation oncology: A century of achievements," *Nat. Rev. Cancer*, vol. 4, no. 9, pp. 737–747, 2004.

[32] Q. T. Le, H. Shirato, A. J. Giaccia, and A. C. Koong, "Emerging treatment paradigms in radiation oncology," *Clin. Cancer Res.*, vol. 21, no. 15, pp. 3393–3401, 2015.

[33] M. Baumann, M. Krause, J. Overgaard, J. Debus, S. M. Bentzen, J. Daartz, C. Richter, D. Zips, and T. Bortfeld, "Radiation oncology in the era of precision medicine," *Nat. Rev. Cancer*, vol. 16, no. 4, pp. 234–249, 2016.

[34] C. Baldock, Y. De Deene, S. Doran, G. Ibbott, A. Jirasek, M. Lepage, K. B. McAuley, M. Oldham, and L. J. Schreiner, "Polymer gel dosimetry.," *Phys. Med. Biol.*, vol. 55, no. 5, pp. R1–63, 2010.

[35] L. J. Schreiner, "True 3D chemical dosimetry (gels, plastics): Development and clinical role," *J. Phys. Conf. Ser.*, vol. 573, p. 012003, 2015.

[36] P. R. Almond, P. J. Biggs, B. M. Coursey, W. F. Hanson, M. Saiful Huq, R. Nath, and D. W. O. Rogers, "AAPM 's TG 51 protocol for clinical reference

dosimetry of high-energy photon and electron beams," *Med. Phys.*, vol. 26, no. 1999, pp. 1–9, 1999.

[37] D. A. Low, J. M. Moran, J. F. Dempsey, L. Dong, and M. Oldham, "Dosimetry tools and techniques for IMRT," *Med. Phys.*, vol. 38, no. 3, pp. 1313–1338, 2011.

[38] F. H. Attix, *Introduction to Radiological Physics and Radiation Dosimetry*. John Wiley and Sons Inc., 1986.

[39] E. G. Yukihara and S. W. McKeever, "Optically stimulated luminescence (OSL) dosimetry in medicine.," *Phys. Med. Biol.*, vol. 53, no. 20, 2008.

[40] V. Feygelman, B. E. Nelms, A. Rosenfeld, T. Kron, F. D'Errico, and M. Moscovitch, "Dose Verification in IMRT and VMAT," *AIP Conf. Proc.*, vol. 145, no. 1, pp. 145–164, 2011.

[41] P. A. Jursinic and B. E. Nelms, "A 2-D diode array and analysis software for verification of intensity modulated radiation therapy delivery," *Med. Phys.*, vol. 30, no. 5, p. 870, 2003.

[42] P. A. Jursinic, "Angular dependence of dose sensitivity of surface diodes," *Med. Phys.*, vol. 36, no. 6, p. 2165, 2009.

[43] D. Létourneau, M. Gulam, D. Yan, M. Oldham, and J. W. Wong, "Evaluation of a 2D diode array for IMRT quality assurance.," *Radiother. Oncol.*, vol. 70, no. 2, pp. 199–206, 2004.

[44] A. Niroomand-Rad, C. R. Blackwell, B. M. Coursey, K. P. Gall, J. M. Galvin, W. L. Mclaughlin, A. S. Meigooni, and C. G. Soares, "Radiochromic Film Dosimetry: Recommendation of AAPM Radiation Therapy Committe Task Group 55," *Med. Phys.*, vol. 25, no. 11, pp. 2093–2115, 1998.

[45] B. M. McCurdy and P. B. Greer, "Dosimetric properties of an amorphous-silicon EPID used in continuous acquisition mode for application to dynamic and arc IMRT," *Med. Phys.*, vol. 36, no. 7, pp. 3028–3039, 2009.

[46] W. van Elmpt, L. McDermott, S. Nijsten, M. Wendling, P. Lambin, and B. Mijnheer, "A literature review of electronic portal imaging for radiotherapy dosimetry.," *Radiother. Oncol.*, vol. 88, no. 3, pp. 289–309, 2008.

[47] M. H. Lin, J. Li, L. Wang, S. Koren, J. Fan, E. Forkal, and C. M. Ma, "4D patient dose reconstruction using online measured EPID cine images for lung SBRT treatment validation," *Med. Phys.*, vol. 39, no. 10, pp. 5949–5958, 2012.

[48] A. Bäck, "Quasi 3D dosimetry (EPID, conventional 2D/3D detector matrices)," *J. Phys. Conf. Ser.*, vol. 573, no. 1, p. 012012, 2015.

[49] M. Wendling, L. N. McDermott, A. Mans, J. J. Sonke, M. Van Herk, and B. J. Mijnheer, "A simple backprojection algorithm for 3D in vivo EPID dosimetry of IMRT treatments," *Med. Phys.*, vol. 36, no. 7, pp. 3310–3321, 2009.

[50] W. van Elmpt, S. Petit, D. De Ruysscher, P. Lambin, and A. Dekker, "3D dose delivery verification using repeated cone-beam imaging and EPID dosimetry for stereotactic body radiotherapy of non-small cell lung cancer," *Radiother. Oncol.*, vol. 94, no. 2, pp. 188–194, 2010.

[51] J. Herzen, M. Todorovic, F. Cremers, V. Platz, D. Albers, a. Bartels, and R. Schmidt, "Dosimetric evaluation of a 2D pixel ionization chamber for implementation in clinical routine.," *Phys. Med. Biol.*, vol. 52, no. 4, pp. 1197–208, 2007.

[52] B. E. Nelms, H. Zhen, and W. a. Tome, "Per-beam, planar IMRT QA passing rates do not predict clinically relevant patient dose errors," *Med. Phys.*, vol. 38, no. 2, p. 1037, 2011.

[53] J. J. Kruse, "On the insensitivity of single field planar dosimetry to IMRT inaccuracies," *Med. Phys.*, vol. 37, no. 6, p. 2516, 2010.

[54] G. Yan, C. Liu, T. a. Simon, L.-C. Peng, C. Fox, and J. G. Li, "On the sensitivity of patient-specific IMRT QA to MLC positioning errors.," *J. Appl. Clin. Med. Phys.*, vol. 10, no. 1, p. 2915, 2009.

[55] D. Letourneau, J. Publicover, J. Kozelka, D. J. Moseley, and D. a. Jaffray, "Novel dosimetric phantom for quality assurance of volumetric modulated arc therapy," *Med. Phys.*, vol. 36, no. 5, p. 1813, 2009.

[56] V. Feygelman, G. Zhang, C. Stevens, and B. E. Nelms, "Evaluation of a new VMAT QA device, or the "X" and "O" array geometries.," *J. Appl. Clin. Med. Phys.*, vol. 12, no. 2, p. 3346, 2011.

[57] S. Stathakis, P. Myers, C. Esquivel, P. Mavroidis, and N. Papanikolaou, "Characterization of a novel 2D array dosimeter for patient-specific quality assurance with volumetric arc therapy," *Med. Phys.*, vol. 40, no. 7, pp. 1–10, 2013.

[58] M.-H. Lin, S. Koren, I. Veltchev, J. Li, L. Wang, R. a. Price, and C.-M. Ma, "Measurement comparison and Monte Carlo analysis for volumetric-modulated arc therapy (VMAT) delivery verification using the ArcCHECK dosimetry system.," *J. Appl. Clin. Med. Phys.*, vol. 14, no. 2, p. 3929, 2013.

[59] G. Li, Y. Zhang, X. Jiang, S. Bai, G. Peng, K. Wu, and Q. Jiang, "Evaluation of the ArcCHECK QA system for IMRT and VMAT verification.," *Phys. medica*, vol. 29, no. 3, pp. 295–303, 2012.

[60] F. García-Vicente, V. Fernández, R. Bermúdez, A. Gómez, L. Pérez, A. Zapatero, and J. J. Torres, "Sensitivity of a helical diode array device to delivery errors in IMRT treatment and establishment of tolerance level for pretreatment QA," *J. Appl. Clin. Med. Phys.*, vol. 13, no. 1, pp. 111–123, 2012.

[61] J. L. Bedford, Y. K. Lee, P. Wai, C. P. South, and A. P. Warrington, "Evaluation of the Delta4 phantom for IMRT and VMAT verification.," *Phys. Med. Biol.*, vol. 54, no. 9, pp. N167–76, 2009.

[62] R. Sadagopan, J. A. Bencomo, R. L. Martin, G. Nilsson, T. Matzen, and P. A. Balter, "Characterization and clinical evaluation of a novel IMRT quality assurance system," *J. Appl. Clin. Med. Phys.*, vol. 10, no. 2, pp. 104–119, 2009.

[63] S. Korreman, J. Medin, and F. Kjaer-Kristoffersen, "Dosimetric verification of RapidArc treatment delivery.," *Acta Oncol.*, vol. 48, no. 2, pp. 185–91, 2009.

[64] B. E. Nelms, D. Opp, J. Robinson, T. K. Wolf, G. Zhang, E. Moros, and V. Feygelman, "VMAT QA: measurement-guided 4D dose reconstruction on a patient.," *Med. Phys.*, vol. 39, no. 7, pp. 4228–38, 2012.

[65] A. J. Olch, "Evaluation of the accuracy of 3DVH software estimates of dose to virtual ion chamber and film in composite IMRT QA.," *Med. Phys.*, vol. 39, no. 1, pp. 81–6, 2012.

[66] P. Hauri, S. Verlaan, S. Graydon, L. Ahnen, S. Klöck, and S. Lang, "Clinical evaluation of an anatomy-based patient specific quality assurance system," *J. Appl. Clin. Med. Phys.*, vol. 15, no. 2, pp. 181–190, 2014.

[67] W. Ansbacher, "Three-dimensional portal image-based dose reconstruction in a virtual phantom for rapid evaluation of IMRT plans," *Med. Phys.*, vol. 33, no. 9, p. 3369, 2006.

[68] W. Ansbacher, I. M. Gagne, and C.-L. Swift, "A comprehensive EPID-based 3D validation technique for TrueBeam-delivered VMAT plans," *Journal of Physics: Conference Series*, vol. 489, p. 012067, 2014.

[69] K. Jordan and N. Avvakumov, "Radiochromic leuco dye micelle hydrogels: I. Initial investigation," *Phys. Med. Biol.*, vol. 54, no. 22, pp. 6773–6789, 2009.

[70] S. Babic, J. Battista, and K. Jordan, "Radiochromic leuco dye micelle hydrogels: II. Low diffusion rate leuco crystal violet gel," *Phys. Med. Biol.*, vol. 54, no. 22, pp. 6791–6808, 2009.

[71] E. M. Høye, P. S. Skyt, E. S. Yates, L. P. Muren, J. B. B. Petersen, and P. Balling, "A new dosimeter formulation for deformable 3D dose verification," *J. Phys. Conf. Ser.*, vol. 573, p. 012067, 2015.

[72] Y. De Deene, P. S. Skyt, R. Hil, and J. T. Booth, "FlexyDos3D: a deformable anthropomorphic 3D radiation dosimeter: radiation properties.," *Phys. Med. Biol.*, vol. 60, pp. 1543–63, 2015.

[73] J. Adamovics and M. J. Maryanski, "Characterisation of PRESAGE: A new 3-D radiochromic solid polymer dosemeter for ionising radiation.," *Radiation protection dosimetry*, vol. 120, no. 1-4, pp. 107–12, 2006.

[74] J. N. M. Chain, A. Jirasek, L. J. Schreiner, and K. B. McAuley, "Cosolvent-free polymer gel dosimeters with improved dose sensitivity and resolution for x-ray CT dose response.," *Phys. Med. Biol.*, vol. 56, pp. 2091–102, 2011.

[75] M. J. Day and G. Stein, "Chemical Effects of Ionizing Radiation in some Gels," *Nature*, vol. 166, pp. 146–7, 1950.

[76] H. L. Andrews, R. E. Murphy, and E. J. LeBrun, "Gel dosimeter for depth-dose measurements," *Rev. Sci. Instrum.*, vol. 28, no. 5, pp. 329–332, 1957.

[77] P. Alexander, A. Charlesby, and M. Ross, "The degradation of solid polymethylmethacrylate by ionizing radiation," *Proc. R. Soc.*, vol. 223, no. 1154, pp. 392–404, 1954.

[78] F. E. Hoecker and I. W. Watkins, "Radiation Polymerization Dosimetry," *Int. J. Appl. Radiat. Isot.*, vol. 3, no. 1, pp. 31–35, 1958.

[79] A. L. Boni, "A Polyacrylamide Gamma Dosimeter," *Radiat. Res.*, vol. 14, no. 4, pp. 374–380, 1961.

[80] H. Fricke and S. Morse, "The chemical action of Roentgen rays on dilute ferrous sulphate solutions as a measure of radiation dose," *Am. J. Roentgenol., Radium Ther. Nuc. Med.,*, vol. 18, pp. 430–432, 1927.

[81] J. C. Gore, Y. S. Kang, and R. J. Schulz, "Measurement of radiation dose distributions by nuclear magnetic resonance (NMR) imaging," *Phys. Med. Biol.*, vol. 29, no. 10, pp. 1189–1197, 1984.

[82] L. E. Olsson, B. A. Westrin, A. Fransson, and B. Nordell, "Diffusion of ferric ions in agarose dosimeter gels," *Phys. Med. Biol.*, vol. 37, no. 12, pp. 2243–2252, 1992.

[83] M. J. Maryanski, J. C. Gore, and R. J. Schulz, "3-D radiation dosimetry by MRI: solvent proton relaxation enhancement by radiation-controlled polymerisation and cross-linking in gels," *Proc. Int. Soc. for Magnetic Resonance in Medicine (New York)*, 1992.

[84] Y. DeDeene, C. D. Wagter, and B. V. Duyse, "Three-dimensional dosimetry using polymer gel and magnetic resonance imaging applied to the verification of conformal radiation therapy in head-and-neck cancer," *Radiother. Oncol.*, vol. 48, pp. 283–291, 1998.

[85] C. Baldock, R. P. Burford, N. Billingham, G. S. Wagner, S. Patval, R. D. Badawi, and S. F. Keevil, "Experimental procedure for the manufacture and calibration of polyacrylamide gel (PAG) for magnetic resonance imaging (MRI) radiation dosimetry," *Phys. Med. Biol.*, vol. 43, pp. 695–702, 1998.

[86] M. J. Maryanski, R. J. Schulz, G. S. Ibbott, J. C. Gatenby, J. Xie, D. Horton, and J. C. Gore, "Magnetic resonance imaging of radiation dose distributions using a polymer-gel dosimeter," *Phys. Med. Biol.*, vol. 39, pp. 1437–1455, 1994.

[87] J. C. Gore, M. Ranade, M. J. Maryanski, and S. R, "Radiation dose distributions in three dimensions from tomographic optical density scanning of polymer

gels: I. Development of an optical scanner," *Phys. Med. Biol.*, vol. 41, pp. 2695–2704, 1996.

[88] M. J. Maryanski, Y. Z. Zastavker, and J. C. Gore, "Radiation dose distributions in three dimensions from tomographic optical density scanning of polymer gels: II. Optical properties of the BANG polymer gel," *Phys. Med. Biol.*, vol. 41, pp. 2705–2717, 1996.

[89] M. Hilts, C. Audet, C. Duzenli, and A. Jirasek, "Polymer gel dosimetry using x-ray computed tomography: a feasibility study," *Phys. Med. Biol.*, vol. 45, pp. 2559–2571, 2000.

[90] L. Rintoul, M. Lepage, and C. Baldock, "Radiation Dose Distribution in Polymer Gels by Raman Spectroscopy," *Appl. Spectrosc.*, vol. 57, no. 1, pp. 51–57, 2003.

[91] M. L. Mather, A. K. Whittaker, and C. Baldock, "Physics in Medicine & Biology Ultrasound evaluation of polymer gel dosimeters Ultrasound evaluation of polymer gel dosimeters," *Phys. Med. Biol.*, vol. 47, pp. 1449–1458, 2002.

[92] P. M. Fong, D. C. Keil, M. D. Does, and J. C. Gore, "Polymer gels for magnetic resonance imaging of radiation dose distributions at normal room atmosphere," *Phys. Med. Biol.*, vol. 46, pp. 3105–3113, 2001.

[93] Y. De Deene, C. Hurley, A. Venning, K. Vergote, M. Mather, B. J. Healy, and C. Baldock, "A basic study of some normoxic polymer gel dosimeters," *Phys. Med. Biol.*, vol. 47, pp. 3441–3463, 2002.

[94] A. Jirasek, M. Hilts, C. Shaw, and P. Baxter, "Investigation of tetrakis hydroxymethyl phosphonium chloride as an antioxidant for use in x-ray computed tomography polyacrylamide gel dosimetry.," *Phys. Med. Biol.*, vol. 51, pp. 1891–1906, 2006.

[95] K. Jordan, "Review of recent advances in radiochromic materials for 3D dosimetry," *J. Phys. Conf. Ser.*, vol. 250, pp. 193–199, 2010.

[96] R. J. Senden, P. De Jean, K. B. McAuley, and L. J. Schreiner, "Polymer gel dosimeters with reduced toxicity: a preliminary investigation of the NMR and optical dose-response using different monomers.," *Phys. Med. Biol.*, vol. 51, no. 14, pp. 3301–3314, 2006.

[97] S. M. Ghavami, A. Mesbahi, I. Pesianian, A. Shafaee, and M. R. Aliparasti, "Normoxic polymer gel dosimetry using less toxic monomer of N-isopropyl acrylamide and X-ray computed tomography for radiation therapy applications," *Reports Pract. Oncol. Radiother.*, vol. 15, no. 6, pp. 172–175, 2010.

[98] R. G. Kelly, K. J. Jordan, and J. J. Battista, "Optical CT reconstruction of 3D dose distributions using the ferrous-benzoic-xylenol (FBX) gel dosimeter," *Med. Phys.*, vol. 25, no. 9, pp. 1741–1750, 1998.

[99] E. M. Høye, P. Balling, E. S. Yates, L. P. Muren, J. B. B. Petersen, and P. S. Skyt, "Eliminating the dose-rate effect in a radiochromic silicone-based 3D dosimeter," *Phys. Med. Biol.*, vol. 60, pp. 5557–5570, 2015.

[100] L. Kaplan, E. M. Høye, P. Balling, L. P. Muren, J. B. B. Petersen, P. R. Poulsen, E. S. Yates, and P. S. Skyt, "Determining the mechanical properties of a radiochromic silicone-based 3D dosimeter," *Phys. Med. Biol.*, vol. 62, pp. 5612–5622, 2017.

[101] C. Baldock, L. Rintoul, S. F. Keevil, J. M. Pope, and G. A. George, "Fourier transform Raman spectroscopy of polyacrylamide gels (PAGs) for radiation dosimetry," *Phys. Med. Biol.*, vol. 43, pp. 3617–3627, 1998.

[102] A. I. Jirasek, C. Duzenli, C. Audet, and J. Eldridge, "Characterization of monomer/crosslinker consumption and polymer formation observed in ft-raman spectra of irradiated polyacrylamide gels," *Phys. Med. Biol.*, vol. 46, pp. 151–165, 2001.

[103] A. I. Jirasek and C. Duzenli, "Effects of crosslinker fraction in polymer gel dosimeters using FT Raman spectroscopy," *Phys. Med. Biol.*, vol. 46, no. 7, pp. 1949–1961, 2001.

[104] M. J. Maryanski, C. Audet, and J. C. Gore, "Effects of crosslinking and temperature on the dose response of a BANG polymer gel dosimeter," *Phys. Med. Biol.*, vol. 42, no. 2, pp. 303–311, 1997.

[105] J. T. Bushberg, J. A. Seibert, E. M. L. Jr., and J. M. Boone, *The Essential Physics of Medical Imaging*. Lippincott Williams and Wilkins, 2002.

[106] M. J. Maryanski, J. C. Gore, R. P. Kennan, and R. J. Schulz, "NMR relaxation enhancement in gels polymerized and cross-linked by ionizing radiation: A new approach to 3D dosimetry by MRI," *Magn. Reson. Imaging*, vol. 11, no. 2, pp. 253–258, 1993.

[107] J. Vandecasteele and Y. De Deene, "On the validity of 3D polymer gel dosimetry: III. MRI-related error sources," *Phys. Med. Biol.*, vol. 58, no. 1, pp. 63–85, 2013.

[108] Y. DeDeene, "Review of quantitative MRI principles for gel dosimetry," *J. Phys. Conf. Ser.*, vol. 164, 2009.

[109] Y. De Deene and C. De Wagter, "Artefacts in multi-echo T2 imaging for high-precision gel dosimetry: III. Effects of temperature drift during scanning," *Phys. Med. Biol.*, vol. 46, pp. 2697–2711, 2001.

[110] S. J. Doran, "The history and principles of optical computed tomography for scanning 3-D radiation dosimeters: 2008 update," *J. Phys. Conf. Ser.*, vol. 164, no. 1, p. 012020, 2009.

[111] W. G. Campbell, D. M. Wells, and A. Jirasek, "Radiation-induced refraction artifacts in the optical CT readout of polymer gel dosimeters," *Med. Phys.*, vol. 41, no. 11, 2014.

[112] R. Cierniak, *X-Ray Computed Tomography in Biomedical Engineering*. Springer, 2011.

[113] T. M. Buzug, *Computed Tomography*. Springer, 2008.

[114] G. Dougherty, *Digital Image Processing for Medical Applications*. Cambridge University Press, 2009.

[115] M. Hilts, a. Jirasek, and C. Duzenli, "Effects of gel composition on the radiation induced density change in PAG polymer gel dosimeters: a model and experimental investigations," *Physics in Medicine and Biology*, vol. 49, no. 12, pp. 2477–2490, 2004.

[116] M. Hilts and A. Jirasek, "Adaptive mean filtering for noise reduction in CT polymer gel dosimetry," *Med. Phys.*, vol. 35, no. 1, p. 344, 2008.

[117] A. Jirasek, J. Carrick, and M. Hilts, "An x-ray CT polymer gel dosimetry prototype: I. Remnant artefact removal.," *Phys. Med. Biol.*, vol. 57, pp. 3137–53, 2012.

[118] A. Jirasek, M. Hilts, and K. B. McAuley, "Polymer gel dosimeters with enhanced sensitivity for use in x-ray CT polymer gel dosimetry.," *Phys. Med. Biol.*, vol. 55, pp. 5269–81, 2010.

[119] H. Johnston, M. Hilts, J. Carrick, and A. Jirasek, "An x-ray CT polymer gel dosimetry prototype: II. Gel characterization and clinical application.," *Phys. Med. Biol.*, vol. 57, pp. 3155–75, 2012.

[120] M. Sedaghat, R. Bujold, and M. Lepage, "Investigating potential physicochemical errors in polymer gel dosimeters," *Phys. Med. Biol.*, vol. 56, pp. 6083–6107, 2011.

[121] H. Johnston, M. Hilts, and A. Jirasek, "Incorporating multislice imaging into x-ray CT polymer gel dosimetry," *Med. Phys.*, vol. 42, no. 4, pp. 1666–77, 2015.

[122] A. Jirasek and M. Hilts, "Dose calibration optimization and error propagation in polymer gel dosimetry," *Phys. Med. Biol.*, vol. 59, 2014.

[123] M. Hilts, A. Jirasek, and C. Duzenli, "Technical considerations for implementation of x-ray CT polymer gel dosimetry.," *Phys. Med. Biol.*, vol. 50, pp. 1727–45, 2005.

[124] P. Baxter, A. Jirasek, and M. Hilts, "X-ray CT dose in normoxic polyacrylamide gel dosimetry," *Med. Phys.*, vol. 34, no. 6, p. 1934, 2007.

[125] P. Andreo, "Monte Carlo techniques in medical radiation physics," *Phys. Med. Biol.*, vol. 36, no. 7, pp. 861–920, 1991.

[126] I. Kawrakow, D. W. Rogers, and B. R. Walters, "Large efficiency improvements in BEAMnrc using directional bremsstrahlung splitting," *Med. Phys.*, vol. 31, no. 10, pp. 2883–2898, 2004.

[127] D. W. O. Rogers, B. R. Walters, and I. Kawrakow, "BEAMnrc Users Manual," *NRC Report*, 2006.

[128] B. R. Walters, I. Kawrakow, and D. W. O. Rogers, "DOSXYZnrc Users Manual," *NRC Report*, 2006.

[129] I. Kawrakow and M. Fippel, "VMC++, a fast MC algorithm for Radiation Treatment planning," *The Use of Computers in Radiation Therapy*, pp. 126–128, 2000.

[130] N. Kadoya, Y. Fujita, Y. Katsuta, S. Dobashi, K. Takeda, K. Kishi, M. Kubozono, R. Umezawa, T. Sugawara, H. Matsushita, and K. Jingu, "Evaluation of various deformable image registration algorithms for thoracic images," *J. Radiat. Res.*, vol. 55, no. 1, pp. 175–182, 2014.

[131] K. K. Brock, M. B. Sharpe, L. A. Dawson, S. M. Kim, and D. A. Jaffray, "Accuracy of finite element model-based multi-organ deformable image registration," *Med. Phys.*, vol. 32, no. 6, pp. 1647–1659, 2005.

[132] S. Oh and S. Kim, "Deformable image registration in radiation therapy," *Radiat. Oncol. J.*, vol. 35, no. 2, pp. 101–111, 2017.

[133] K. K. Brock, S. Mutic, T. R. Mcnutt, H. Li, and M. L. Kessler, "Use of image registration and fusion algorithms and techniques in radiotherapy: Report of the AAPM Radiation Therapy Committee Task Group No. 132," *Med. Phys.*, vol. 44, no. 7, pp. e43–e76, 2017.

[134] H. Paganetti, H. Jiang, J. A. Adams, G. T. Chen, and E. Rietzel, "Monte Carlo simulations with time-dependent geometries to investigate effects of organ motion with high temporal resolution," *Int. J. Radiat. Oncol. Biol. Phys.*, vol. 60, no. 3, pp. 942–950, 2004.

[135] B. Schaly, J. A. Kempe, G. S. Bauman, J. J. Battista, and J. Van Dyk, "Tracking the dose distribution in radiation therapy by accounting for variable anatomy," *Phys. Med. Biol.*, vol. 49, no. 5, pp. 791–805, 2004.

[136] P. J. Keall, J. V. Siebers, S. Joshi, and R. Mohan, "Monte Carlo as a four-dimensional radiotherapy treatment-planning tool to account for respiratory motion," *Phys. Med. Biol.*, vol. 49, no. 16, pp. 3639–3648, 2004.

[137] J. V. Siebers and H. Zhong, "An energy transfer method for 4D Monte Carlo dose calculation," *Med. Phys.*, vol. 35, no. 9, pp. 4096–4105, 2008.

[138] A. R. Farajollahi, D. E. Bonnett, A. J. Ratcliffe, R. J. Aukett, and J. A. Mills, "An investigation into the use of polymer gel dosimetry in low dose rate brachytherapy.," *The British Journal of Radiology*, vol. 72, no. 863, pp. 1085–1092, 1999.

[139] A. E. Rodrigues, S. W. Yoon, M. Oldham, J. Adamovics, S. Meltsner, and O. Craciunescu, "High Resolution 3D Dosimetry for LDR Ocular Brachytherapy," *Brachytherapy*, vol. 16, no. 3, 2017.

[140] C. Matrosic, W. Culberson, B. Rosen, E. Madsen, G. Frank, and B. Bednarz, "Initial characterization of a gel patch dosimeter for in vivo dosimetry," *Phys. Med. Biol.*, vol. 61, no. 10, pp. N240–N248, 2016.

[141] A. Jirasek and C. Duzenli, "Relative effectiveness of polyacrylamide gel dosimeters applied to proton beams: Fourier transform Raman observations and track structure calculations," *Med. Phys.*, vol. 29, no. 4, pp. 569–577, 2002.

[142] J. Heufelder, S. Stiefel, M. Pfaender, L. Lüdemann, G. Grebe, and J. Heese, "Use of BANG® polymer gel for dose measurements in a 68 MeV proton beam," *Med. Phys.*, vol. 30, no. 6, pp. 1235–1240, 2003.

[143] H. Gustavsson, S. Å. J. Bäck, J. Medin, E. Grusell, and L. E. Olsson, "Linear energy transfer dependence of a normoxic polymer gel dosimeter investigated using proton beam absorbed dose measurements," *Phys. Med. Biol.*, vol. 49, no. 17, pp. 3847–3855, 2004.

[144] B. Hill, A. J. Venning, and C. Baldock, "A preliminary study of the novel application of normoxic polymer gel dosimeters for the measurement of CTDI on diagnostic x-ray CT scanners," *Med. Phys.*, vol. 32, no. 6, pp. 1589–1597, 2005.

[145] B. Hill, A. J. Venning, and C. Baldock, "Polymer gel dosimetry on a multislice computed tomography scanner: Effect of changing parameters on CTDI," *Phys. Medica*, vol. 24, no. 3, pp. 149–158, 2008.

[146] L. J. Rankine, S. Mein, B. Cai, A. Curcuru, T. Juang, D. Miles, S. Mutic, Y. Wang, M. Oldham, and H. H. Li, "Three-Dimensional Dosimetric Validation of a Magnetic Resonance Guided Intensity Modulated Radiation Therapy System," *Int. J. Radiat. Oncol. Biol. Phys.*, vol. 97, no. 5, pp. 1095–1104, 2017.

[147] F. Costa, S. Doran, I. Hanson, S. Nill, I. Billas, D. Shipley, S. Duane, J. Adamovics, and U. Oelfke, "Investigating the effect of a magnetic field on dose distributions at phantom-air interfaces using PRESAGE® 3D dosimeter and Monte Carlo simulations," *Phys. Med. Biol.*, vol. 63, no. 5, 2018.

[148] H. J. Lee, G. Won Choi, M. Alqathami, M. Kadbi, and G. Ibbott, "Using 3D dosimetry to quantify the Electron Return Effect (ERE) for MR-image-guided radiation therapy (MR-IGRT) applications," *J. Phys. Conf. Ser.*, vol. 847, no. 1, 2017.

[149] S. Mein, L. Rankine, J. Adamovics, H. Li, and M. Oldham, "Development of a 3D remote dosimetry protocol compatible with MRgIMRT:," *Med. Phys.*, vol. 44, no. 11, pp. 6018–6028, 2017.

[150] T. Kairn, A. Asena, S. B. Crowe, A. Livingstone, D. Papworth, S. Smith, B. Sutherland, S. Sylvander, R. D. Franich, and J. V. Trapp, "Can a commercial gel dosimetry system be used to verify stereotactic spinal radiotherapy treatment dose distributions?," *J. Phys. Conf. Ser.*, vol. 847, 2017.

[151] C. M. McErlean, E. Bräuer-Krisch, J. Adamovics, and S. J. Doran, "Assessment of optical CT as a future QA tool for synchrotron x-ray microbeam therapy," *Phys. Med. Biol.*, vol. 61, no. 1, pp. 320–337, 2015.

[152] C. McErlean, E. Bräuer-Krisch, J. Adamovics, M. O. Leach, and S. J. Doran, "High resolution 3D dosimetry for microbeam radiation therapy using optical CT," *J. Phys. Conf. Ser.*, vol. 573, no. 1, 2015.

[153] F. M. Gagliardi, L. Day, C. M. Poole, R. D. Franich, and M. Geso, "Water equivalent PRESAGE® for synchrotron radiation therapy dosimetry," *Med. Phys.*, 2018.

[154] C. Audet, M. Hilts, A. Jirasek, and C. Duzenli, "CT gel dosimetry technique: comparison of a planned and measured 3D stereotactic dose volume.," *J. Appl. Clin. Med. Phys.*, vol. 3, no. 2, pp. 110–118, 2002.

[155] C. Y. Chiu, Y. W. Tsang, and B. T. Hsieh, "N-isopropylacrylamide gel dosimeter to evaluate clinical photon beam characteristics," *Appl. Radiat. Isot.*, vol. 90, pp. 245–250, 2014.

[156] C. J. Niu, W. D. Foltz, M. Velec, J. L. Moseley, A. Al-Mayah, and K. K. Brock, "A novel technique to enable experimental validation of deformable dose accumulation.," *Med. Phys.*, vol. 39, no. 2, pp. 765–76, 2012.

[157] U. J. Yeo, M. L. Taylor, L. Dunn, T. Kron, R. L. Smith, and R. D. Franich, "A novel methodology for 3D deformable dosimetry," *Med. Phys.*, vol. 39, no. 4, pp. 2203 – 2213, 2012.

[158] T. Juang, S. Das, J. Adamovics, R. Benning, and M. Oldham, "On the need for comprehensive validation of deformable image registration, investigated with a novel 3-dimensional deformable dosimeter," *Int. J. Radiat. Oncol. Biol. Phys.*, vol. 87, no. 2, pp. 414–421, 2013.

[159] R. D. Franich, J. R. Supple, B. Lindsay, U. J. Yeo, P. Lonski, R. L. Smith, M. L. Taylor, L. Dunn, and T. Kron, "Reproducibility assessment of dynamically deforming DEFGEL in a respiratory motion phantom," *J. Phys. Conf. Ser.*, vol. 573, p. 012024, 2015.

[160] U. J. Yeo, M. L. Taylor, J. R. Supple, R. L. Smith, L. Dunn, T. Kron, and R. D. Franich, "Is it sensible to deform dose? 3D experimental validation of dose-warping," *Med. Phys.*, vol. 39, no. 8, p. 5065, 2012.

[161] U. J. Yeo, J. R. Supple, M. L. Taylor, R. Smith, T. Kron, and R. D. Franich, "Performance of 12 DIR algorithms in low-contrast regions for mass and density conserving deformation.," *Med. Phys.*, vol. 40, no. 10, p. 101701, 2013.

[162] H. K. Sinclair, "Gas barrier coating and coated elastomeric toy balloons," 1993. US Patent 5,244,429.

[163] S. Zeman and L. Kubik, "Permeability of polymeric packing materials," *Techn. Sc.*, vol. 10, pp. 26–34, 2007.

[164] M. Hilts, J. Carrick, H. Johnston, and A. Jirasek, "SU-E-T-93: A CT Polymer Gel Dosimetry System for End-To-End Dosimetry," *Med. Phys.*, vol. 38, no. 6, p. 3507, 2011.

[165] K. Bush, R. Townson, and S. Zavgorodni, "Monte Carlo simulation of RapidArc radiotherapy delivery.," *Phys. Med. Biol.*, vol. 53, pp. N359–70, 2008.

[166] P. G. Righetti, B. C. W. Brost, and R. S. Snyder, "Polymerization kinetics of polyacrylamide gels: I. Effects of different crosslinkers.," *J. Biochem. Biophys. Methods*, vol. 4, no. 5-6, pp. 347–63, 1981.

[167] C. Gelfi and P. Righetti, "Polymerization kinetics of polyacrylamide gels: I. Effects of different crosslinkers.," *Electrophoresis*, vol. 2, no. 4, pp. 213–9, 1981.

[168] D. A. Low, W. B. Harms, S. Mutic, and J. A. Purdy, "A technique for the quantitative evaluation of dose distributions.," *Med. Phys.*, vol. 25, no. 5, pp. 656–61, 1998.

[169] P. S. Basran and M. K. Woo, "An analysis of tolerance levels in IMRT quality assurance procedures," *Med. Phys.*, vol. 35, no. 6, pp. 2300–2307, 2008.

[170] M. Miften, A. Olch, D. Mihailidis, J. Moran, T. Pawlicki, A. Molineu, H. Li, K. Wijesooriya, J. Shi, P. Xia, N. Papanikolaou, and D. A. Low, "Tolerance limits and methodologies for IMRT measurement-based verification QA: Recommendations of AAPM Task Group No. 218," *Med. Phys.*, vol. 45, no. 4, pp. e53–e83, 2018.

[171] J. Vandecasteele and Y. De Deene, "On the validity of 3D polymer gel dosimetry: I. reproducibility study.," *Phys. Med. Biol.*, vol. 58, no. 1, pp. 19–42, 2013.

[172] J. Vandecasteele and Y. De Deene, "On the validity of 3D polymer gel dosimetry: II. physico-chemical effects.," *Phys. Med. Biol.*, vol. 58, pp. 43–61, 2013.

[173] L. Rankine and M. Oldham, "On the feasibility of optical-CT imaging in media of different refractive index," *Med. Phys.*, vol. 40, no. 5, p. 051701(8pp), 2013.

[174] Y. J. Chang, J. Q. Lin, B. T. Hsieh, C. H. Yao, and C. H. Chen, "Dose evaluation of an NIPAM polymer gel dosimeter using gamma index," *Radiat. Phys. Chem.*, vol. 104, pp. 180–187, 2014.

[175] M. B. Kakakhel, T. Kairn, J. Kenny, and J. V. Trapp, "Improved image quality for x-ray CT imaging of gel dosimeters," *Med. Phys.*, vol. 38, no. 9, pp. 5130–5135, 2011.

[176] T. Gorjiara, R. Hill, S. Bosi, Z. Kuncic, and C. Baldock, "Water equivalence of NIPAM based polymer gel dosimeters with enhanced sensitivity for x-ray CT," *Radiat. Phys. Chem.*, vol. 91, pp. 60–69, 2013.

[177] V. I. Koeva, T. Olding, A. Jirasek, L. J. Schreiner, and K. B. McAuley, "Preliminary investigation of the NMR, optical and x-ray CT dose-response of polymer gel dosimeters with cosolvents and increased crosslinker levels," *Phys. Med. Biol.*, vol. 54, pp. 2779–2790, 2009.

[178] B. T. Hsieh, Y. J. Chang, R. P. Han, J. Wu, L. L. Hsieh, and C. J. Chang, "A study on dose response of NIPAM-based dosimeter used in radiotherapy," *J. Radioanal. Nucl. Chem.*, vol. 290, pp. 141–148, 2011.

[179] Y. D. Deene, "On the accuracy and precision of gel dosimetry," *J. Phys. Conf. Ser.*, vol. 56, pp. 72–85, 2006.

[180] M. Oldham, J. H. Siewerdsen, S. Kumar, J. Wong, and D. A. Jaffray, "Optical-CT gel-dosimetry I: basic investigations.," *Med. Phys.*, vol. 30, no. 4, pp. 623–34, 2003.

[181] M. Oldham and L. Kim, "Optical-CT gel-dosimetry. II: Optical artifacts and geometrical distortion.," *Med. Phys.*, vol. 31, no. 5, pp. 1093–104, 2004.

[182] M. Oldham, H. Sakhalkar, P. Guo, and J. Adamovics, "An investigation of the accuracy of an IMRT dose distribution using two- and three-dimensional dosimetry techniques.," *Med. Phys.*, vol. 35, no. 5, pp. 2072–80, 2008.

[183] J. Jackson, T. Juang, J. Adamovics, and M. Oldham, "An investigation of PRESAGE 3D dosimetry for IMRT and VMAT radiation therapy treatment verification," *Phys. Med. Biol.*, vol. 60, no. 6, pp. 2217–2230, 2015.

[184] E. Maynard, E. Heath, M. Hilts, and A. Jirasek, "Introduction of a deformable x-ray CT polymer gel dosimetry system.," *Phys. Med. Biol.*, vol. 63, p. 075014 (14pp), 2018.

[185] G. Starkschall, K. Britton, M. F. McAleer, M. D. Jeter, M. R. Kaus, K. Bzdusek, R. Mohan, and J. D. Cox, "Potential Dosimetric Benefits of Four-Dimensional Radiation Treatment Planning," *Int. J. Radiat. Oncol. Biol. Phys.*, vol. 73, no. 5, pp. 1560–1565, 2009.

[186] H. Zhong and J. V. Siebers, "Monte Carlo dose mapping on deforming anatomy.," *Phys. Med. Biol.*, vol. 54, pp. 5815–5830, 2009.

[187] G. Janssens, J. O. de Xivry, S. Fekkes, A. Dekker, B. Macq, P. Lambin, and W. van Elmpt, "Evaluation of nonrigid registration models for interfraction dose accumulation in radiotherapy.," *Med. Phys.*, vol. 36, no. 9, pp. 4268–76, 2009.

[188] E. Heath, F. Tessier, and I. Kawrakow, "Investigation of voxel warping and energy mapping approaches for fast 4D Monte Carlo dose calculations in deformed geometries using VMC++.," *Phys. Med. Biol.*, vol. 56, pp. 5187–202, 2011.